

DISSERTATION

High Power Proton Beam Shocks  
and  
Magnetohydrodynamics  
in a  
Mercury Jet Target  
for a Neutrino Factory

ausgeführt zum Zwecke der Erlangung des akademischen Grades eines  
Doktors der technischen Wissenschaften unter der Leitung von

Ao. Univ. Prof. Dr. Christian W. Fabjan  
E141

Atominstitut der österreichischen Universitäten

im Rahmen des

Austrian Doctoral Student Program

am CERN, CH-1211 Geneve 23

eingereicht an der Technischen Universität Wien

Fakultät für Technische Naturwissenschaften und Informatik

von

Dipl.Ing. Adrian Fabich

9226849

A-1060 Wien, Bürgerspitalgasse 9

Wien, im November 2002

CERN-THESIS-2002-038  
22/11/2002





## Kurzfassung

Das Verhalten von Flüssigmetall-Targets für Sekundärpartikelproduktion wurde untersucht. Die Hauptaspekte dieser Arbeit sind der thermische Schock, der in einem flüssigen Target durch einen intensiven Protonenpuls hervorgerufen wird, und die Magnetohydrodynamik eines Quecksilberstrahles.

In der ISOLDE Anlage am CERN und am Hochfeld-Magnetlabor (High Magnetic Field Laboratory) in Grenoble ergaben sich aus Sicherheitsgründen und zeitlich eingeschränkten Versuchsdurchführungen mehrere Herausforderungen. Die Zugangsdauer zu den Bereichen hoher Radioaktivität waren auf Minuten begrenzt, und in dieser Zeit mußte die Versuchsanordnung installiert werden. Die Verwendung von Quecksilber und dessen Aktivierung verlangte zusätzliche Sicherheitsvorkehrungen.

Die Beobachtung wurde in beiden experimentellen Reihen mittels einer Hochgeschwindigkeitkamera durchgeführt. Die radioaktive Strahlung und das starke Magnetfeld erforderten die Installation der Kamera in einem Abstand von bis zu 15 m. Aufgrund der reflektierenden Oberfläche des Quecksilbers wurde die Methode der Schattenfotographie angewendet.

In der ISOLDE Anlage am CERN und am Brookhaven AGS wurde das Verhalten von einem flüssigen, metallischen Target unter Einwirkung eines intensiven Protonenstrahles in Abhängigkeit einzelner Strahlparameter gemessen. Die Ergebnisse erlauben eine Extrapolation dieses Verhaltens zu dem nominellen Design einer Neutrino-fabrik ("neutrino factory"). Die höchsten beobachteten Geschwindigkeiten der Quecksilberexplosion waren 45 m/s.

Der Versuchsaufbau am High Magnetic Field Laboratory in Grenoble erlaubte die erfolgreiche Demonstration der Injektion eines 12 m/s Quecksilberstrahles mit einem Durchmesser  $d = 4$  mm in ein 20 T Solenoidfeld. Die Experimente zeigten die magnetohydrodynamischen Effekte, die im freien Strahl und im versorgenden Quecksilberkreislauf auftreten, und die Ergebnisse dienen zur Verifikation numerischer Simulationen.

Die Extrapolation zu den nominellen Parametern einer Neutrino-fabrik zeigt, daß das Konzept eines Quecksilberstrahles als Target eine mögliche Option ist.

## Abstract

The feasibility of liquid metal jet targets for secondary particle production with high power proton beams has been studied. The main aspects of the thesis were benchmark experiments covering the behaviour of liquid targets under thermal shock waves induced by high power proton beams, and also magnetohydrodynamic effects.

Severe challenges were imposed by safety issues and the restricted beam time dedicated to the tests in ISOLDE at CERN and at the High Magnetic Field Laboratory at Grenoble. Restricted access times in high radiation level areas were of the order of minutes and in this short time span, the complete experimental setup had to be performed and verified. The involvement of mercury as liquid target material and its activation during beam tests demanded special confinement precautions.

The setup for both experiments was based on the use of a high speed camera system for observation of the mercury target. The presence of high radiation or high magnetic field required the installation of the sensitive camera system at distances up to 15 m. The method of shadow photography had to be used because of the highly reflective surface of mercury.

During proton beam tests at the CERN ISOLDE facility and at Brookhaven AGS, the behaviour of a mercury target as a function of various proton beam parameters was analysed. The experimental results allow for extrapolation from the present data by one order of magnitude to the final design of a high power jet target foreseen for a neutrino factory. Observed velocities of the mercury splash were up to 45 m/s.

The experimental setup used at the High Magnetic Field Laboratory allowed a successful demonstration of injecting a 12 m/s mercury jet with a diameter  $d = 4$  mm into a 20 T solenoidal field. The results of this experiment revealed the magnetohydrodynamic effects, which occur in the free jet and in the supplying mercury circuit, and serve as benchmark for numerical codes.

The extrapolation to the nominal parameters of a neutrino factory shows that the concept of a jet target is a valid option.

## Acknowledgement

I am most grateful to Christian Fabjan for his guidance and support during my studies. Jacques Lettry as my local supervisor did a great job and it was a pleasure to work with them.

Helmut Haseroth and his never-ending enthusiasm supported me a lot during the last few years.

I thank all my colleagues from the PS division, especially those from the ISOLDE target group.

I want to express my sincere thanks to the people of the US Neutrino Factory and Muon Collider Collaboration, especially to Harold, Kirk and Mike, and to the High Magnetic Field Laboratory at Grenoble for their continuous cooperation.

I won't forget the initial work done by Daniel. Michael and Christian gave me advice in accelerator physics when needed, and so did Andreas in informatics. I thank Erk for his help, when I started my PhD work.

# Contents

<b>1</b>	<b>Introduction</b>	<b>1</b>
1.1	High Power Proton Beam Scenarios . . . . .	1
1.2	A Neutrino Factory . . . . .	2
1.2.1	Neutrino Physics . . . . .	3
1.3	Other High Power Target Facilities . . . . .	8
<b>2</b>	<b>The Target Station</b>	<b>10</b>
2.1	A High Power Proton Beam . . . . .	10
2.2	The Target Station . . . . .	12
2.2.1	Pion Collection . . . . .	12
2.3	Options for a High Power Proton Beam Target . . . . .	15
2.4	Feasibility Study of a Liquid Metal Jet Target . . . . .	18
<b>3</b>	<b>Proton Induced Shocks</b>	<b>19</b>
3.1	Solid Targets . . . . .	20
3.2	Liquid Targets . . . . .	24
3.3	Experimental Layout . . . . .	24
3.3.1	AGS and PSB Test Areas . . . . .	25
3.3.2	Mercury Test Targets . . . . .	27
3.3.3	Simulation of the Energy Deposition . . . . .	30
3.3.4	Diagnostics . . . . .	31
3.3.5	Digital Image Processing . . . . .	33
3.4	The Behaviour of Thimble, Trough and Jet on Impact of a Proton Pulse . . . . .	37
3.4.1	The Thimble Splash . . . . .	37
3.4.2	The Trough Splash . . . . .	38
3.4.3	The Jet Splash . . . . .	39
3.4.4	Pulse Intensity . . . . .	42
3.4.5	The Spot Size . . . . .	43
3.4.6	Pulse Length . . . . .	44
3.4.7	Cavitation . . . . .	45
3.4.8	Beam Scan of the Target . . . . .	45
3.5	Conclusion . . . . .	46

<b>4</b>	<b>A Metal Jet in a High Magnetic Field</b>	<b>48</b>
4.1	Experimental Layout . . . . .	49
4.1.1	The 20 Tesla Solenoid M9 . . . . .	49
4.1.2	The Jet Setup . . . . .	49
4.1.3	Diagnostics and Digital Image Processing . . . . .	53
4.2	Observations . . . . .	55
4.2.1	Jet Velocity at $B=0$ T . . . . .	55
4.2.2	Dynamic Pressure . . . . .	56
4.2.3	The Sprayed Jet . . . . .	57
4.2.4	The Stable Jet . . . . .	57
4.2.5	The Jet Tip . . . . .	57
4.2.6	Deflection . . . . .	60
4.2.7	Jet Diameter . . . . .	60
4.2.8	Velocity . . . . .	61
4.3	Magnetohydrodynamics . . . . .	62
4.4	Conclusions . . . . .	63
<b>5</b>	<b>Conclusion</b>	<b>65</b>
<b>A</b>	<b>Material Properties</b>	<b>66</b>
<b>B</b>	<b>The mercury jet setup for the MHD experiment</b>	<b>68</b>
<b>C</b>	<b>Cavitation Bubbles</b>	<b>73</b>
	<b>Bibliography</b>	<b>75</b>
	<b>Curriculum Vitae</b>	<b>79</b>





# Chapter 1

## Introduction

### 1.1 High Power Proton Beam Scenarios

In the recent past at CERN, the **S**uper **P**roton **S**ynchrotron (SPS) contributed to the discovery of the electro-weak bosons and the **L**arge **E**lectron **P**ositron Collider (LEP) to the precision measurements of the standard model. The next generation of high-energy physics research facilities has to operate in the  $TeV$  range in order to address important issues of elementary particle physics. The **L**arge **H**adron **C**ollider (LHC), presently under construction, will cover center-of-mass energies of several  $TeV$  of proton collisions for the research in the extension of the standard model, the super-symmetry and the higgs boson. A next generation collider under study is CLIC, the **C**ompact **L**inear **C**ollider, which will contribute also to the physics beyond the standard model, where the lightest leptons are collided at energies of several  $TeV$ . All these accelerators and colliders are to accelerate primary particle beams, either light leptons or ions. The required statistics in the collision processes demand a very high flux of primary particles. As an example, LHC will operate at a collision rate of  $10^9 \text{ s}^{-1}$ .

On interaction of the primary particles with a target, it is possible to produce secondary beams of elementary particles like pions, kaons, neutrons and gammas. Primary protons pass through a linear accelerator and further through synchrotron, bunch compressors and accumulator to achieve a beam with a certain energy, intensity and beam structure. This beam is directed towards a fixed target. On interaction with this target secondary particles of different kinds are produced. E.g. the secondary neutron flux is produced by spallation of a neutron rich target nuclei and used in neutron spallation sources for solid state physics [1]. As the secondary particle yield is often low, but still high secondary particle flux is desired, primary particles beams of highest intensities are developed.

Assuming a particle accelerator, where the primary particle beam is converted into a secondary particle beam, which itself also turns into another family of particles, it is obvious that the production of high intensities of such third generation particles is even more demanding.

High power proton beam concepts are demanded in order to produce particular particles, not producible in different ways, like high intensity neutrino beams as in the concept of a neutrino

superbeam or a neutrino factory. As the presented work was performed within the Neutrino Factory Working Group (NFWG) at CERN, an introduction to this future facility and its purposes are presented. It serves as a reference for the assumed target scenario, which this study has been made for. A neutrino factory is the ultimate tool to produce a high intensity neutrino beam to study neutrino oscillations and CP violation.

The high power primary proton beams have typically a beam power of a few MW. Present designs of secondary particle production targets will not withstand the power deposition which comes along with the passage of such primary beams. This is at the same time caused by the fact, that in cases, where the secondary flux of charged particles is of interest, the target is kept small in order to minimise the re-absorption, and the deposited energy density is high. The principle concept of a moving target, which provides a new target section for each proton pulse would distribute the power dissipation over a larger volume keeping the effective target small. Moving solid and liquid targets are under investigation (Section 2.3).

## 1.2 A Neutrino Factory

With the experimental evidence of neutrino oscillations at Super-Kamiokande [2] in Japan and Sudbury Neutrino Observatory (SNO) [3] in Canada, the neutrino puzzle is now one of the most interesting topics in particle physics. Oscillations are directly linked to a non-zero mass for at least one of the neutrinos, requiring an extension of the Standard Model. Furthermore, non-zero neutrino masses could lead to a natural explanation of CP-violation.

The Neutrino Factory is based on a new concept for an accelerator that produces a high-intensity, high-energy beam of electron and muon neutrinos. It has been first proposed by S. Geer [4].

The Neutrino Factory will improve the precision of the mass differences  $\Delta m_{13}^2$  and  $\Delta m_{12}^2$  from 10% (planned MINOS and KAMLAND experiments) down to 1%. It will also dramatically increase the sensitive region for the mixing angles  $\sin^2\Theta_{13}$  and  $\sin^2\Theta_{23}$ . Moreover, the Neutrino Factory is a machine that can study the mechanism of CP-violation.

The Neutrino Factory has many scopes that should allow an investigation of a new domain in neutrino physics:

- **High Intensity.** Its flux is  $10^3$  times greater than current man-made neutrino beams.
- **High Energy.** As the number of neutrino interactions increases linearly with the beam energy, the Neutrino Factory features a very high beam energy of 20 to 50 GeV.
- **Two Flavours.** Perfectly suited for oscillation physics, the Neutrino Factory delivers a beam of two flavours (muon neutrino and electron anti-neutrino) at the same time.
- **Two charges.** In the Neutrino Factory, the muon sign can be selected. Thus it is possible to deliver the anti-particles, allowing the search for CP-violation.

The basic concept of the Neutrino Factory is the production of muon neutrinos and electron anti-neutrinos from muon decay. An intense proton beam is delivered to a target, where pions are

produced. These pions are collected in a magnetic field, selecting one charge sign. In a 30 m long section (decay channel) the pions decay into muons. At this stage, the muon beam has a large energy spread and transverse emittance. The energy spread is reduced using phase rotation, while emittance is improved by ionisation cooling. The cooled beam is accelerated in a linac followed by two recirculating linacs to energies of 20 to 50 GeV and injected into a storage ring. This storage ring has two long straight sections that point towards two neutrino detectors. Whenever muons decay in one of the straight sections, each of them produces two neutrinos, which are Lorentz boosted towards one of the detectors, resulting in an intense neutrino beam.

### 1.2.1 Neutrino Physics

Ultimate answers to the questions on neutrino oscillations and CP violation with neutrinos can only be found with an intense, high-energy, human-made neutrino beam.

Out of the many neutrino sources, muons are the most promising mother particles. They have a moderately short lifetime of  $2.2 \mu\text{s}$  that still allows manipulating a muon beam while delivering the decay neutrinos sufficiently fast. The muon decay produces two neutrinos of different flavours, which allows for cross-checking and eliminating beam systematics. If muons of high intensity are produced, accelerated and injected in a storage ring, where they decay, they can produce an intense, well-controlled neutrino beam. This is the concept of the Neutrino Factory [4].

Unfortunately, muons cannot be produced directly, so a precursor particle, the pion has to be produced. The first stage of any neutrino factory is thus a high-power proton driver that shoots protons on a target, where – among other particles – pions are produced. These pions have to be collected and transported. After about 20 m, most pions have decayed into muons. At this stage, the muon beam has a low phase space density and resembles more a cloud than a beam. Its transverse emittance is a million times higher than the LEP beam and it has an energy spread from zero to almost the maximum proton energy. The next step is to create a usable muon beam. Longitudinally, phase rotation is applied to reduce the energy spread (see next Section). As it is not possible to completely eliminate it, the phase rotation is optimised to flatten out the most important part of the energy spectrum, while particles outside the “momentum bite” are lost. Transversally, ionisation cooling is applied to reduce the emittance by a factor of 4. Once the beam is cooled, it can be accelerated to a final energy of 30 to 50 GeV (this is the optimum energy range to allow the detection of neutrino oscillations). This acceleration has to be very fast in order to avoid unnecessary muon decay losses. In the final stage of the Neutrino Factory, the accelerated muons are injected into a storage ring with long straight sections. They decay in the storage ring and whenever they decay in one of the two long straight sections, their decay products contribute to the neutrino beam. In the decay ring, the muons have a Lorentz  $\gamma$  of 300-500, so their lifetime in the lab frame is 0.7-1.1 ms. After a few life times, all muons have decayed and the storage ring is free for the next bunch of muons. This implies a rather high repetition rate of the overall machine, in the range of several tens to hundreds Hz.

In order to maximise the output of the neutrino factory, a bow-tie shaped decay ring is preferred to a racetrack design. The form has the potential to serve two detectors which could be located at different distances to achieve complementary results. The detectors need to have a large mass, as the number of events observed is proportional to the product of the beam intensity times the

detector mass.

### Physics motivation and requirements for a high-intensity neutrino factory

After the exciting results of the Super-Kamiokande and SNO experiments, the flavour changing processes in neutrino propagation (neutrino oscillation) is a phenomenon with solid experimental evidence and implies massive neutrinos [2] [3].

Neutrino oscillations come from the fact that for neutrinos with non-zero mass, there are no reasons that flavours and mass eigenstates coincide. The latter appear in the Schrödinger equation that describes the neutrino propagation in space. From the hypothesis that the flavour base does not correspond to the mass bases, one can express a flavour state as a linear combination of mass eigenstates. As measured at LEP [5], there are only three active neutrino flavours; hence the matrix that describes the relation between neutrino flavour and mass states has to be 3x3: where  $e, \mu, \tau$  are the flavour states, 1 2 3 the mass states associated to the mass  $m_1, m_2$  and  $m_3$ ,  $c_{ij} = \cos\theta_{ij}$  and  $s_{ij} = \sin\theta_{ij}$  with  $\theta_{ij}$  the mixing angle,  $\delta$  the CP violation phase. In total, there are 3 mixing angles, one CP phase and two squared mass differences to be measured.

$$\begin{pmatrix} \nu_e \\ \nu_\mu \\ \nu_\tau \end{pmatrix} = \begin{pmatrix} 1 & 0 & 0 \\ 0 & c_{23} & s_{23} \\ 0 & -s_{23} & c_{23} \end{pmatrix} \begin{pmatrix} c_{13} & 0 & s_{13}e^{-i\delta} \\ 0 & 1 & 0 \\ -s_{13}e^{-i\delta} & 0 & c_{13} \end{pmatrix} \begin{pmatrix} c_{12} & s_{12} & 0 \\ -s_{12} & c_{12} & 0 \\ 0 & 0 & 1 \end{pmatrix} \begin{pmatrix} \nu_1 \\ \nu_2 \\ \nu_3 \end{pmatrix}$$

Once a neutrino is produced, it is in one of the flavour states, but as it propagates, it can turn into another flavour state, according to the probability computed from the Schrödinger equation and quantum mechanics. For example, the probability for a muon neutrino of energy E to turn into a tau neutrino after a distance L in vacuum equals to:

$$P(\nu_\mu \rightarrow \nu_\tau) = \sin^2(2\theta_{23})\sin^2\left(\frac{\Delta m_{13}^2 L}{4E_\nu}\right)$$

where  $\Delta m_{13}^2 = m_1^2 - m_3^2$ . This oscillation probability is non-zero only if the mixing angle and the square mass difference are both non-zero.

Considering a given distance L between source and detector and a given energy spectrum, nature provides a way for measuring  $\theta_{23}$  via atmospheric neutrinos ( $\nu_\mu$  disappearance) and  $\theta_{12}$  from solar neutrinos ( $\nu_e$  disappearance). The only existing limit for the third mixing angle  $\theta_{13}$  comes for the CHOOZ reactor experiment [6] but there is still no experimental evidence that this angle is different from zero.

A number of experiments in the near future will increase the precision in the measurement of the mixing matrix parameters, but still, some important questions will remain unsolved, namely:

- Which is the sign of the mass difference  $\Delta m_{23}^2$ ?
- What is the exact value of the angle  $\theta_{13}$ ?

- Does the CP violation in the leptonic sector exist? And if yes, what is the value of the violating phase delta?

None of the existing available neutrino sources, natural or man made, has the possibility to provide answers to these questions as precisely as the neutrino factory, mostly because one needs a high energy electron neutrino source known with high precision.

A neutrino beam produced from muon decay  $\mu^+ \rightarrow e^+ + \nu_e + \bar{\nu}_\mu$  ( $\mu^- \rightarrow e^- + \bar{\nu}_e + \nu_\mu$ ) at high energy (tenths GeV range) and in controlled condition, such in the case of neutrino factory, would offer the following advantages:

- electron neutrinos at high energy
- the neutrino spectrum is known precisely from the muon energy and polarisation
- the beam is pure since there are two neutrino flavours at the same time but with different leptonic charges

The parameters of the neutrino factory and the detector baselines shall be optimised for the maximum number of oscillation events. The cross section  $\sigma_\nu$  for neutrino interactions grows linearly with energy while the oscillation probability is a function of  $\sin^2 \frac{L}{E}$ . Supposing  $L/E$  constant to optimise the oscillation probability, the number of events is calculated as follows:

$$N_{osc} \sim Flux \sigma_\nu P(\nu_\alpha \rightarrow \nu_\beta) \sim \frac{E_\nu^3}{L^2} \sin^2 \frac{L}{E_\nu} \propto E_\nu,$$

which means that the higher the energy, the more statistics one would have for the measurements. Once the neutrino energy is fixed, the choice of the distance comes from the maximum of the oscillation probability. The natural baseline is limited by the earth diameter. A good compromise for the neutrino energy seems to be 30 – 50 GeV and for the baseline lengths around 2500 and 7000 kilometres to get the right sensitivity to the oscillation parameters.

The signal for oscillations to be looked at in the detector is clear: the neutrino factory produces electron neutrinos and muon anti-neutrinos from positive muons. In the far detector, the charged current interaction of muon anti-neutrinos will produce again positive muons, while electron neutrinos oscillated into muon neutrinos will produce negative muons. The detector must be able to identify electrons, muons and their charges to extract the oscillation parameters. The technique of counting the “wrong sign muons” will permit the measurement of [7]:

- $\theta_{13}$  and  $\theta_{23}$  with the precision of 0.1% or down to limit of about  $10^{-3}$
- CP violation with good sensitivity over the complete LMA (Large Mixing Angle) solution for Solar Neutrinos.
- the sign of the squared mass difference via the MSW effect (see below).

Parameter	Value	Reason
Intensity	$10^{21} \nu/\text{yr}$	Low neutrino cross-section
Min. Energy	30 GeV	Low neutrino cross-section at low energies
Max. Energy	50 GeV	Oscillation maximum must be smaller than earth diameter; CP violation effect is covered by matter effect
Precision beam parameters	1%	To avoid systematic errors, emittance, divergence and intensity must be known to better than 1%

**Table 1.1:** parameters derived from physic requirements

The CP violation phase can be extracted from the difference between the two probabilities  $P(\nu_e \rightarrow \nu_\mu)$  and  $P(\bar{\nu}_e \rightarrow \bar{\nu}_\mu)$ , by changing the sign of the muons produced by the neutrino factory [8]. The advantage of a source like the neutrino factory is that both of the neutrinos of same flavours but opposite helicities are produced in the same condition, cancelling the systematic errors due to limited knowledge of the beam properties.

The sign of the  $\Delta m_{13}^2$  would be extracted from the electron neutrino oscillation. In fact, electron neutrinos interact with matter in a different way than the other flavours, since ordinary matter contains electrons (Mikheyev-Smirnov-Wolfenstein (MSW) effect [9] [10]). Matter would act on electron neutrinos as a birefringent medium would act on one component of polarised light, inducing an extra phase in the neutrino propagation formula, and varying the oscillation probability in vacuum. The effect induced strongly depends on the material density, the distance between source and detector and on the sign of  $\Delta m_{13}^2$ .

The physics requirements can be translated into a table 1.1 of desired machine parameters, that has been presented at NuFact'99 workshop at Lyon [11].

### The CERN Neutrino Factory Concept

The scenario described here is based on the particular situation at CERN. It is intended as a working hypothesis that is partly CERN specific, while dominated by the wish to achieve the required high muon flux [12]. There have been other intensive studies on this subject in the USA [13] and Japan [15].

The upgrade of CERN accelerators to match neutrino factory requirements are proposed in [16] to replace the CERN PS injector complex (50 MeV linac and 1.4 GeV booster) by a linear accelerator, that can act as injector into the PS for the LHC beam. The basic idea to reduce costs is to build the  $\beta \approx 1$  section of this linac with the cavities, klystrons and auxiliary equipment recuperated from LEP. The average beam power of 4 MW with a beam energy of 2.2 GeV appears to be feasible. The HARP experiment [17] will measure the production cross section in this energy range and will produce data by the end of 2002. These results will be crucial in the final assessment of the choice of proton driver.

Protons hitting a target produce pions, which decay very rapidly into muons. The pions depart

from the target in all directions and with a very large energy spread. To make efficient use of the produced pions, it is necessary to collect and guide them. After the pion decay, it is necessary to reduce the muon energy spread and to modify their angular distribution so that they fit into the accelerator acceptance. Only in this way one can produce a beam, which can be accelerated and stored.

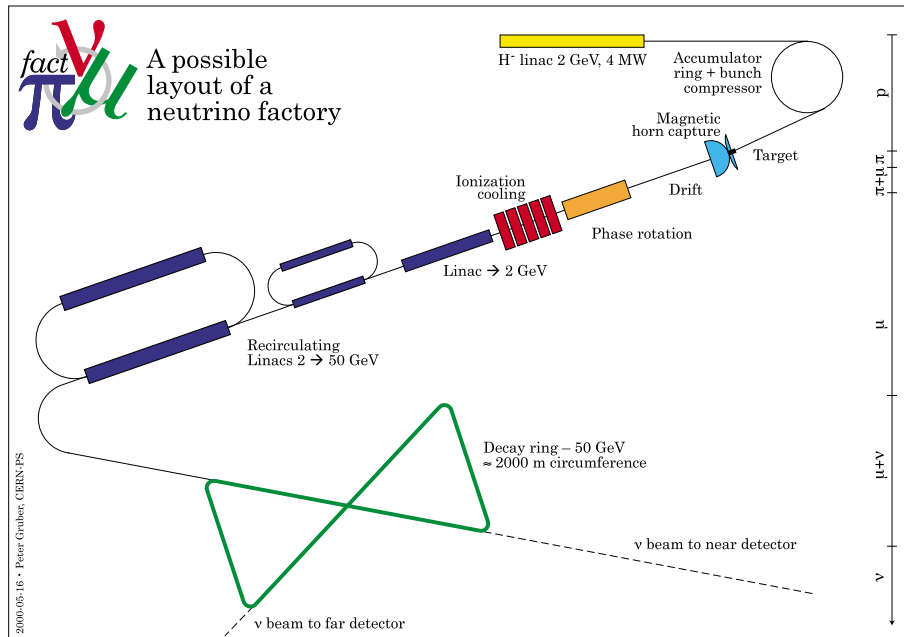


**Figure 1.1:** Schematic of Neutrino Factory showing a triangular decay ring

Reducing the energy spread of a bunch of muons is called “phase rotation” and is basically the acceleration of low energetic muons and the deceleration of high-energy muons. This can be achieved by conventional rf cavities if a phase-energy correlation in the muon beam can be built up, because the acceleration (deceleration) depends on the phase. This is possible with all non-relativistic beams.

Reducing the transverse phase space is called “cooling”, which is achieved by slowing down the muons and accelerating them in the forward direction with rf cavities. The muon lifetime at rest is only  $2.2 \mu\text{s}$  and therefore, fast acceleration using high gradients is necessary to profit from the relativistic increase of their lifetime in the laboratory frame.

To allow for phase rotation, the neutrino factory requires the production of beam pulses consisting of relatively short trains of very short proton bunches. This makes it possible to use bunch rotation to reduce the large energy spread within the muon bunches. The pulse repetition rate must not be too high; otherwise the energy consumption of the subsequent accelerators becomes too high. Also it would be wasteful if a new injection into the storage ring took place before the previous batch had decayed (the ring design employs full-aperture kickers and so injection would kill the previous circulating muon beam). The linac cannot directly provide a suitable beam; hence it will operate with  $H^-$  ions and inject into an accumulator ring, using charge exchange injection to achieve a large circulating proton current. Bunches will be formed in this ring with suitable

rf cavities. They will be transferred into a compressor ring for further shortening of their length. The linac will operate at 50 Hz and initial pulse duration of 2.8 ms at a mean current of 13 mA during the pulse. After accumulation and compression the resulting beam pulse, now shortened to 3.2  $\mu$ s the revolution period in the accumulator and compressor rings - contain a bunch train comprising 140 bunches spaced at 44 MHz frequency. It is assumed that the accumulator and compressor rings will be accommodated in the old ISR tunnel.

This beam will irradiate the production target. About 10-20% of the 4 MW beam power are transferred as heat to the target. Currently, it is planned to use a liquid mercury jet as a target. This jet explodes after the passage of the beam and thus the heat load is carried away with the material while induced activity can be distilled away. The investigation on a liquid metal target is subject of this thesis.

It is necessary to capture the pions produced in the target. At CERN there is considerable experience with magnetic horns, for the collection of anti-protons and in the production of (conventional) neutrino beams. It is therefore worthwhile to investigate the possibility of using a magnetic horn also for the neutrino factory.

An rf system will capture and phase-rotate the muon bunches, and it will also be used in the ionisation cooling of the muon beam in order to compensate the loss of energy of the muon due to ionisation when passing through matter. Further acceleration of the muons to 2 GeV is performed in a special linac with solenoid focusing, followed by more conventional quadrupole focusing. Subsequent acceleration takes place in two Recirculating Linacs (RLA) to an energy of 50 GeV. The muons are then injected into a storage ring (decay ring) where they decay completely. (At 50 GeV, the muon life time is 1 ms and the next beam is injected after 20 ms). The muons decaying in the long straight sections of this ring produce the required neutrino beams. A schematic layout of this CERN reference scenario is presented in Figure 1.1.

### 1.3 Other High Power Target Facilities

A description of the target scenario for a neutrino factory is given in Chapter 2. There are several other designed accelerator complexes, where a target is submitted to a high power proton beam in order to produce a secondary particle beam. A short introduction with emphasis on the target scenario is presented. The most significant differentiation is made by the desired particle production, e.g. charged or neutral particles. In the case of the neutrino factory the production of charged particles, namely pions, is of interest. For other applications the production of neutral particles, namely neutrons, is desired. This fact has impact on the conceptual layout of the target due to different absorption coefficients in matter. In the mentioned accelerator complexes the target is foreseen to be a liquid, either contained in a steel pipe or as a jet, as to withstand the power deposition by the primary proton beam.

- **spallation neutron source**

World-wide there exist several spallation sources. Such machines produce a high flux of neutrons to obtain information on the atomic structure and the excitations of materials by neutron scattering. Presently the most powerful spallation neutron source (SNS) is con-



structed in the USA [1]. The proton beam power is designed to be 5 MW. Not far from CERN, PSI is installing MegaPiE (Megawatt Pilot Target Experiment) [18], a target facility to demonstrate the feasibility of a liquid lead bismuth target for spallation facilities at a beam power level of 1 MW. The presently discussed concepts for accelerator driven systems (ADS) [19] for nuclear waste transmutation foresee similar target concepts as MegaPiE.

- **ISOL (Isotope Separation OnLine) facilities** [20]

Similar to the operational ISOLDE [21] at CERN, a more powerful complex is presently studied. EURISOL [22] is a facility dedicated to the production of a large variety of radioactive ion beams for a great number of different experiments, e.g. in the field of nuclear and atomic physics, solid-state physics, life sciences and material science. The production of fission products where fission is induced by spallation neutrons from the interaction of a proton beam with a converter target [23] is under discussion.

- **muon collider** [24] [25]

The lepton-antilepton colliders built so far have been  $e^+e^-$  colliders like the Large Electron Positron collider (LEP) at CERN and the Linear Collider (SLC) at SLAC. However, electrons are very light and radiate away their energy when accelerated. For a lepton with mass  $m$ , the energy losses per revolution in a circular ring are inversely proportional to  $m^4$ . Hence, the energy loss problem can be solved by using heavy leptons. In practice this means using muons, which have a mass 207 times the electron mass. The resulting enormous reduction in radiative losses enables higher energies to be reached, and smaller collider rings to be used.

# Chapter 2

## The Target Station

The secondary particle flux of pions is produced by a target subjected to a primary proton beam. The pion flux decays into muons, which again decay into neutrinos. Respecting the needed neutrino flux and the restrictions in post-acceleration of muons, the primary proton beam parameters are determined. We will discuss the proton driver and the target station for the CERN scenario as well as for the US-scenario [13], as the experimental results on proton induced shocks are valid for both. The magneto-hydrodynamics caused by the pion focusing device in the US-scenario are another topic of the presented work.

### 2.1 A High Power Proton Beam

A high-power proton beam is used in the neutrino factory to produce pions that decay into muons and later neutrinos. The layout of the CERN Neutrino Factory baseline design leads to a number of requirements for the proton driver:

- **Power**

In order to produce the designed number of  $10^{21}$  muons/year in the decay ring, current estimates (based on current capture efficiencies and losses) show that a beam power of 4 MW is required.

- **Proton energy**

Currently, the pion production cross section is not very well known, and above a threshold energy of 2 GeV, the useful pion spectrum seems to depend only on the proton beam power and not on the proton energy. The HARP experiment at the CERN PS currently measures pion production cross sections for proton energies in the range of 2 – 15 GeV. The results of HARP will determine the preferred proton energy. For the time being we assume a reference energy of 2.2 GeV, as this is the design number given in [16] for the proton driver.

- **Bunch length and spacing**

As the CERN scenario is based on the bunch-to-bucket principle (one proton bunch produces particles that fill one rf bucket at 44 MHz), a very short bunch length of 1 ns rms is

	NuFact <sub>US</sub>	NuFact <sub>CERN</sub>	PSB-ISOLDE	AGS→E951	SNS
$E_p$ [GeV]	24	2.2	1.4	24	~ 0.8
average power <sub>beam</sub> [MW]	1(4)	4	0.003	0.005	~ 5
average current [mA]		0.8	0.002		
rep. rate <sub>pulse</sub> [Hz]	2.5(5)*6	50	0.5	0.33	60
$p^+$ /pulse [ $10^{12}$ ]	16(32)*6	227	32	24	150
$t_{pulse}$ [ $\mu$ s]		3.2	<1.28		< 1
number <sub>bunch</sub>		145	4	6	
$p^+$ /bunch [TP]		1.6	10	4	
$t_{bunch}$ [ns]		5	230		
$t_{bunch\ spacing}$ [ns]		17.5	120	0	
radius <sub>beam</sub> [mm] <sup>1</sup>	1.5	10	3.0/2.0	1.6/0.8 [27]	-
$\rho_{beam\ spot}$ <sup>2</sup> [ $10^{12}p^+/mm^2$ ]	1.4	0.5	1.4	0.8	

**Table 2.1:** Comparison of designed and experimentally used proton beams. Listed are only beam parameters relevant to the target design.

needed. The bunch spacing has to match the rf frequency of the downstream phase rotation and cooling. Furthermore, the train of proton bunches must be shorter than the decay ring.

- **Repetition rate**

Muon life time at 50 GeV allows a repetition rate of < 100 Hz, although the pulsed magnetic horn and the pulsed cavities in the front end make lower rates of < 50 Hz desirable. Power consumption in the front end is largely dominated by the repetition rate.

- **Beam spot size**

The beam spot size at the target is directly related to the target size in order to maximise the pion yield. About  $3\sigma$  of the beam should be within the target, which has a diameter of only centimetres to minimise the pion re-absorption.

In the CERN scenario two different proton driver scenarios are considered [26]: based on a 2.2 GeV linac or an alternative one, based on a 30 GeV synchrotron. An upgraded AGS could serve as a proton driver for the American neutrino factory [13]. This would deliver a proton beam with a higher energy (24 GeV) and a different structure. The proton beam parameters of the scenarios are listed in Table 2.1 together with the ones of present facilities, which have been used for experimental studies.

<sup>1</sup>r.m.s., horizontal/vertical. The radii given are the minimal spot size at maximum intensity.

<sup>2</sup> $\rho_{beam} = \frac{Intensity_{1\sigma}}{r_{beam,r.m.s.}^2 \pi}$

## 2.2 The Target Station

The pion collection device in the vicinity of the target and the target itself are referred to as the 'target station'.

The support facility of the target station consists of a complete high level radioactivity laboratory with the technical support equipment needed to operate and service the target, the spent beam absorber and the first particle collection and focusing device.

It is planned to build it in a modular way so that its individual parts can be rapidly replaced and serviced by means of remote handling. This should allow flexibility in the choice of equipment and allow a stepwise approach in which lower power conventional techniques are used in an early phase and later exchanged against more performing high power targets when developed. The deleterious effects on this equipment and its surroundings caused by radiation induced by the high intensity proton beam is a challenge which makes the target and pion capture system as one of the most crucial items of the neutrino factory.

A molten metal jet target located inside the neck part of a magnetic horn for pion collection has been chosen as the scenario for further investigation of the CERN muon neutrino factory production system. The tentative layout of such a system is shown in Figure 2.1 [28] and will be described in detail below. The scenario chosen by the US Muon Collaboration favours a 20 T super-conducting solenoid as pion collector [13].

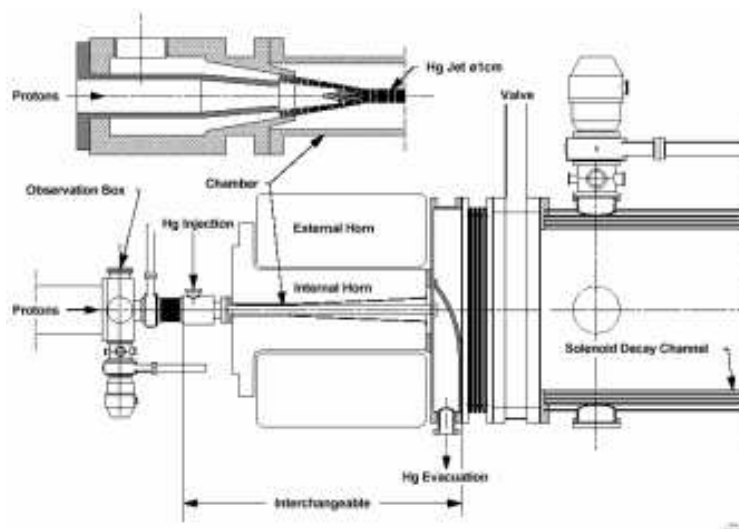


**Figure 2.1:** Layout of a target and magnetic horn-module

### 2.2.1 Pion Collection

In order to maximise the secondary pion collection efficiency, the target needs to be surrounded by a large acceptance pion collection and focusing system. For the pion capture system, in the environment of the target, two scenarios are proposed. The CERN community is presently going for a magnetic horn scheme. The US scenario foresees a 20 Tesla solenoid.

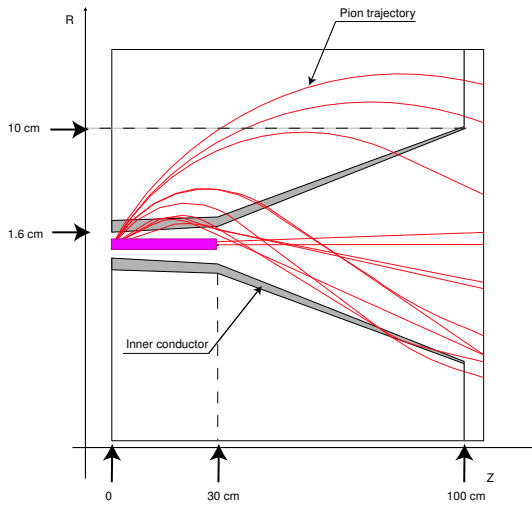


Figure 2.2: pion capture in magnetic horn

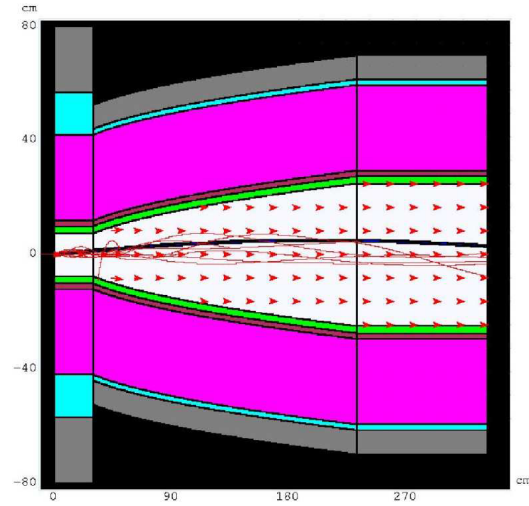


Figure 2.3: pion capture in solenoid

### Cern Scheme

Since one is interested in the production of one sign of pions in any given proton bunch, it is planned to use a pion collection system based on the azimuthal magnetic fields generated between the coaxial conductors of a magnetic horn. This technology has a long tradition at CERN for focusing secondary particles [29] and has the advantage that the parts exposed to the beam are rather simple and inexpensive and that they can be radiation hard. It is therefore a natural choice for CERN.

The horn [30] (Figure 2.2) is compact in the longitudinal dimension (1 m), while the radial dimensions are larger than traditional designs. This choice was dictated by the particular pion spectrum produced by the 2.2 GeV proton beam. Most of the useful particles exit the target radially, with a typical transverse momentum of 250 MeV/c. One needs to bend these particles as soon as possible, which means a small radius of the horn neck, and for a long transverse distance. Since the magnetic field in the horn decreases as  $1/R$ , where  $R$  is the distance between a point in space and the horn axis of symmetry, the focusing effect decreases with the distance. The maximum current is fixed by mechanical and thermal constraints. Limiting factor for this technology is the waist region of the inner conductor. It needs to have a minimum diameter of 5 to 8 cm in order to accommodate the target and its plumbing. The Joule losses in a waist of this diameter raises concerns about cooling followed by the lifetime limitation caused by the magnetic forces of the high current pulse and the possible weakening of the material caused by radiation damage. An experimental study on mechanical lifetime of a full scale horn is presently on-going [31].

### US Scheme

In the US-scheme [13] the capture mechanism considered is a solenoidal magnetic field channel starting at 20 T near the target (Figure 2.3), then falling adiabatically to 1.25 T downstream ( $\approx 18$  m) from the target. In a solenoidal field the pion (and muon) trajectories are helices, with adiabatic invariants  $BR^2$  and  $p_{\perp}^2/B$ . The aim is to capture pions with  $p_{\perp} \leq 225$  MeV/c, for

which an aperture of 7.5 cm is required at 20 T. As the pions to be captured emerge from the target at large angles to the beam, and follow helical paths that may intersect the target at more than one point, it is advantageous for the target to be in the form of a narrow rod, tilted at a small angle to the magnetic axis. Suitable parameters for a mercury target in a 20 T solenoid are a tilt angle of 100 mrad and a target radius of 5 mm.

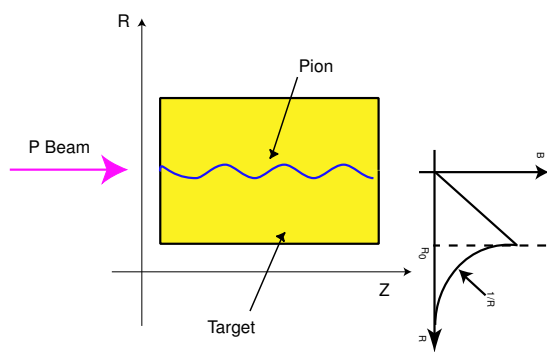


**Figure 2.4:** Pion capture in the conducting target

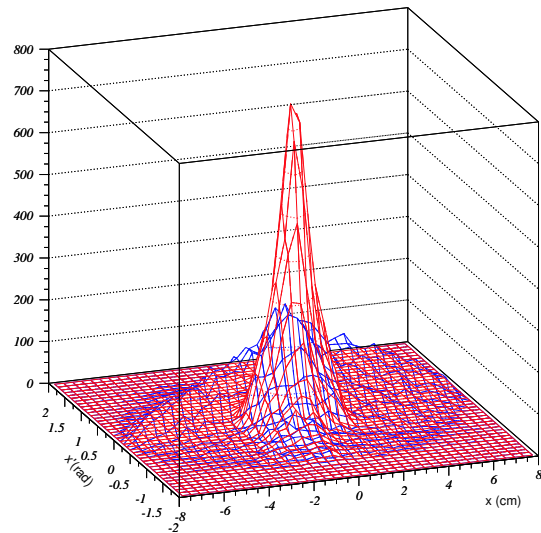


**Figure 2.5:** The emittance decrease of the conducting target. The emittance in the case of the conducting target (red) is smaller compared to case of the solenoid (blue).

### Conducting Target

Similar to lithium lenses developed for the antiproton beams another pion collection concept has been proposed in [32]. In the conducting target a current of about 2 MA is induced. The magnetic field keeps the charged particles within the target (Figure 2.4). The electric losses in the target volume, which are higher than the energy deposition of the proton beam, would result in similar effects as described in Chapter 3. The conducting target is placed in upstream direction outside the magnetic horn, which would eliminate the space restrictions of the magnetic horn. A conducting target can produce a much brighter secondary particle beam than a target magnetised by a solenoid for the same field intensity at the periphery of the target (Figure 2.5).

For the target there are two major constraints issued by the pion collector:

- **Limited space**

The horn has in the bottle neck a minimum radius of  $\sim 2.5$  cm, in the case of the solenoid  $\sim 7.5$  cm. Compared with a diameter of the target in the order of centimetres, space is limited.

- **Magnetic field**

In the case of the solenoid a field of 20 T is in the place of the target. Any moving, conducting target in this field will experience retarding forces. These effects are discussed in Chapter 4.

## 2.3 Options for a High Power Proton Beam Target

Innovative techniques may be needed in order to dispose of the power generated in the small volume of a pion production target where local densities up to  $100 \text{ kW/cm}^{-3}$  may be encountered. A number of ideas were presented at the NuFact'99 workshop and are now under laboratory tests in order to verify the simulations and determine engineering parameters. They should in principle allow the use of pulsed proton driver beams with 4 MW average power and may possibly be extended to 20 MW but a considerable R&D effort is needed in order to select the future directions among the many ideas around.

Targets can primarily be split into two groups: solid and liquid. Today mainly solid targets are used, e.g. for ISOLDE, antiproton beams and secondary beams in experimental areas. These solid targets have always been at rest. Novel concepts demand the dissipation of very high thermal loads in the target due to the high energy deposition of primary proton beams. A new approach compared to the presently used active cooling by liquids/gases flowing around the target, is to exchange the target. Examples are the rotating band or the flow of a liquid target. The expected working principle is similar to the rotating anode of a x-ray tube. The energy is distributed over a larger volume than the effective target. Liquid targets can differ in the layout of the beam window, which is either in contact with the liquid (e.g. SNS target station), or in the concept of a free jet target, where no close-by beam windows are needed.

- **Static Solid Target**

The advantage of solid targets is the fixed shape and therefore the easier handling. Such solids are mostly made of carbon or high z-materials as tungsten. For the application in high power beams they could suffer from the high energy deposition and loose their initial properties (Figure 3.5). The feasibility of a carbon rod as target is under investigation [33]. The carbon composite is particularly interesting because its elastic modulus is unusually high while its coefficient of thermal expansion is nearly zero over a large temperature range.

- **Granular Target**

To reduce thermal internal stresses and to increase the cooling efficiency of a solid target, a novel concept has been proposed by P.Sievers [34]. The granular target is a closed confinement, which contains beads with a diameter  $d$  of a few millimetre (Figure 2.6). Dynamic response, as pressure pulses and vibrations, are greatly reduced in the small target granules due to relatively long beam bursts. The dynamic response delay  $t_s$  is approximated as the time, a pressure wave needs to travel from the centre to the boundary of the target with the velocity of sound  $c$ . Since the proton pulse length  $\tau$  is - by one order of magnitude - longer

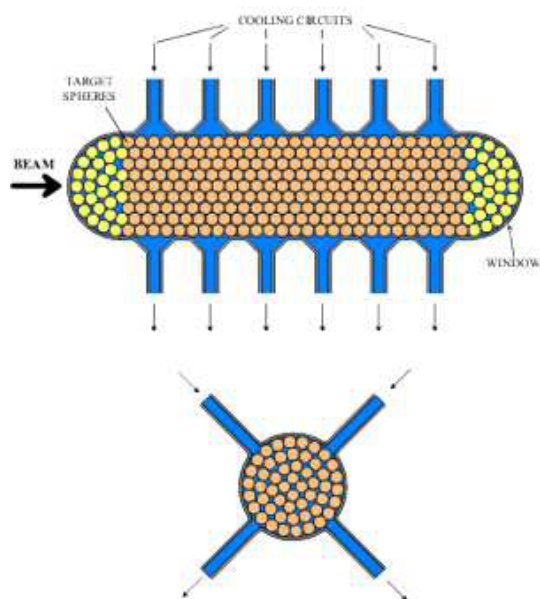


**Figure 2.6:** Layout of the granular target

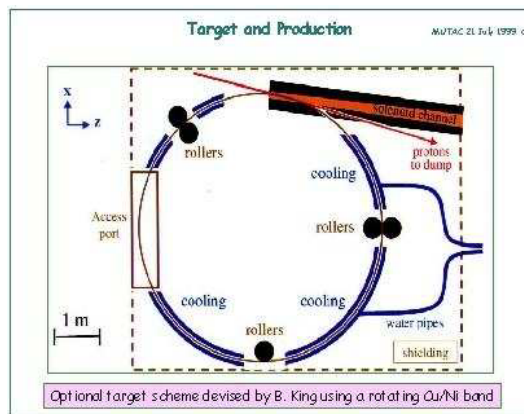


**Figure 2.7:** Layout of the rotating band

than the dynamic response delay  $t_s \approx \frac{d}{2c}$  of the beads, the induced pressure is no longer instantaneous and reduces by a factor  $t_s/\tau$ . At the same time, the enlarged surface increases the surface for cooling and results in smaller thermal stress. Experiments to validate the feasibility of such a target concept are ongoing [35].

- **Moving Solid Target**

The principle of distributing the deposited beam energy over a larger volume for a solid target than the effective target volume could be realised by the rotating band [36] (see Figure 2.7), where the heat is radiated.

- **Liquid Target**

All solid target concepts suffer from the possibility of definitive rupture due to the thermal shocks induced, which demands an exchange of the target. The liquid metal target is a natural solution to the stresses and fatigue induced by the proton beam that eventually lead to the destruction of most solid targets. A liquid flow can be conveniently replaced so that target integrity is restored after exposure to the proton beam.

- **Confined liquid target**

The concept of a contained liquid metal flow is presently foreseen for the SNS target. The flow of the target material keeps the temperature in the circulating medium below 100 °C. A major concern is the beam window of the steel container in direct contact with the liquid. The incident proton beam causes thermal shocks corresponding to pressure waves in the order of MPa. The resulting cavitation releases material from the beam window and weakens the confinement, which might lead to undesirable break-down. This effect has been observed in ISOLDE targets (Figure 3.11) and is presently under investigation in the USA [37].

- **Jet target**

The liquid jet has the advantages of avoiding any near-by beam windows. From a



nozzle placed close to the entrance of the horn a liquid jet is injected into the interaction region. The intercepting proton beam produces the pions. Further the heated liquid is collected and recirculated to a reservoir and back to the nozzle. In this way, the deposited heat is automatically removed from the interaction region of proton beam and target. A liquid jet would establish a new target for each proton pulse if the material disrupted by the proton beam can be evacuated within the proton pulse interval and provided the jet velocity is large enough.

In cooperation with other laboratories CERN has started a study on some of the many technological challenges of a neutrino factory. A major issue of the facility is the pion production target. At CERN the choice was made to investigate a liquid metal jet target - the topic of the present work.

The choice of a high atomic  $Z$  target material is favoured due to a shorter target length. High density reduces the physical length of the target and influences the design of the pion capture system, the spread in time of the resulting  $\pi$ -burst, and the absolute pion production [38]. The target approximates better a point like source for the focusing device. The length of a carbon target would be already in the order of 1 m. As a liquid is needed, preferable at ambient temperature for easier handling, mercury is one of the top candidates. Other possibilities are metals with a very low melting point like eutectic metals, a composition of lead and bismuth. Eutectic metals are used in the target for MegaPiE [18].

The free flying jet provides an easy solution for the rapid exchange of the target for each proton pulse, and avoids the problem caused by rupture of the target due to the high power deposition. The needed jet velocity is given by the beam repetition rate  $f = 50$  Hz and the affected target length of the jet. For the pion yield after capture an optimum is achieved with a target length of  $2 \lambda_{Hg} \approx 30$  cm. If one target length should be exchanged within the passage of two proton pulses, the speed of the jet has to be  $> 15$  m/s. The upper limit is given by the technical possibilities to establish such a jet. One target length of a mercury jet with a radius of 1 cm has a volume of  $\sim 1$  litre. The power stored in such a jet is a few tens kilowatt.

Experiments performed at BNL (USA) and at CERN revealed the behaviour of a liquid with free surface submitted to a proton beam. The numerical results and the impact on the design for a 4 MW target for a neutrino factory are presented in chapter 3.

The advantages of a mercury jet target can be summarised in the following list:

- High pion yield (high  $Z$ )
- Liquid at ambient temperature (no liquid-to-solid phase change issues)
- The majority of the radioactive reaction products may be concentrated and removed from the Hg by distillation
- No confinement tubing (free flowing jet)
- No need for near by beam windows (differential pumping confinement)

The disadvantage of the jet target is given by the fact, that its feasibility has not been shown so far. The jet target is a novel concept, which has been proposed only a few years ago. Towards

the application in high power proton schemes, the feasibility has to be studied. The R&D work within the Neutrino Factory Collaboration in Europe and the US for a jet target within the last two years is presented here.

## 2.4 Feasibility Study of a Liquid Metal Jet Target

The possibilities of a liquid metal target as a pion production target for a Neutrino Factory have been investigated experimentally. These experiments concern the interaction of a liquid metal with a proton beam and the effects on the liquid metal in a 20 T magnetic field.

The characteristics of the proton driver define their constraints on the pion production target. The interaction between mercury, selected as a generic liquid metal, and a proton beam were observed with static mercury at the ISOLDE facility and with free mercury jets at the AGS/BNL. to estimate the impact on the high power proton target of a full scale neutrino factory and to benchmark hydrodynamic simulation codes. The partial and local derivatives (scaling laws) on the proton pulse parameters (intensity, spot size, ...) are presented in chapter 3.

The liquid metal jet injected into the pion focusing system of the US scheme exposes the moving metal to a high magnetic field. The magnetic forces on the target might result in undesired deformation and rejection. In cooperation with the High Magnetic Field Laboratory [39] at Grenoble an experiment to observe magneto-hydrodynamic effects of a free jet was established. A mercury jet with a velocity of up to 15 m/s was injected into a 20 T solenoid. The observations of magneto-hydrodynamics are presented in chapter 4.

## Chapter 3

# Proton Induced Shocks

It has become apparent to high-energy physicists over the past few years that the physics opportunities available to the community provided by intense muon beams are significant. Recent examples include the concept of a machine based on  $\mu^+\mu^-$  colliding beams and even more recently of an intense neutrino beam resulting from the decay of muons circulating in a storage ring. Each of these applications calls for a scenario [40] in which muons are generated from a beam of pions which are in turn generated by impinging an intense proton beam on a target. For this scenario, the intensity of the resulting muon beam is directly proportional to the power of the proton beam which initiates the process. Questions arise about the viability of targets to withstand the high beam power required to generate the desired pions.

Considering that a high intensity proton beam is required in order to generate the required muons, the choice of the target material becomes a particularly important issue. One is confronted with conflicting demands, namely a target material and geometry capable of producing copious pions while minimising their absorption once they are produced. Modelling studies point to high-Z materials being more efficient at producing pions of both signs, whereas low-Z materials are better in avoiding the absorption of the produced pions. Carbon has the advantage of permitting larger target cross-sections and therefore larger beam spot sizes with a corresponding decrease in shock heating due to high peak energy depositions. The muon collider collaboration is considering another approach, however, which is to retain the pion production advantage from high-Z materials by utilising a free liquid mercury jet. In this case, the jet can be conveniently replaced so that target integrity after exposure to the proton beam is not an issue.

To study the interaction of a liquid metal with a proton beam a static mercury target and a mercury jet with free surface have been exposed to a proton beam at the AGS, BNL (experiment E951) [41] and at the PS booster at CERN (ISOLDE, no dedicated experimental proposal). Mercury was chosen as one of the room temperature liquid metals. The energy deposition density approached 100 J/g, which is not sufficient to reach the boiling point of mercury. Diagnostics included a high-speed photography of the liquid targets. The experimental setups are based on the recording of the shadow of the mercury, intercepting a laser light source, with a high speed camera. The proposed experiment aims at measuring the droplet velocities of the splashes result-

ing from proton-induced shocks in mercury under very precisely defined beam parameters. The behaviour of the free surface of a mercury target been investigated as a function of various proton beam parameters in order to make it possible to extrapolate to designed scenarios. With these observations one can estimate the behaviour of the mercury jet target inside the pion collection system of a neutrino factory. This work is part of the R&D program of the Neutrino Factory and Muon Collider Collaboration.

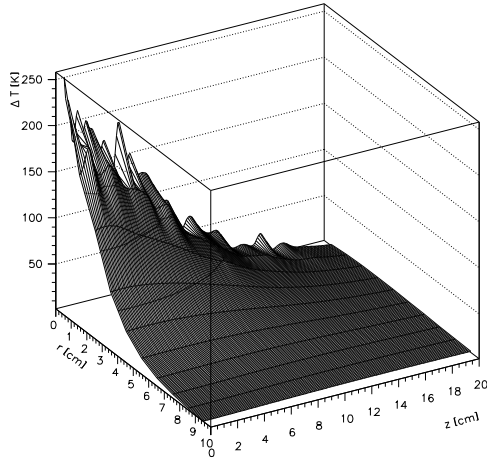


**Figure 3.1:** Temperature profile (simulation) of a high-Z target (1.4 GeV proton beam,  $30 \cdot 10^{12}$  protons/pulse,  $r_{r.m.s.} = 2.2$  mm)

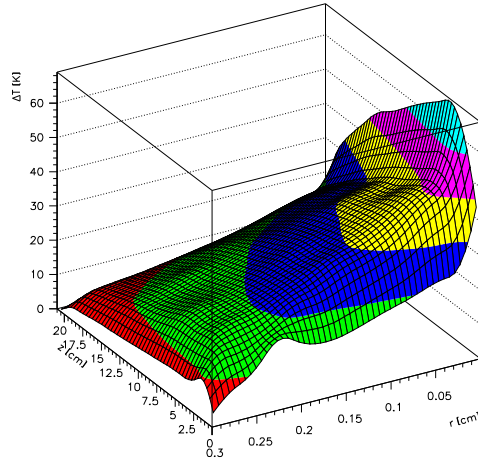


**Figure 3.2:** Temperature profile (simulation) of an aluminium rod (1.4 GeV proton beam,  $3 \cdot 10^{13}$  protons/pulse,  $r_{r.m.s.} = 2.2$  mm)

### 3.1 Solid Targets

The energy deposition of a proton beam causes a temperature rise in a target of a few hundred Kelvin (Figure 3.1). Today commonly used are solid targets, e.g. cylinders of carbon or heavy metals. The thermal expansion can cause undesired operational states (compare Figure 3.3 and 3.4) or distortion (Figure 3.5) of solid targets. The neutron converter (Figure 3.3) for ISOLDE consists of a cylindrical proton target (lower cylinder), where the produced neutrons cause fission released radio-isotopes in the secondary target. It has been observed, that the proton beam ( $\approx 10^5$  pulses) caused a shift of the this cylinder by  $\approx 2$  cm (Figure 3.4), which is mostly likely due to the thermally induced vibrations.

To study the kinetic energy transfer a simple experiment was proposed. A pendulum will serve as the solid target. A high-speed camera system served as the tool of observation. This optical system is described in detail in section 3.3.4. A total of 12 single proton pulses with an intensity of  $3 \cdot 10^{13}$  protons have been submitted to the target. The proper environment to perform this experiment without a large effort is the target area of ISOLDE (see section 3.3.1). Thermal induced vibrations and the verification of the optical diagnostics are the motivation of such an in situ experimental method.

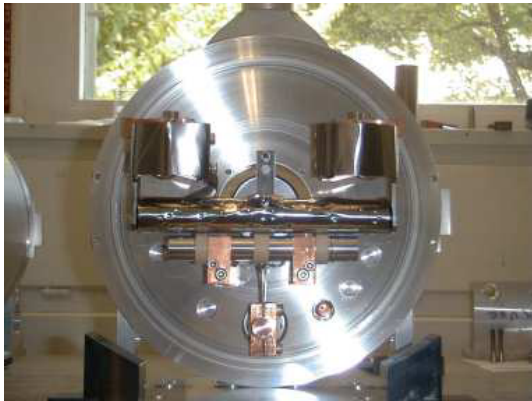


**Figure 3.3:** ISOLDE target UC<sub>2</sub>-208, before irradiation ...



**Figure 3.4:** ... and after, where the cylindrical target (lower cylinder) is shifted by about 2 cm in forward direction of the beam.

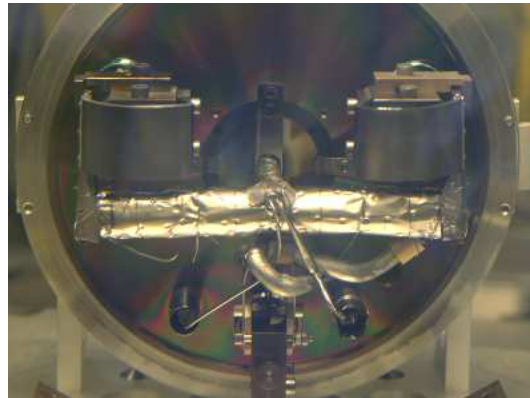


**Figure 3.5:** Distorted n-converter. Due to the thermal heating by the proton beam ( $10^{18}$  protons, 1.4 GeV) the rod has been deformed from its original straight form.

A cylindrical Aluminium target ( $d = 6 \text{ mm}, l = 20 \text{ cm}$ ) is free hanging on two 0.94 m long Tungsten wires ( $\text{Ø}100 \mu\text{m}$ ). This configuration allows the pendulum to move in all directions, while other solid targets, e.g. the carbon tests described in [33] or the ISOLDE neutron converter mentioned above were fixed. The radius of the proton beam spot size was  $r_{r.m.s} = 2.2 \text{ mm}$  and the diameter of the the target was chosen to be about one and a half times larger. To assure a relaxation of the target between two successive events, a delay of 10 minutes was respected. The pendulum target was placed in the GPS area of ISOLDE. 12 proton pulses (intensity  $3 * 10^{13}$  protons) impinged coaxially with the target cylinder (Figure 3.6). The pulse length was set to  $1.3 \mu\text{s}$ .

The camera can detect movements larger than  $0.075 \text{ mm/s}$ . The record rate is 8000 frames/second (shutter time  $12.5 \mu\text{s}$ ). The shadow photography allowed an observation of a movement in y- and z-direction.

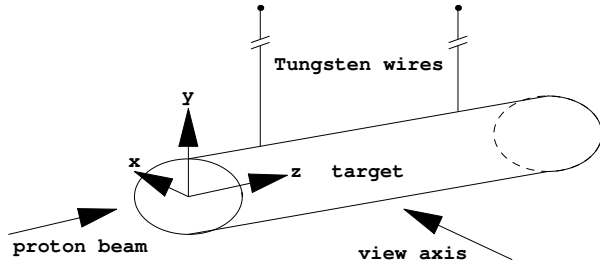


**Figure 3.6:** Schema of pendulum target

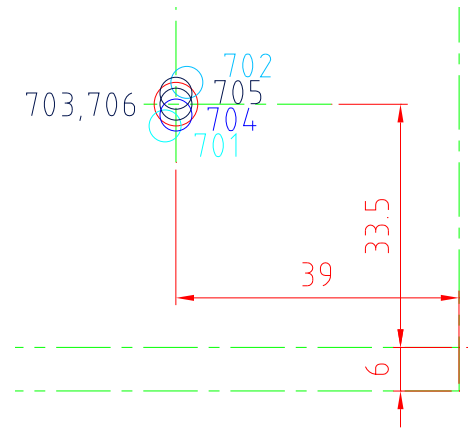


**Figure 3.7:** Beam position relative to the pendulum target (red circle) for the various events.

For the movement of the pendulum in horizontal plane its corresponding eigenfrequency  $f = \frac{1}{2\pi} \sqrt{\frac{g}{l}} = 0.514 \text{ Hz}$  ( $t = 1.945 \text{ s}$ ) has never been observed. The maximum amplitude for the pendulum in horizontal plane was a few centimetre in beam direction and  $\pm 30 \text{ mm}$  perpendicular to it. The digital image processing revealed no movement of the cylinder in beam direction. The movement in y-direction was with - no understatement - a surprise. Figure 3.8 shows the vertical movement of the pendulum for the different events. In Figure 3.9 the maximum amplitude and the initial velocity, which are directly proportional, are plotted. The absence of an expected correlation between amplitude and velocity like  $v = \sqrt{2gh}$  can be explained by the elasticity of the Tungsten wires, which acted like springs. An oscillation amplitude of about 4 mm needs a initial velocity of about 0.28 m/s in absence of additional acceleration, and an initial velocity of about 0.14 m/s would result in a height of about 1 mm. Due to the low velocities we neglect air friction in these considerations. The spectrum of the vertical eigenfrequency is shown in Figure 3.10. Dominant eigenfrequency is  $f \approx 13 \text{ Hz}$ .

The movement in vertical direction can be explained by radial asymmetrical heating of the target rod. The asymmetric heating of the pendulum by the proton beam would cause a curvature of it. An aluminium foil was placed in front of the target, its activation was measured afterwards and confirmed the proper positioning of the beam within millimetres. An asymmetric averaged heating at one side of the pendulum by about 30 K (Figure 3.2) results in a curvature with a radius of  $\approx 3.3 \text{ m}$  with a maximum deviation of  $s \approx 1.6 \text{ mm}$  from the straight target.

The radial dilatation can cause a velocity  $v$  of meter/second. This dilatation is much smaller because the radius  $r$  is minor compared to the target length, but at the same time, the delay  $t \propto \frac{r}{c}$  of expansion,  $c$  being the sound velocity, is much shorter [42].

This effect will be studied in more detail in a forthcoming experiment in ISOLDE. The thermal expansion and the resulting oscillations of two different solid target configurations, namely a single rod and the granular target, will be compared [35]. For future investigation the use of a laser vibrometer is envisaged, as such a tool is more suitable to reveal information on the vibration modes of a solid target. The setup will be similar to the strain measurements on carbon and INVAR targets performed at BNL using laser strain gauges [33].

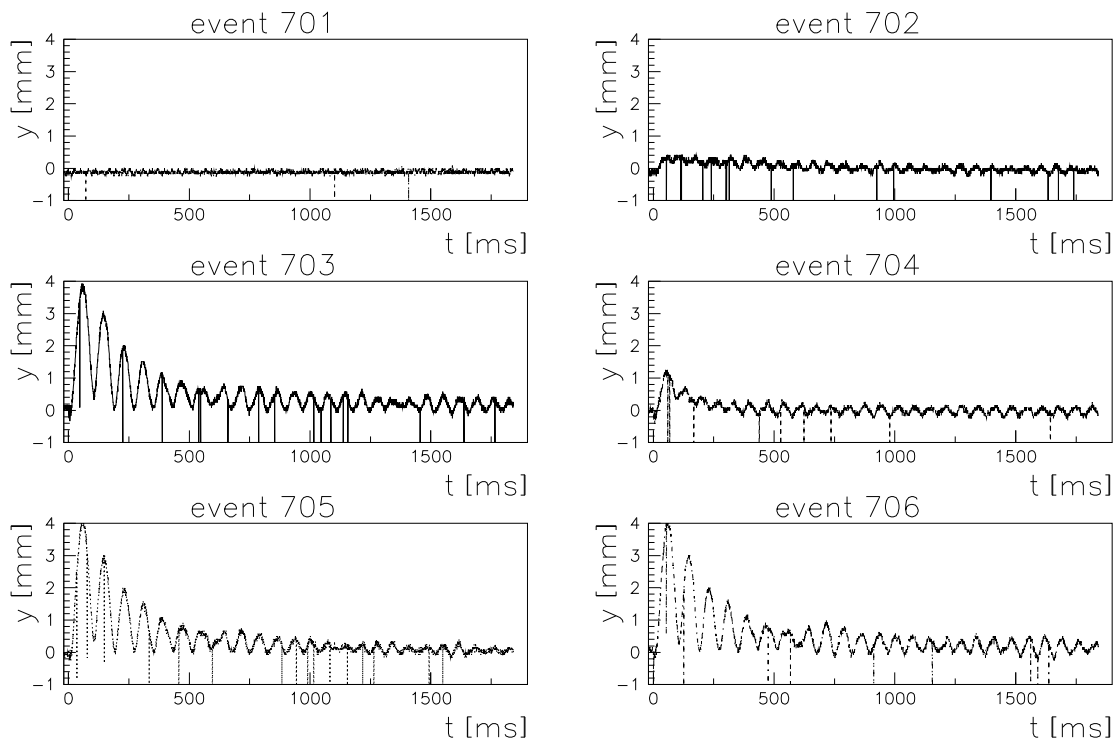


**Figure 3.8:** Vertical movement of the pendulum. The oscillation is shown for various impact positions shown in Figure 3.7. The frequency spectrum is shown in Figure 3.10.

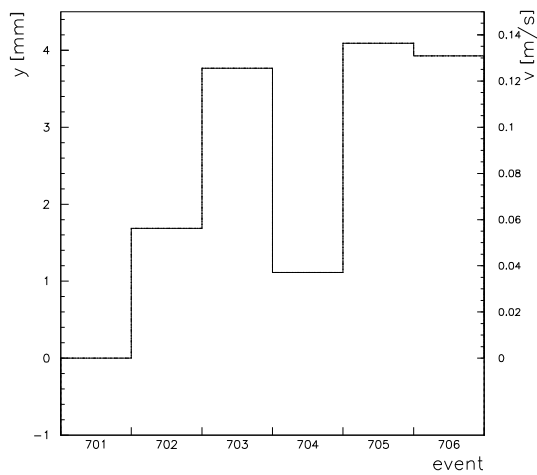


**Figure 3.9:** Oscillation height and initial velocity of the pendulum.

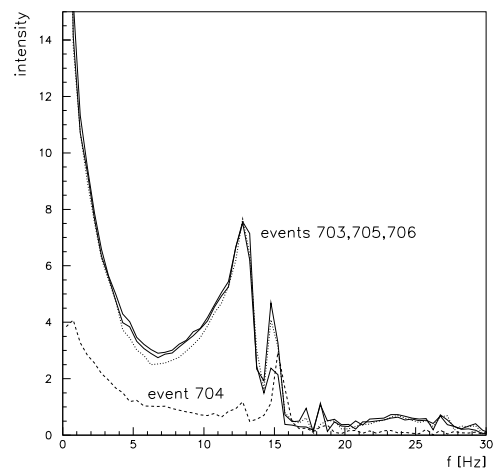


**Figure 3.10:** The frequency spectrum for the vertical oscillation of the pendulum.

## 3.2 Liquid Targets

Thermal shocks induced by proton pulses were observed in each ISOLDE molten metals submitted to the PS-Booster beam and eventually lead to their destruction. The thermal induced pressure wave in liquid targets possibly ruptures the confinement (Figure 3.11) [43]. Radioactive ion beam production resumed after modification of the target containers, doubling of the beam spot size, staggering the extraction of 3 booster rings and reducing the proton intensity to 2/3 of its nominal value. While these effects were qualitatively understood, the step towards higher proton beam intensities and other pulse structures such as full intensity of the PS-booster, EURISOL and  $\nu$ -factories, requires modelling and experimental benchmarks.

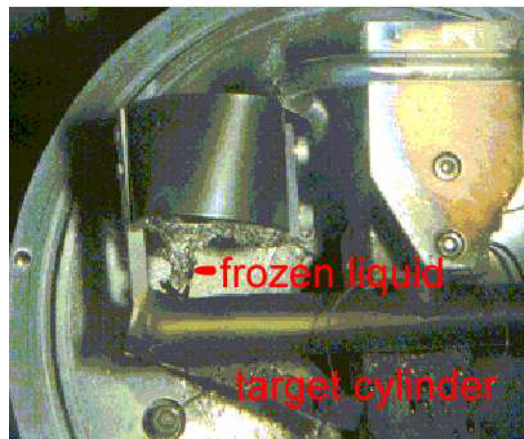


**Figure 3.11:** Broken confinement of a liquid metal target. The shock waves induced by the proton beam caused the break-down of the confinement. The ejected and frozen liquid can be seen.

Following the thimble/jet tests at BNL performed in spring 2001, extended measurements with a larger variation of beam parameters were done in the thimble and trough tests at ISOLDE/CERN in summer 2001 and spring 2002 (Table 3.1). The contents has been published in [33] [44] [45] [46].

## 3.3 Experimental Layout

The interaction between a free surface liquid metal and a proton beam were observed with static mercury as well as with a mercury jet and up to  $32 \times 10^{12}$  protons/bunch. The final design of the high power proton beam target foresees a liquid mercury jet. In order to simplify the experimental setups, different liquid target configurations than a jet have been designed, which are explained in detail in section 3.3.2. Three different target configurations have been exposed to two different proton beams with different proton energies (Table 3.1).



date	site	beam	target configuration
April 2001	BNL	AGS	thimble
April 2001	BNL	AGS	jet
August 2001	CERN	PSB	thimble
April 2002	CERN	PSB	trough

**Table 3.1:** Series of experiments on proton induced shocks. The notation of the different target configurations is explained in section 3.3.2

	PSB	AGS
energy $_{p^+}$ [GeV]	1.4	24
intensity/pulse [ $10^{12}$ protons]	1-32	0.6-4
bunches/pulse	1-4	1
intensity/bunch [ $10^{12}$ protons]	1-8	0.6-4
bunch length [ns]	180-230	150
pulse length [ns]	1300-	-
bunch spacing [ns]	350-	-
spot size $r_{r.m.s.}$ [mm]	> 2.2	0.8/1 [27]

**Table 3.2:** Beam parameters of PSB and AGS at target station

### 3.3.1 AGS and PSB Test Areas

Table 3.2 indicates the various beam parameters of the synchrotron facilities Brookhaven Alternating Gradient Synchrotron (AGS) and the CERN Proton Synchrotron Booster (PSB). For the performed experiments these parameters have been varied within their limits in order to extract scaling laws for the behaviour of a liquid target. As in a neutrino factory the target volume will be renewed for each proton pulse, the test experiment can be carried out at much lower repetition rate. In fact, the mercury targets in the experiments have been exposed to single pulse events at time intervals larger than ten minutes to allow self-cooling of the mercury.

#### PS booster

The PS booster (PSB) can vary its beam parameters over a large range (Table 3.2). Some additional features of the PS booster [47] are relevant for further discussion:

- Intensity of ring 2 (i.e. 3 rd bunch in a standard extraction) can go up to  $1 \cdot 10^{13}$  protons/pulse.
- The minimum bunch spacing is determined by the rise time of the recombination kickers that is specified at 100 ns. A reserve of 20 ns should be added.
- The maximum bunch spacing is determined by the flat-top of the recombination kicker BT.KFA20 that has to support bunches from two rings. The flat-top is specified at 2700 ns,

subtracting one bunch length of 230 ns and a reserve of 70 ns gives 2400 ns spacing.

- Bunch spacing can be varied quasi-continuous within the above-mentioned limits but the process requires various adjustments and is relatively time-consuming.
- For a bunch spacing of more than 2400 ns, the so-called “staggered ejection mode” might be considered. This would allow a spacing of (theoretically) up to a few 100  $\mu$ s at the expense of having only 3 bunches (rings 2,3,4) available from the Booster.

The beam spot size was calibrated in advance by a SEM-grid placed at the designed point of interaction between mercury and proton beam for various quadrupole settings. Figure 3.12 shows the spot size as a function of intensity, where the quadrupole settings are kept constant.

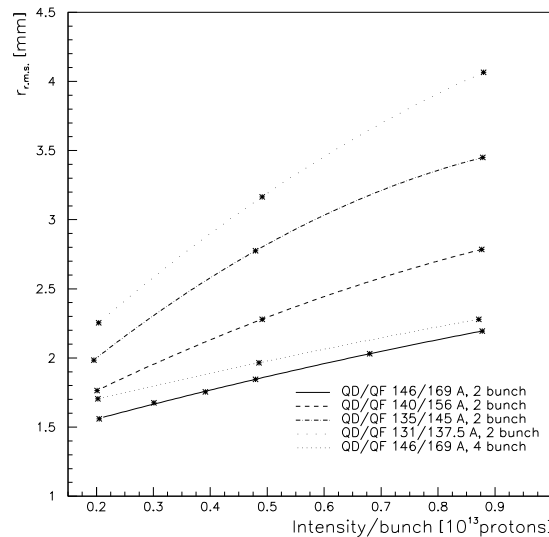


**Figure 3.12:** The beam spot size at the GPS target station as a function of the intensity and fixed quadrupole settings. The use of four instead of two bunches/pulse modifies the spotsizes slightly.

The beam from the PS booster can be extracted to the ISOLDE target area. Two target stations, namely GPS and HRS are designed in a modular way in order to place various types of targets. Figure 3.13 shows a sketch of the ISOLDE target area with the positions of target, and optical equipment used for diagnostics is indicated, both for the use of GPS or HRS. Due to the higher radiation level in HRS and the needed personal access to the target zones, only GPS was used for the discussed experiments.

**AGS**

Experiment E951 [41] has been approved for running at the Brookhaven Alternating Gradient Synchrotron. The A3 beam line [48] in the experimental hall has been configured for the transport of primary 24 GeV protons extracted from the AGS. All targets have been mounted inside a stainless steel vessel which prevents the potential dispersal of activated fragments which could be ejected from the tested target. This target system is placed on a translation table which has a target flag mounted to one side to facilitate the tuning of the proton beam prior to the target being moved into position. Measured beam rms spot sizes typically were on the order of  $\sigma_x = 1.6$  mm and  $\sigma_y = 0.9$  mm. Beam intensities were monitored by a series of beam transformers extending from the AGS extraction point to immediately preceding the target table. Intensities were adjustable from  $0.5$  to  $4.0 \times 10^{12}$  protons/pulse with full bunch beam lengths typically 150 ns.

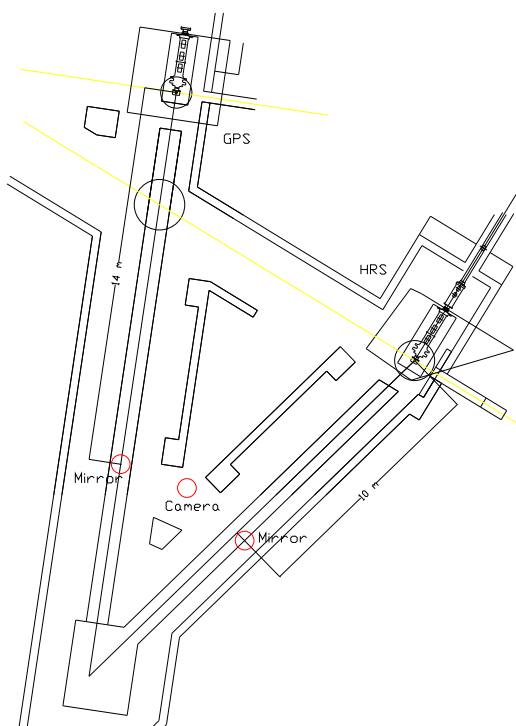


**Figure 3.13:** Isolde target area

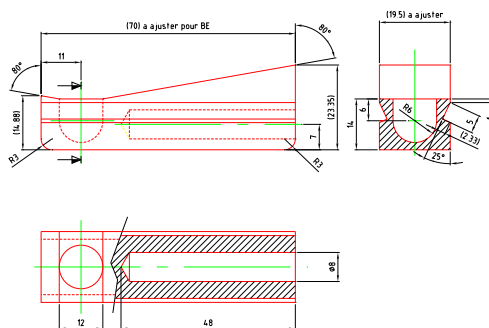


**Figure 3.14:** Layout of the thimble

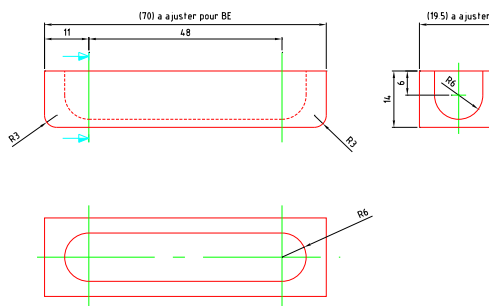


**Figure 3.15:** Layout of the trough

**3.3.2 Mercury Test Targets**

Three different target configurations, a thimble, a trough filled with mercury and a mercury jet, have been exposed to a proton beam. This was done to minimise the radioactive waste production in such studies. As experiments for both setups under the same conditions were performed, their results can be compared.

The mercury is contained in a thimble or a trough machined in a 316LN stainless steel frame.

Three confinement layers prevent any leakage: A first layer of quartzglas confines the mercury splash, an additional layer of Makrolon was mounted as backup (Figure 3.16); The steel frame with the double window was contained in an outer confinement (Figure 3.17). The trough and the thimble are placed on an ISOLDE vacuum vessel support and positioned on the front-end identically to an ISOLDE target. A technical description can be found in [49]. All mercury targets contained a 1 bar Argon atmosphere. There were no monitoring of pressure or temperature inside the experimental chamber described here. The only diagnostics is the high speed camera system described in section 3.3.4.

**Thimble:** The thimble is presented in Figure 3.16. The central window in the steel frame hosts the target place for the liquid metal, the thimble. The larger flanges, located at the beam height, are the beam entrance and exit windows, which were demanded by the safety group to connect additional beam windows than the steel frame itself. The two upper flanges serve as connections to the target space to fill the mercury and, if desired, to apply a vacuum. In the front and the back two window flanges are mounted, which make it possible to view the process through quartz windows. The amount of mercury, which is irradiated, is small, as no spare material for circulation is needed. The volume of the thimble excavated in a stainless steel frame is  $1.3 \text{ cm}^3$ . It consists from bottom to top (Figure 3.14) of a half sphere ( $r = 6 \text{ mm}$ ), a vertical cylinder ( $r = h = 6 \text{ mm}$ ), and a meniscus, which has a free surface of  $1.2 \text{ cm}^2$ . The mercury has a free surface in up-direction, where it can expand to. The proton beam interacted with the mercury along  $12 \text{ mm}$ . The atmosphere was 1 bar Argon. The 'explosion' can be viewed through two viewing windows placed on either side of the steel frame.

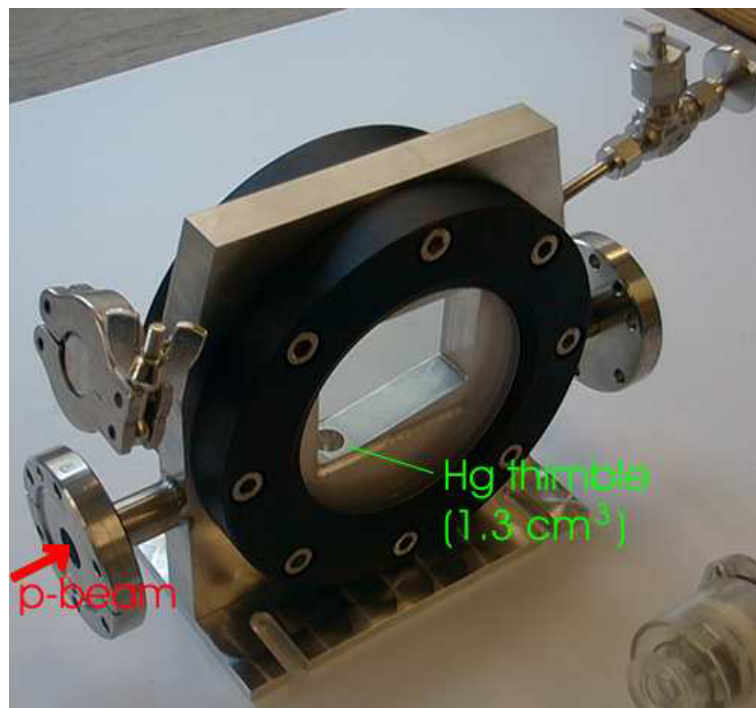


**Figure 3.16:** Mercury thimble

**Trough:** Figure 3.17 shows the trough within the second confinement. The trough (Figure 3.15) is more or less a cylinder of  $d = 12 \text{ mm}$  in vertical direction and an interaction length of  $l =$

60 mm. The volume of mercury put in is  $7.3 \text{ cm}^3$ . This is excluding the meniscus ( $< 1 \text{ cm}^3$ ). A detailed list of all parts including material properties and their functionality are given in [49]. The short interaction length in the case of the thimble did not allow an observation of the shower development in the mercury volume. The extraction of the behaviour of the mercury splash as a function along the z-axis is possible by using the trough.

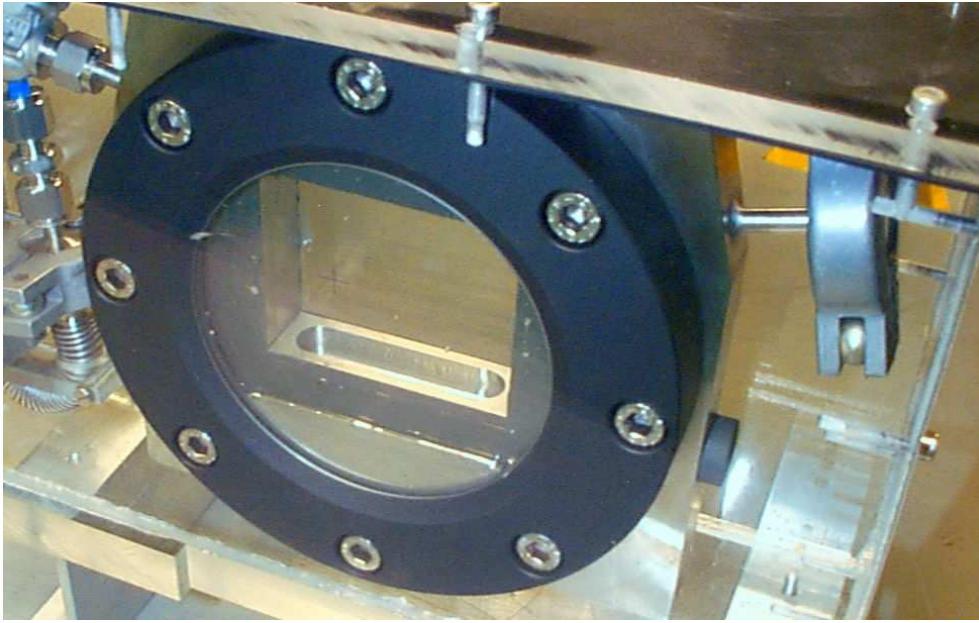


**Figure 3.17:** Trough target. The trough is excavated in a steel frame, with the viewing windows on both sides. The steel frame is placed in a second confinement.

**Jet:** The mercury jet (Fig. 3.18) was formed by supplying a pneumatic pressure of 1.8 bar which forced the mercury out of a 1 cm diameter nozzle inclined at  $18.5^\circ$ . The resulting mercury stream travels 20 cm to its maximum height at which point the trajectory of the Hg jet overlaps with the proton beam for 19 cm. The average velocity of the jet was 2.5 m/s. The diameter of the jet at the interaction point fluctuated between 0.7 and 1.7 cm. The mercury jet was established for several seconds, so quasi-continuous in respect to the proton pulse length and the mercury splash duration.

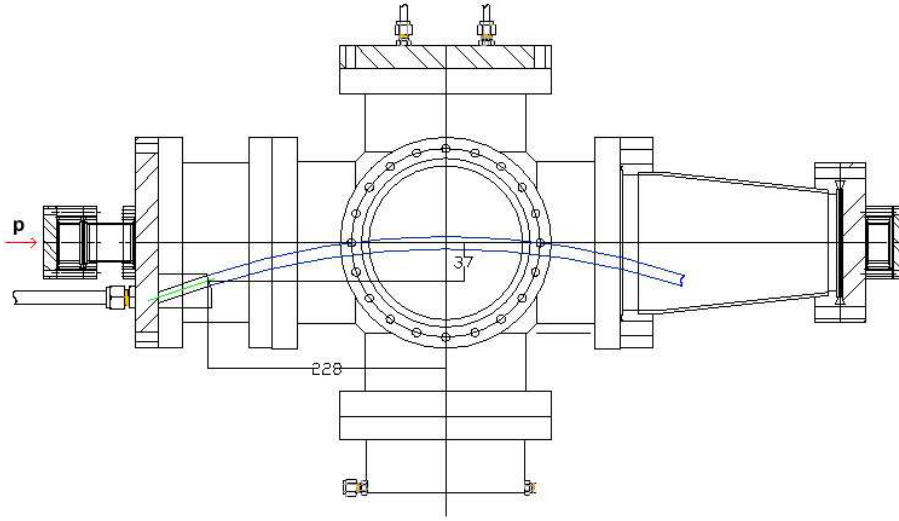


**Figure 3.18:** Elevation view of the Hg jet overlapping with the 24 GeV proton beam.

### 3.3.3 Simulation of the Energy Deposition

The proton beam profile was measured to be Gaussian. In Figure 3.19 the beam profile, its integral  $A \int e^{-\frac{r^2}{2\sigma^2}} dr$  and the folded function of beam profile and beam area is shown. The folded function shows the low number of protons in the centre of the beam. The number of protons within a radius  $r_a$  is defined as

$$N_p = 2\pi A \int_0^{r_a} e^{-\frac{r^2}{2\sigma^2}} r dr, \quad (3.1)$$

where  $\sigma$  is the variance of the beam spot size measured by the SEM-grid and  $A = \frac{N_p}{2\pi r}$  the normalisation.

Using the simulation code MARS [50] the energy deposition for the various target configurations mentioned above was simulated. Target, thimble and jet do have the same cross sectional layout ( $d \approx 12$  mm) and the resulting shower development is similar in the three cases for a given proton energy. The difference in target length of course implies for e.g. the thimble that it represents only the first part of a full jet. The largest energy deposition density occurs within the first centimetres. The surrounding steel with a thickness of a few millimetre in the case of thimble and trough are negligible concerning the energy deposition, as such steel corresponds to a minor layer of mercury (one order of magnitude less). The impact of the steel frame on splash velocities - as the free surface is reduced - is discussed later.

The two different proton energies change the energy deposition profile such, that the maximum is shifted a few centimetres downstream in the case of 24 GeV. In the case of 1.4 GeV protons the maximum is located at the beam entrance to the target and the energy is down to half the value after  $\approx 6$  cm. For a 24 GeV proton pulse with an intensity of  $4 \cdot 10^{12}$  protons and a spot

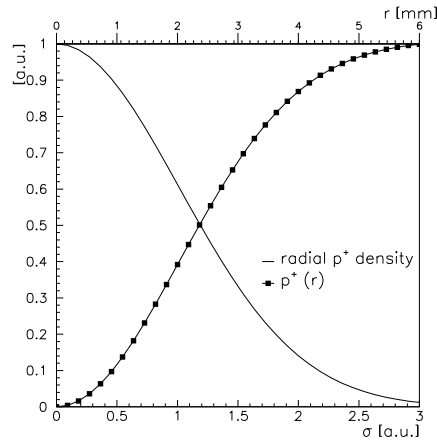


**Figure 3.19:** Transverse proton density and integrated proton number as a function of radius  $r$ .

size radius of 1 mm (r.m.s.) the main characteristics are an average temperature rise in the target centre of 200 K for the thimble and 300 K for the jet target (Figure 3.20 and 3.21). The average temperature rise overall is 57 K (thimble) and 65 K (jet). Figure 3.20-3.23 show the simulated temperature distribution of a single pulse in a mercury target for different target configurations and proton energies.

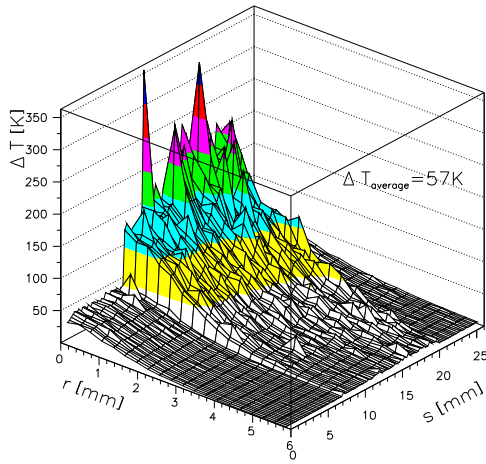


**Figure 3.20:** temperature profile for the thimble, 24 GeV,  $4 \cdot 10^{12}$  protons/pulse,  $r_{r.m.s.} = 1$  mm

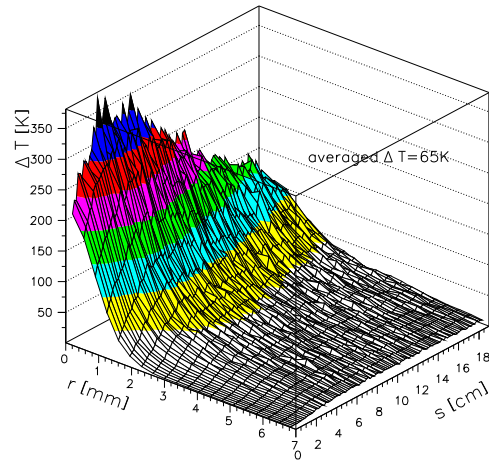


**Figure 3.21:** temperature profile for the jet, 24 GeV,  $4 \cdot 10^{12}$  protons/pulse,  $r_{r.m.s.} = 1$  mm

### 3.3.4 Diagnostics

Experiments performed at BNL and at CERN used the same method to monitor the shadow of the mercury splashes. Two independent optical camera systems were used: 1) an Olympus Industrial,

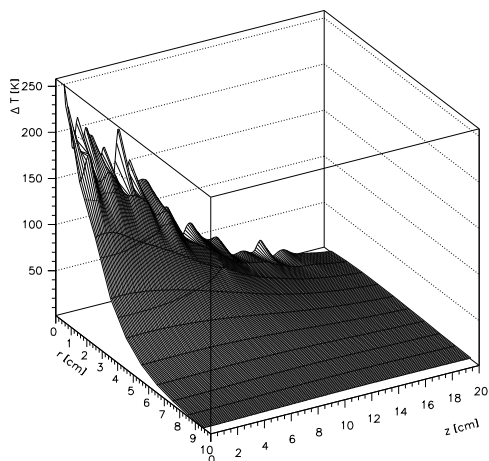


**Figure 3.22:** Temperature profile of a mercury target and a 1.4 GeV proton beam,  $30 \cdot 10^{12}$  protons/pulse,  $r_{r.m.s.} = 2.2$  mm

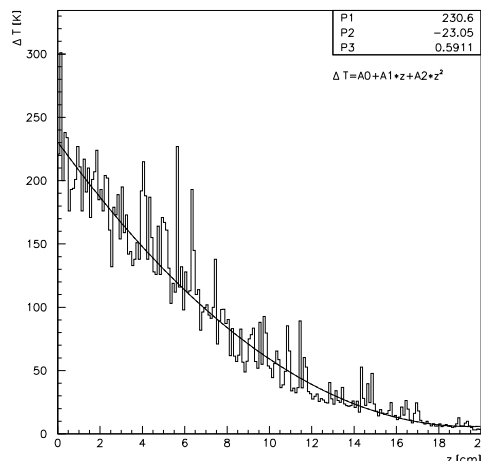


**Figure 3.23:** temperature profile on axis for a mercury target and a 1.4 GeV proton beam,  $30 \cdot 10^{12}$  protons/pulse,  $r_{r.m.s.} = 2.2$  mm

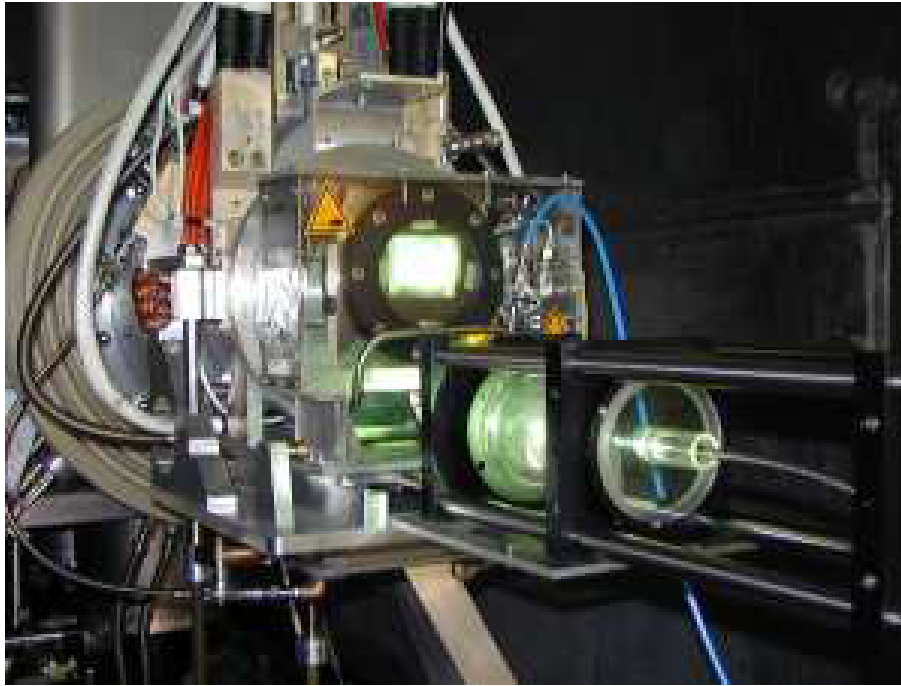
Encore PCI 8000S camera system capable of recording at a maximum rate of 8 kHz with shutter settings for each frame set to  $25 \mu\text{s}$ ; and 2) an SMD 64K1M camera capable of taking 16 frames at speeds of up to 1 MHz. The exposure time for the latter camera is 150 ns per frame. The jet and trough experiments at BNL have been recorded with both camera systems, the ones at CERN only with the Olympus system.

Figure 3.13 shows the installation in the ISOLDE target area. The read-out is done by a high-speed camera, which is placed as far as possible from the front end, where the target is placed. The camera position is behind a few meters of concrete in order to shield it from radiation. The light is transported towards the camera by a mirror placed in the light path.

Figure 3.24 shows the light source and the trough installed on the GPS front end of ISOLDE. The outer confinement containing the target steel frame is placed on a standard ISOLDE target base, which has been modified, in order to support the target box and two mirrors. A conventional 150 W light source is connected through a liquid light guide to the optical system next to the target box. The parallel light, which is needed to transport the image over a distance of  $\approx 15$  m towards the camera, is formed by an optical lens ( $f = 19$  cm), then reflected by two plane mirrors through the target box above the mercury level. In Fig. 3.25 we see three frames of the thimble event taken with the SMD 16K1M camera.

The view of the Olympus camera system on the jet setup as shown in Figure 3.26, which covered a round area with a diameter of  $d \approx 8$  cm, was centred at the zenith of the jet. The calibration grid can be weakly seen in Figure 3.26b. The 'digital image processing', described in the following section, makes it possible to clearly identify the grid.





**Figure 3.24:** Liquid Target Setup on the ISOLDE front-end. In front of the liquid the light source (liquid light guide) is installed, which points through a lens ( $f=19$  cm) onto two mirrors, which again direct the light through the steel window towards the camera, which is placed some 15 m away.

### 3.3.5 Digital Image Processing

The movies recorded with the Olympus system of the mercury splashes consist each of 8192 frames, which corresponds to a total recording time of 2.05 s. As the record rate is constant, the frame number is similar to a time stamp ( $\#_{frame} * c = t_{frame}$ ). From the sequence of pictures (frames) the data is extracted as an  $100 \times 98$  array of numbers, which correspond to the grey level for a single pixel in the frame. Per definition we call the direction along the vertical centre line of the thimble the y-axis, with the origin at the top of the mercury volume.

The instability of the grey level without having a proton impact or flying mercury (instability of the background illumination) results in an error of the position of about 0.15 pixel, which is four times below the spatial resolution given by the pixel size and therefore negligible. The

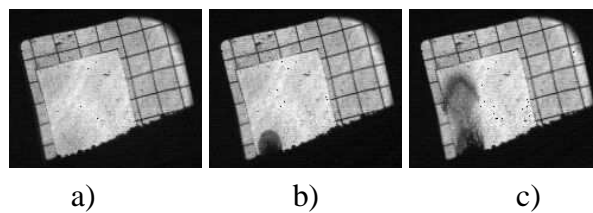


**Figure 3.25:** Hg interaction with 24 GeV,  $4 \times 10^{12}$  protons;  $t =$  a)  $0 \mu\text{s}$ ; b)  $300 \mu\text{s}$ ; c)  $800 \mu\text{s}$ . The grid is 1 cm x 1 cm

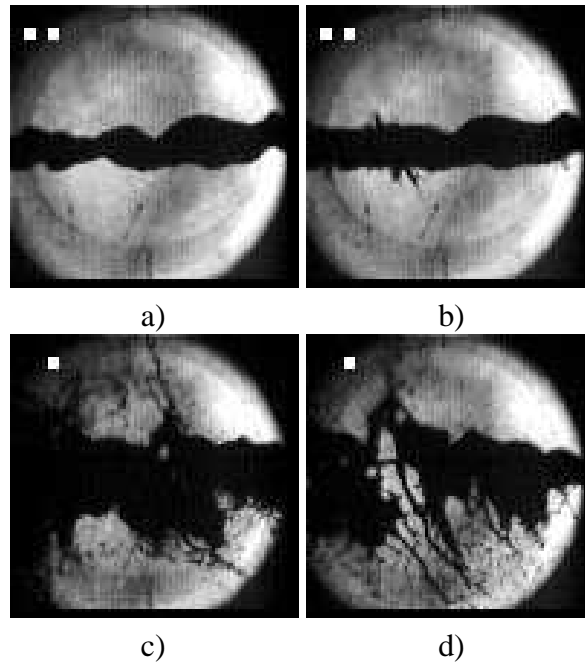


**Figure 3.26:** Hg jet interaction with 24 GeV  $3.8 \times 10^{12}$  protons;  $t =$  a) 0 ms; b) 0.75 ms; c) 10 ms; d) 18 ms

fluctuation of the background is periodically with a frequency of 100 Hz. This is likely due to the instability of the power supply of the light source.

Mercury is decelerated due to three different forces: friction in air, gravity and surface tension. The order of magnitude of these three forces are estimated, assuming an initial velocity of 10 m/s, a path of  $5 \cdot 10^{-2} \text{ cm} \equiv 5 \text{ ms}$ , mercury drops of  $d = 1 \text{ mm}$  and a surface increase of  $10 \text{ cm}^2$ . The volume of the mercury is approx.  $V = 1.5 \text{ cm}^3$ , with a mass of  $m = 20 \text{ g}$ . The gravity  $g = -9.81 \text{ m/s}^2$  causes a velocity decrease  $\Delta v \approx 5 \cdot 10^{-2} \text{ m/s}$ . The friction in air is defined as  $F = -bv$ , where  $b = 6\pi\eta r$  is the geometric friction coefficient for a sphere of radius  $r$  and is expected to be dominant for small  $t$ . The acceleration  $a \approx -5000 \text{ m/s}^2$  is orders of magnitude above the one of gravity. Assuming a surface tension as given in Table A.1 a velocity drop of  $\approx 0.3 \text{ m/s}$  occurs, which is only a small fraction of the initial velocity. Only the deceleration by air friction is not negligible.

The differential equation of motion of all brake forces is given by

$$dv/dt = -\frac{6\pi\eta r v}{V \rho} + g + \frac{F_{\text{surface tension}}}{m}, \quad (3.2)$$

with the solution:

$$v(t) = v_0 + g * t + e^{c+k*t}. \quad (3.3)$$

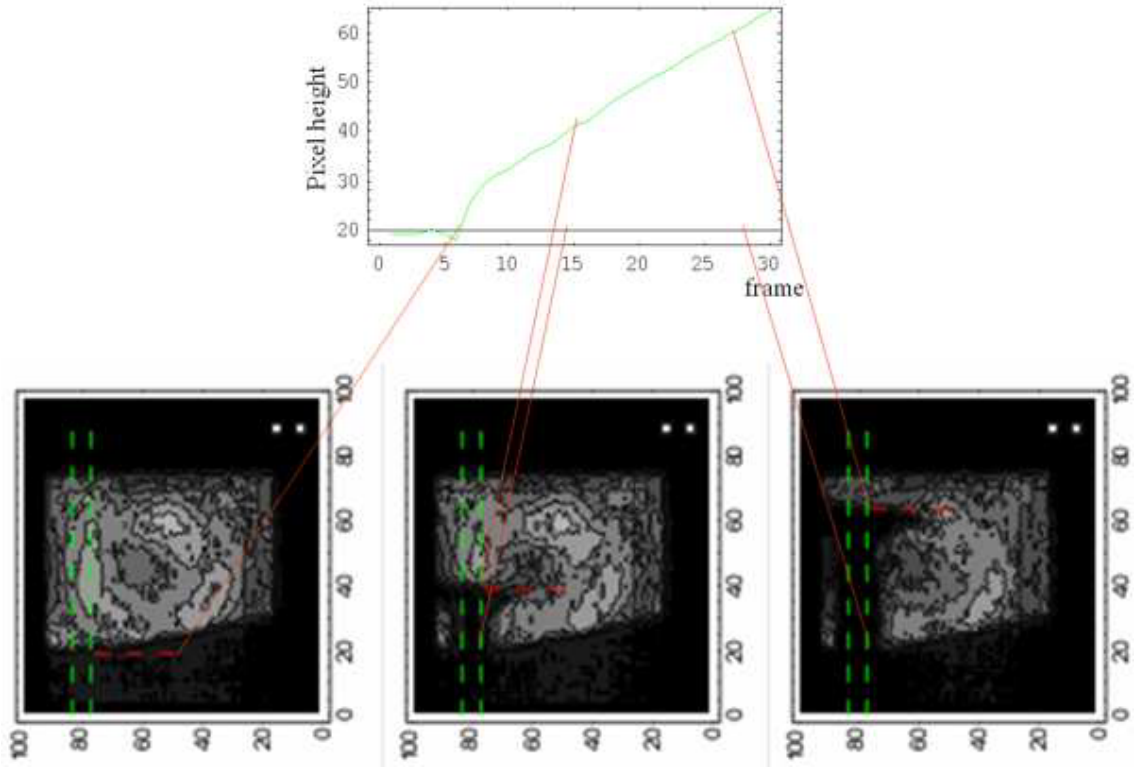


**Figure 3.27:** The mercury level raising out of the thimble.

$$x(t) = x_0 + v_0 * t - \frac{a}{2} * t^2 - p_1 * e^{p_2 * t}, \quad (3.4)$$

where  $p_i$  are free parameters linked with the friction of droplets in air. Using equation 3.4 the height of the mercury as a function of time was fitted (Figure 3.27) with the standard gravitational acceleration  $a = 9.81 \text{ m/s}^2$ .

The radius of droplets slowed down by air friction can be calculated as

$$r(t) = \sqrt{-6\eta v \frac{4}{3} \frac{1}{\rho a}}. \quad (3.5)$$

The droplet radii are measured to be on average  $d = 0.83 \text{ mm} \pm 0.14 \text{ mm}$ . This number is reasonable as the average thickness of the raising mercury column is  $d = 2.2 \text{ mm}$  assuming a plane and  $d = 0.9 \text{ mm}$  for a hollow cylinder.

Equation 3.4 is fitted to the data shown in Figure 3.27. The resulting function is shown in Figure 3.28. The velocity at time zero is calculated for each event and serves as the characteristic property, which is used to generalise the behaviour of a free surface liquid target at impact of a proton beam. The procedure of extracting the relevant information is similar in the cases of trough and jet, where the analysis is split in strips of a few millimetres along the z-axis. This information is presented in Figure 3.32 (see Section 3.4.2). The errors of the shutter time ( $t = 12.5 \mu\text{s}$ ) and the spatial resolution of the camera ( $0.89 \text{ mm/pixel}$  in the case of the jet,  $0.77 \text{ mm/pixel}$  for the

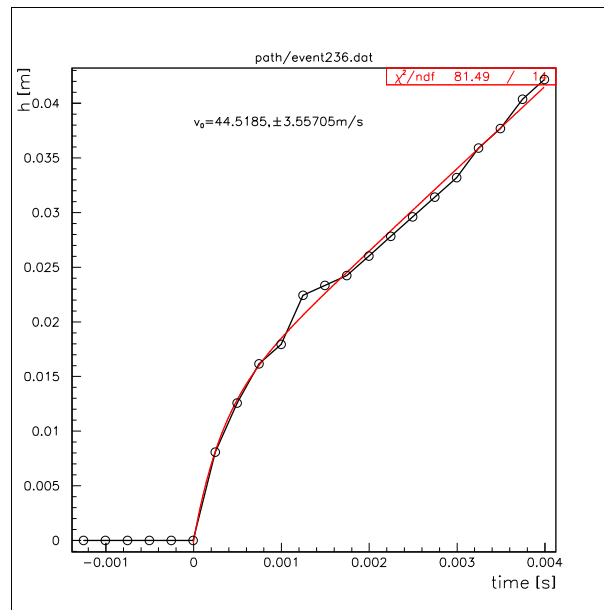


**Figure 3.28:** The black line indicates the raw data. The red line shows the final fit with equation (3.4).

trough) result according to Gaussian error propagation in an uncertainty of the initial velocity of  $\approx 10\%$ .

We define the 'splash' as the cloud of mercury, which is displaced from the initial volume by thermal heating. The splash is considered to be a cloud of mercury droplets mixed with the surrounding atmosphere. The 'splash velocity' is describing the movement of the fastest droplets, the front of the splash. The peculiarities of the splash in the three target samples is discussed in the Section 3.4.1- 3.4.2. The generalised behaviour of a mercury target as a function of the beam parameters is described in Section 3.4.4- 3.4.8

### 3.4 The Behaviour of Thimble, Trough and Jet on Impact of a Proton Pulse

Experiments concerning proton induced shocks have been performed in the E951 experiment at BNL [44] [33]. Similar tests in ISOLDE at CERN followed to study the target behaviour as a function of various beam parameters such as pulse intensity, spot size and time structure. Three different target configurations were used and their peculiarities are discussed first (Section 3.4.1-3.4.3). The comparison and the final conclusion on the scaling laws of the splash as a function of the various beam parameters are summarised in section 3.4.4- 3.4.8. We derive scaling laws which allow the extrapolation to final scenarios of a neutrino factory (Section 3.5).

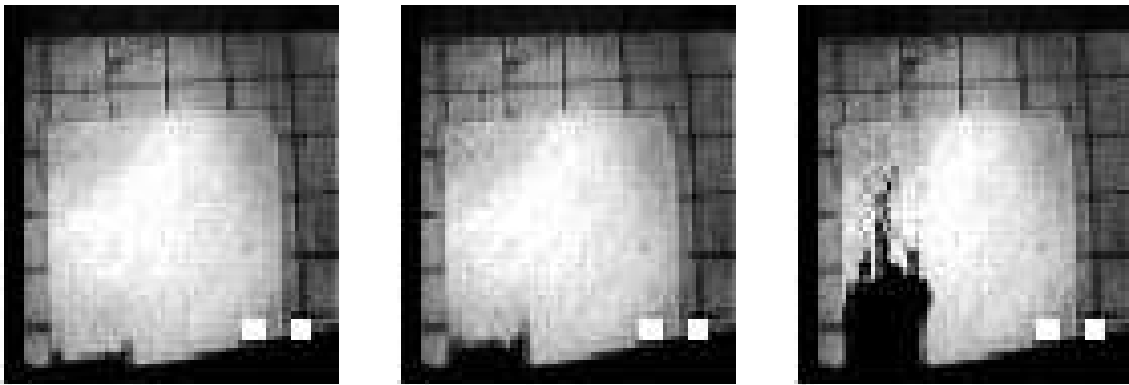


**Figure 3.29:** mercury splash at  $t = 0.88, 0.125, 0.7$  ms after proton impact of  $0.6 \cdot 10^{12}$  protons (thimble)

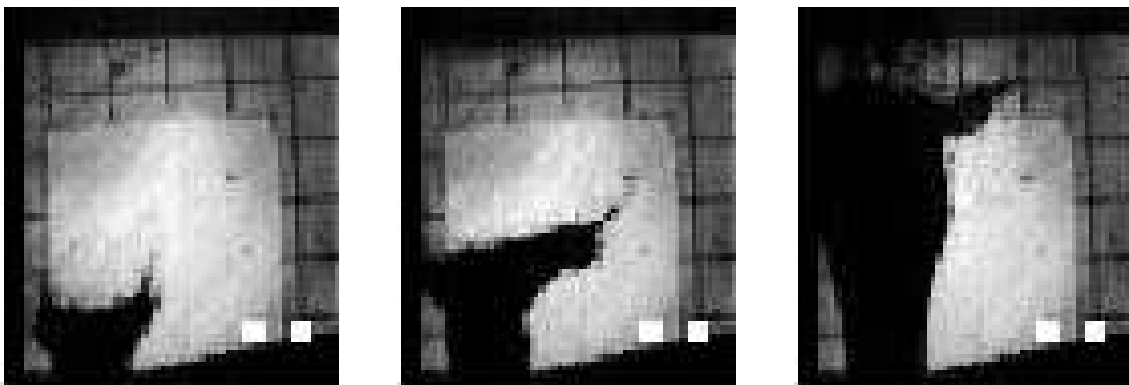


**Figure 3.30:** mercury splash at  $t = 0.88, 0.125, 0.7$  ms after proton impact of  $3.7 \cdot 10^{12}$  protons (thimble)

#### 3.4.1 The Thimble Splash

Figures 3.29-3.30 show the mercury splash at two different pulse intensities. The shadow photography used and the small transverse horizontal dimensions of the thimble/trough setup impose some restrictions on the information one can extract. The x-dimension, in which the light passes

trough the experimental chamber produces a projection of the splash. The expelled mercury could possibly touch the confinement. However, imagining that the centre of the raising column is not affected by any contact to the confinement, one can state, that the maximum velocities obtained are not reduced by the friction on the walls and indicate indeed the ones of a free surface target. As the free surface of the mercury in the thimble volume is restricted to a well defined area on the top of it, the mercury can only expand in vertical up-direction. The dimension in beam direction of the opening is 12 mm, where the mercury can splash vertically along 50 mm. The projection of the splash looks like a 'column' (Figure 3.29).

As mentioned, the third dimension can not be resolved with the diagnostics used. Still, there is a single hint on the 3-D structure of the mercury column of the trough splashes. The projected area of the mercury at fully evolved column is a section of  $\approx 1 \text{ cm} \times 7 \text{ cm}$ . The total mercury volume contained in the thimble is  $1.3 \text{ cm}^3$  and distributing it over this area gives an average thickness of 1.9 mm. If we assume a cylindrical shape of the raising mercury, the hollow column has a thickness of 0.9 mm. Such a form of the explosion has been predicted by [51] using the simulation tool HEIGHTS package [53].

### 3.4.2 The Trough Splash

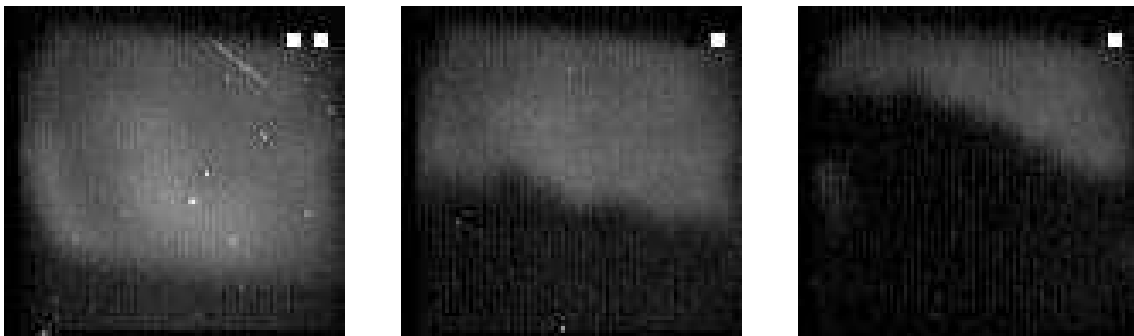


**Figure 3.31:** Trough splash at  $t = 0$ ,  $t = 2.5 \text{ ms}$  and  $t = 5.5 \text{ ms}$  after the 1.4 GeV proton beam pulse (intensity  $10^{13}$  protons) arrives from the left.

The setup of the trough 'suffers' from the same peculiarity of the layout as the thimble, but again the same argument is valid. A typical view on the trough splash can be seen in Figure 3.31. The extended mercury length in beam direction allows to observe the mercury splashes along  $z$ -direction. The maximum velocities for the trough were extracted from the region  $z = 1$  to  $z = 3$  cm after the beam entrance window, where the splash velocity is almost constant. For the trough, Figure 3.32 shows the propagation of the mercury splash along the beam axis at certain times after the proton impact, where the beam intensity was  $I = 20 \times 10^{12}$  protons/pulse. All recorded trough events show similar qualitative behaviour as the thimble. The splash velocity at a distance of  $z = 60 \text{ mm}$  after the beam window is about half the maximum splash velocity, which occurs close to the beam entrance. This shape corresponds to the distribution of energy deposition in numerical simulations. Also indicated is the initial splash velocity, which shows the same shape as the propagation of the mercury front.

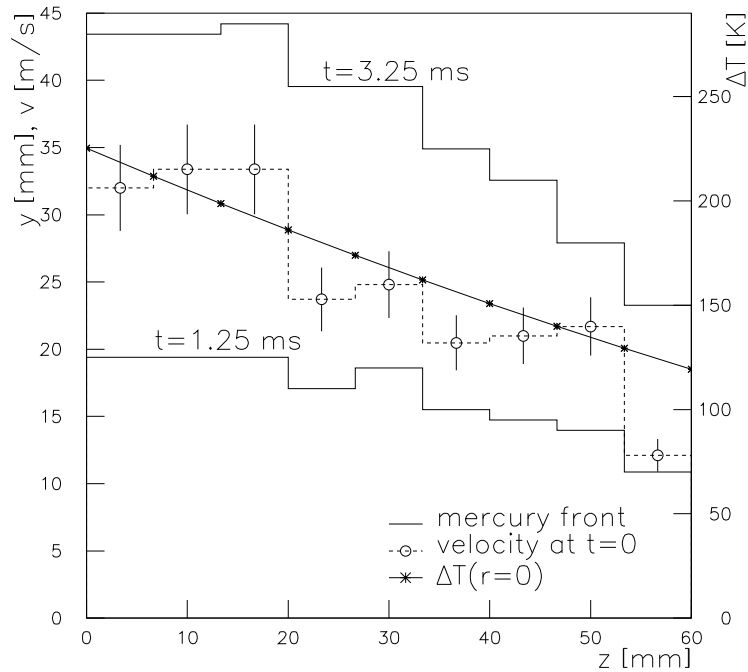


**Figure 3.32:** The trough explosion. The length of the mercury trough is  $l = 60$  mm along the beam axis. The proton beam is passing in positive  $z$ -direction. Indicated are the mercury front at two different times, the splash velocity of the trough and the simulated temperature profile as a function of the  $z$ -axis. The analysis is averaged over slices each  $\approx 7$  mm long.

### 3.4.3 The Jet Splash

The initial diameter of the jet at the interaction point fluctuated between 0.7 and 1.7 cm (Figure 3.34). The average initial velocity of the jet was 2.5 m/s (Figure 3.35).

Certain parameters can only be measured in the case of the jet, due to the different geometry. This concerns the disruption length and the drop splashes onto the viewing window. Latter item exits of course also in the case of the thimble and the trough, but can not be distinguished from the undisturbed raising mercury column as it is immediately blocking the light path. The total absence of any confinement is simulated only in the case of such a jet. The free surface in the case of the thimble and the trough are reduced to the opening at the top. The relation between splashes in the trough and the jet is known as the targets were exposed to the same circumstances (Figure 3.38). The obtained relation allows to use the results of the thimble and the trough to predict the mercury splashes in a jet target.

The main parameter of the beam is the 24 GeV proton intensity, which was varied from 1 – 4 TP (1 TP =  $10^{12}$  protons). The effects of the parameters 'beam spot size' and 'bunch length' can not be determined due to low statistics. The spot size was measured with an aluminium foil ( $r_{r.m.s.} = 1.5$  mm x 1 mm, horizontal/vertical).

Dispersal of the mercury by energy deposition due to the interacting proton beam was observed

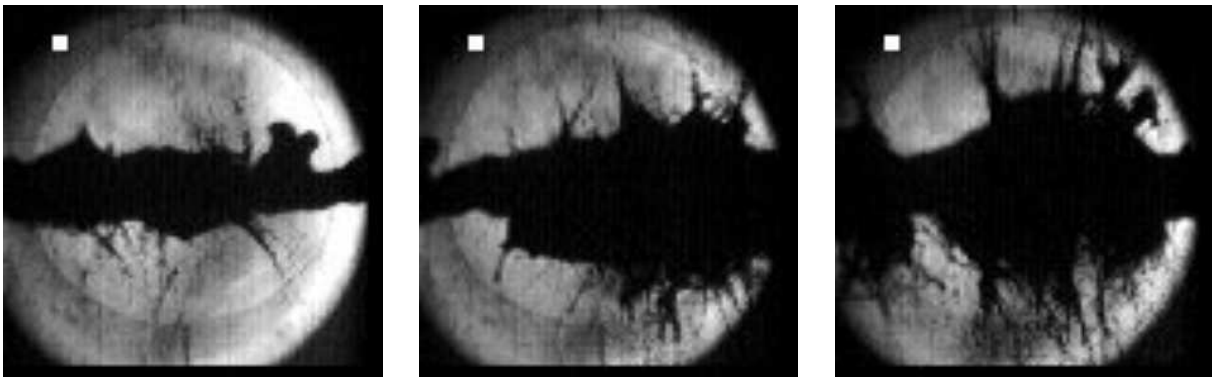


**Figure 3.33:** mercury jet at  $t = 6.5$  ms after proton impact of  $2, 3$  and  $3.8 \cdot 10^{12}$  protons

directly by viewing prominences as they left the bulk of the mercury jet. We were also able to indirectly measure the velocity of Hg droplets, since their arrival at the quartz viewing ports was signaled by distinctive splashes.

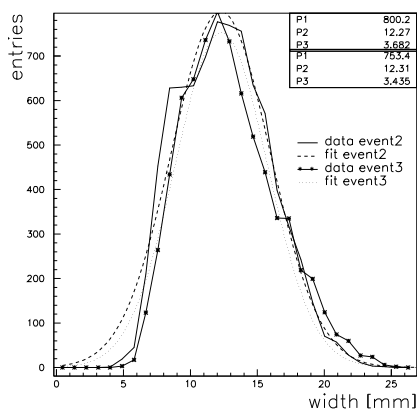


**Figure 3.34:** width of the mercury jet

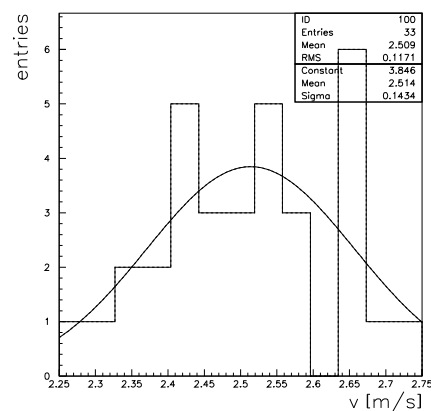


**Figure 3.35:**  $v_0$  of the jet

### Drop Splash onto the Viewing Windows

At a distance of 18 cm along the viewing axis in front and behind the jet are the viewing windows, which allow the camera to look inside the experimental chamber. As the proton beam impacts on the mercury jet and causes it to explode, several drops arrive after at a certain time at the windows and can - as long as no other mercury is blocking the view - be seen as splashes by the camera. The time of arrival for drops on the window correspond to the directly measured velocities of the mercury drops presented in Section 3.4.4.

### Disruption Length

The disruption length and its offset relatively to the zenith are only measurable in the jet setup, as there is no equivalent in the case of the thimble and trough. The thimble and the trough do not



extend outside the geometrical intersection of beam and mercury target. Also of interest is the extent of the disruption of the mercury, and in particular whether this disruption extends forwards and backwards from the interaction region. It was observed that the region of disruption was confined largely to the volume of overlap with the proton beam with no evidence of jet dispersal propagating back to the nozzle. The maximum disruption length observed was 14 cm.

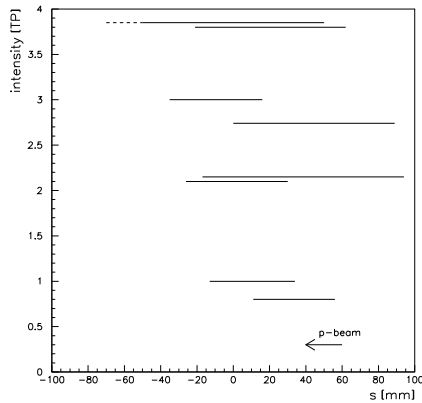


**Figure 3.36:** Disruption length and its position along the jet for different proton intensities. The dashed line indicates the invisible disruption for the event at 3.8 TP, where the disruption is extended to outside the viewing area. Proton beam and mercury-jet ( $v=2.5$  m/s) arrive from the positive ordinate.

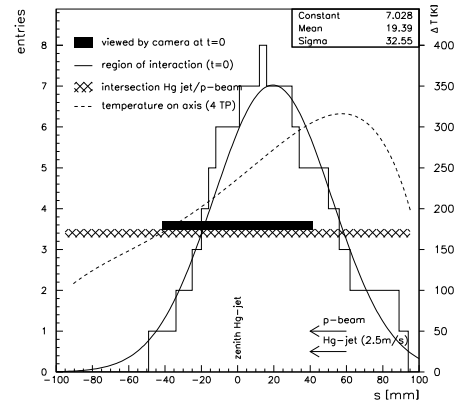


**Figure 3.37:** Probability of jet rupture and its Gaussian fit. The two bars indicate the the viewing length of the jet (black) and the physical intersection region of jet and beam (grey). For an 4 TP-proton impact the temperature rise on axis along the jet is shown (dashed).

Directly measured bulk velocities range from 5 to 50 m/s while the velocities of the Hg droplets arriving at the quartz window varied from 1 to 10 m/s. In both cases we observe that the maximum velocities increase roughly proportionally to the intensity of the impinging proton beam.

An interesting criterion to decide between a pulsed or continuous jet as a target is the length for which the jet is disrupted. As the jet passes the viewing area of the camera, the extension of the destructive interaction between the p-beam and the mercury jet can be determined by computing the origin of the Hg-drops. From this it can be learned whether a destructive pressure wave is travelling along the mercury jet outside the initial geometrical intersection region. As no obvious rupture outside the jet-beam intersection occurs, one can assume that travelling pressure waves do not harm the jet outside of this region. The numerical information of the disruption length is given in Table 3.3. Figure 3.36 is a scattered plot of the disruption length and position as a function of the distance along the jet and the proton intensity. Figure 3.37 shows a projection of Figure 3.36 on the position axis, where the ordinate shows the number of entries, which is proportional to the probability of rupture of the jet. We observed no rupture outside the geometrical intersection region.

# event	004	005	006	007	008	009	010	011
$\lambda_i$ [ cm ]	8.3	10+	4.5	4.7	5.6	11.1	5.1	8.9
offset [ cm ]	-2.1	-5+	1.1	-1.3	-2.6	-1.7	-3.5	0.0

**Table 3.3:** Parameters of the disruption length. In event005 the disruption length most obviously extended the visible area.

### 3.4.4 Pulse Intensity

For the thimble and jet experiments performed at BNL, the statistics are very low. In total 12 proton pulse impacts on jet and target have been performed. Main parameter of the beam is the proton intensity, which was varied from 1 – 4 TP. The number of events is high enough to reveal the information of the difference in explosion in the case of the thimble and the jet. Detailed information on the splash velocity as a function of the pulse intensity are extracted from the experiment performed at ISOLDE.

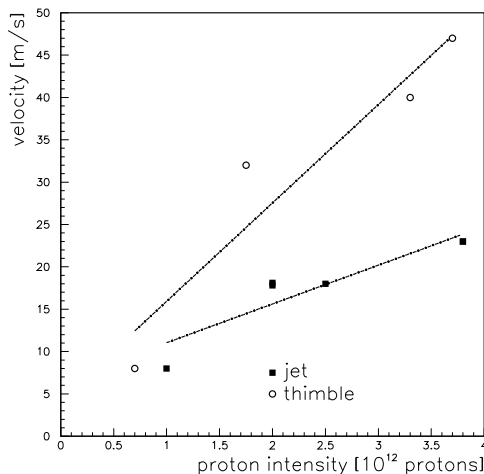


**Figure 3.38:** Splash velocity of thimble and jet in the AGS beam. The splash velocity in the case of the jet is about two times less than for the thimble.

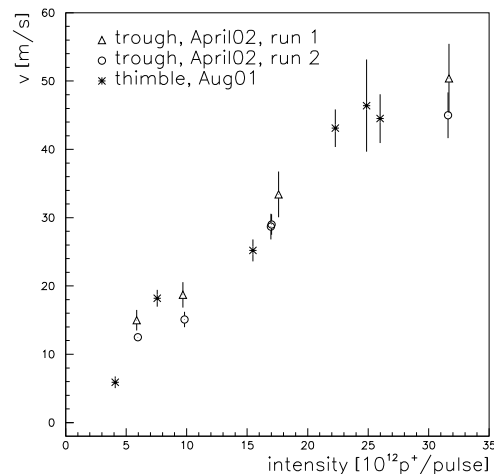


**Figure 3.39:** The splash velocity scales linearly with the proton intensity. Indicated are measurements from the thimble and the trough, where the same maximum splash velocities are observed. Run 1 and 2 are similar exposures of the trough to the proton beam at different times of the experiment.

The splash velocities measured from the thimble and jet in a 24 GeV proton beam are plotted in Figure 3.38. The data points represent drop sizes greater than 1 mm. A small fraction of the jet is dispersed into small, fast droplets. The upper limit of the dominating velocity is indicated by the solid line. The splash velocity in the thimble is about two times higher due to the lower free surface. The explosion in case of the jet can expand almost spherically, whereas in the case of

the thimble only the top is opened to the atmosphere.

The maximum splash velocity is plotted in Figure 3.39 as a function of the proton pulse intensity. The figure is not corrected for the spot size. The quadrupole settings for beam focusing were kept constant during this measurement series, corresponding to a spot size of  $r_{r.m.s.} = 2.1$  mm at maximum intensity. The splash velocity scales linearly with the beam intensity. The experiments on trough and thimble show the very equivalent behaviour for these velocities. The splash velocities shown here are derived from the experiments with the thimble and the trough and are not directly valid for the behaviour of a free surface jet. The splash velocities for the free jet are about a factor two below those observed with thimble and trough [44]. This has to be taken into account when estimating the impact of a proton beam on a jet target as foreseen for a neutrino factory.

### 3.4.5 The Spot Size

Figure 3.40 shows the behaviour of the mercury target as a function of the spot size of the proton beam. All events with a spot size different from  $r_{r.m.s.} = 0.5$  mm are due to a pulse with two bunches within  $t_{pulse} = 0.5 \mu s$  and a total intensity of  $I = 17 \cdot 10^{12}$  proton/pulse recorded at ISOLDE. The splash velocity for a spot size  $r_{r.m.s.} = 0.5$  mm (pulse length 150 ns) is derived from the events recorded at BNL [33]. There, the beam intensity was  $I = 3.8 \cdot 10^{12}$  protons/pulse and the splash velocity was extrapolated to an intensity of  $I = 17 \cdot 10^{12}$  protons/pulse according to the scaling law shown in Figure 3.39. The splash velocity is corrected for the energy loss of protons  $dE/dx$  (according to Bethe-Bloch) slightly differing at 1.4 GeV and 24 GeV. The splash velocity depends on the spot size  $r_{r.m.s.}$  like  $(1/r_{r.m.s.})^2$ .

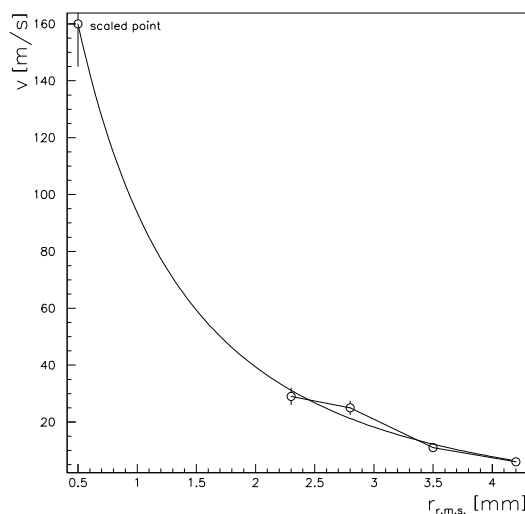


**Figure 3.40:** Increasing the spot size of the proton beam results in a decrease of the splash velocities. The intensity was  $I = 17 \cdot 10^{12}$  protons/pulse.

### 3.4.6 Pulse Length

The PS Booster allows to extract up to four bunches from its four rings at adjustable bunch-to-bunch distance, which is variable from a minimum of  $t_s = 286$  ns to several microseconds in multiples of  $t_s$ . To simulate various bunch lengths at fixed intensity and spot size, two bunches with varying spacing were extracted from the PS Booster. Each of the two bunches contained  $5.5 \cdot 10^{12}$  protons. The behaviour of the mercury target as a function of the pulse length for two different spot sizes is indicated in Figure 3.41. The indication 'bunch distance' instead of pulse length would be more precise, as it describes the peak-to-peak delay of the two bunches used for this experiment.

Figure 3.41 shows the splash velocity as a function of the pulse length. The measured velocities are normalised to the velocity resulting from adjacent bunches at minimum pulse length. At a bunch spacing of about  $t_s \approx 3 \mu\text{s}$  the splash velocity drops. The splash velocity for larger pulse lengths correspond to the ones, where the target is submitted to a single bunch with an intensity of  $5.5 \cdot 10^{12}$  protons only.

During this time  $t_s$  the pressure wave induced by the first bunch travels about 5 mm, which corresponds to about twice the spot size  $\sigma$ , and the pressure waves of the two bunches do not sum up, but travel sequentially. Such a reduction of the instantaneously induced pressure, where the dynamic response is shorter in time than the pulse length, is also envisaged in the concept for the granular target (Section 2.3).

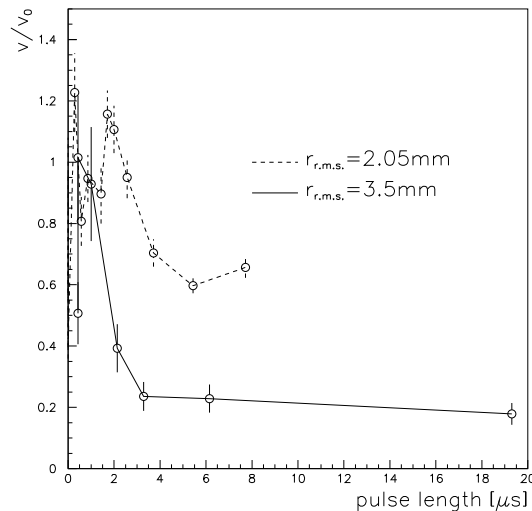


**Figure 3.41:** Splash velocity vs. pulse length for two beam spot sizes. The pulse length was varied from a minimum distance between two bunches of  $0.286 \mu\text{s}$  up to  $8 \mu\text{s}$  and  $19 \mu\text{s}$  respectively. The velocities are normalised to a typical figure for each of the two data series.

### 3.4.7 Cavitation

As discussed in the previous section the splash velocity is reduced, if the pulse length is extended for more than  $3 \mu\text{s}$ . Possible cavitation bubbles could occur within this time and reduce the local interaction of the proton beam with the target. This would result in the observed effect of reduced splash velocity, and at the same time lower the integrated pion production. With the following argumentation we exclude this show-stopper for a jet target.

By utilising the SMD 64K1M camera set in a fast frame mode (1 frame/10  $\mu\text{s}$ ), we observed that the breakup of the mercury jet commenced after an elapsed time of  $\sim 40 \mu\text{s}$ . Observations with the camera with a recording rate of 1 MHz showed no discernible disruptive motion in the jet within a time interval of 18  $\mu\text{s}$  [33]. As the mercury volume is not expanding within the pulse length, the averaged density can not change and so the intergrated interaction of a single pulse keeps the same. Also the position of the maximum of the pion production does not shift, if we assume that the cavitation bubbles are small compared to the target size and are equally distributed.

At the “*école polytechnique fédéral de Lausanne*” (EPFL), Laboratory for Hydraulic Machines (LMH), research on cavitation close to free surfaces is ongoing (see Section C). Laser induced cavitation in a transparent medium is observed optically and will provide a better understanding of the behaviour of cavitation bubbles in a liquid [52].

### 3.4.8 Beam Scan of the Target

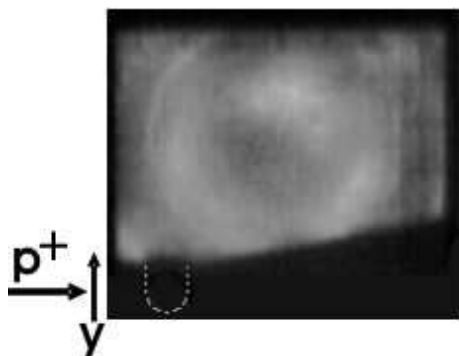


**Figure 3.42:** Beam scan of thimble. The beam was displaced in the vertical direction of the thimble.

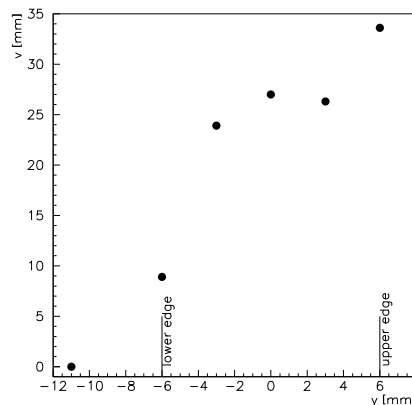


**Figure 3.43:** Vertical beam scan of the thimble. The lower and upper edge of the thimble are indicated. The pulse at  $y = -11 \text{ mm}$  traverses the steel frame below the mercury target.

The beam positioning was verified by various methods. At BNL, a beam flag and optical analysis assured the beam position. In ISOLDE, the beam position was verified in advance with the installation of a SEM-grid in the target place. Additionally an aluminum-foil has been fixed on the mercury target confinement. The peak activation was determined afterwards and confirmed

the beam position. The variation of the beam height gives a hint on the beam and thimble relative position and shows also its effect of blocking mass on the acceleration of droplets.

Figure 3.42 illustrates the principle of this method. The minimum position was below the mercury thimble and the beam hit the steel frame only. Maximum height of the beam was such, that the beam centre was located at the free surface of the mercury. Figure 3.43 shows the velocity measurements as a function of the vertical beam position. The passage trough the steel frame only, at  $y = -11$  mm, shows no effect on the mercury. The energy deposition, the resulting thermal expansion, the higher heat capacity and the lower thermal expansion coefficient of steel make the non-effect obvious. The increase of the splash velocity for beam positioning at  $y > 5$  mm is according to higher induced pressure gradient and the lower mass, which needs to be accelerated.

In the case of the jet, thinner parts (0.6 – 0.7 cm) resulting of turbulences of the initial jet are disrupted quicker than thicker ones (1.5 cm).

### 3.5 Conclusion

In order to extrapolate the behaviour of a liquid metal target from the kilowatt to the megawatt-scale as required for a neutrino factory, various measurements were carried out with the aim of establishing scaling laws of the splash velocity as a function of beam size, intensity and time structure.

The mercury thimble and jet experiments confirmed reasonably well the predictions for the behaviour of a liquid metal target on impact of a proton pulse. The thimble provided a simple setup for studying proton-induced shocks. Explosion velocities of up to 45 m/s were measured using proton intensities of up to  $3 \cdot 10^{13}$  protons/pulse. The splash velocity is two times lower in the case of the jet, as its free surface is almost spherical (Section 3.4.4).

At low proton energies, a coaxially alignment of target and beam results in highest splash velocities at the beam entrance to the target, in agreement with the simulated deposited energy distribution (Section 3.4.2). As the path outside the space limits of the horn are shorter in reversed direction, one may ask, whether the mercury jet should be directed with or against the beam direction. This is only valid for the CERN scenario, as in the US scheme the maximum power deposition is shifted towards the downstream end by inclination of proton beam and target.

The rupture of the mercury jet outside the intersection of jet and beam did not occur (Section 3.4.3), which makes the use of pulsed target jets unnecessary. This goes along with the observations in the case of the through, where the velocity distribution followed the simulated energy deposition (Section 3.4.2). Mercury jet dispersal is mostly transversal and delayed for  $\sim 40 \mu\text{s}$ .

Changing the pulse length by increasing the peak-to-peak distance of the single bunches from minimum 286 ns resulted in a maximum pulse length of  $\approx 19 \mu\text{s}$ . At a pulse length of  $\approx 3 \mu\text{s}$  the explosion velocity drops to about half the initial value (Section 3.4.6). This is very likely due to the advanced propagation of the first pressure wave from the centre of the target to the outer boundary and the absence of positive interference of subsequently induced pressure waves.

The following scaling laws of the mercury splash as a function of beam parameters have been

derived:

- Intensity: The splash velocity scales linear with the proton pulse intensity. With the highest intensity available ( $32 \cdot 10^{12}$  protons/pulse) mercury splashes with a maximum velocity of 45 m/s have been observed (Section 3.4.4).
- Spot size: The splash velocity depends on the spot size  $r_{r.m.s.}$  like  $(1/r_{r.m.s.})^2$  (Section 3.4.5).
- Pulse length: With a pulse length comparable or longer than the time  $t_{response}$  the sound needs to travel through the target radially, the splash velocity is determined by the number of protons impinging on the target during this time interval  $t_{response}$  (Section 3.4.6).

These scaling laws of the splash velocity for a liquid mercury target enable extrapolation to a 4 MW proton beam as required for a  $\nu$ -Factory. Explosion velocities of up to 45 m/s were measured using proton intensities of up to  $3 \cdot 10^{13}$  proton/pulse. The proton intensity of the European neutrino factory scenario will be seven times larger than in the experiments at ISOLDE. The inner horn radius restricts the beam spot size to a radius  $r_{r.m.s.} = 4$  mm to keep  $5\sigma$  within the horn to avoid radiation damage. Numerical simulations assume the target radius to be  $3\sigma$  of the beam, where the maximum pion yield occurs. The beam spot size will be two times larger than in the experiment at Isolde. We measured for the jet a splash velocity two times smaller than in the case of the trough. The pulse length is shorter than the shock wave propagation to the target border, which results in no attenuation of the splash. The expected mercury splash velocity is about two times the initial jet speed out of the nozzle. The resulting explosion in  $4\pi$  makes the removal within the delay of two successive proton pulses difficult.

A splash velocity of the same order as the initial velocity is envisaged to obtain a splashing in forward direction. To achieve such a goal, the following considerations are possible:

The pulse length is fixed by the layout of the successive RF-acceleration. The spot size is fixed by the presently designed capturing device. The energy deposition is at the minimum. The use of a target material with higher heat capacity and a lower thermal expansion coefficient would reduce the splash velocity.

# Chapter 4

## A Metal Jet in a High Magnetic Field

The US scenario for a neutrino factory foresees a solenoidal channel for pion capture (section 2.2.1). The high power target scheme relies on a mercury jet injected with a velocity of  $\approx 30$  m/s under an angle of 6 degree into the 20 Tesla magnetic field. A moving metal in an inhomogeneous field experiences forces caused by the change of the magnetic flux and the induced eddy currents. The magnetic field again acts on these eddy currents and results in magneto-hydrodynamic effects.

The layout in the region of interaction between proton beam and mercury jet is indicated in Figure 4.1. The target region is surrounded by the solenoidal channel (black square, indicated as shielding), where the minimum bore is  $r = 7.5$  cm. The mercury jet is inclined by 100 mrad from the solenoid axis to maximise the pion yield. Table 4.1 summarises the geometrical parameters for the mercury jet and the proton beam [13]. A few meters downstream from the interaction region, the dispersed mercury is collected in a pool, which serves as the beam dump at the same time.

A mercury jet ( $v \leq 15$  m/s,  $d \approx 4$  mm) has been injected into a 20 T solenoid. The experimental conditions differ from the ones of the proposed neutrino factory and the purpose of these measurements is to benchmark the simulation tools for a full scale mercury jet target. In section 4.1 the experimental setup is described. This includes the solenoid configuration, the pump and the experimental chamber, where the jet is injected. Section 4.1.3 explains the diagnostics and the principle of measuring the properties of the jet. The results of the observation are presented in Section 4.2.

$\sigma_{proton\ beam}$	1.5 mm
$\alpha_{beam}$	-67 mrad
$\beta_{jet}$	-100 mrad
$radius_{jet}$	5 mm
$v_{jet}$	30 m/s
jet material	mercury

**Table 4.1:** Geometric parameters of the proton beam and the mercury jet



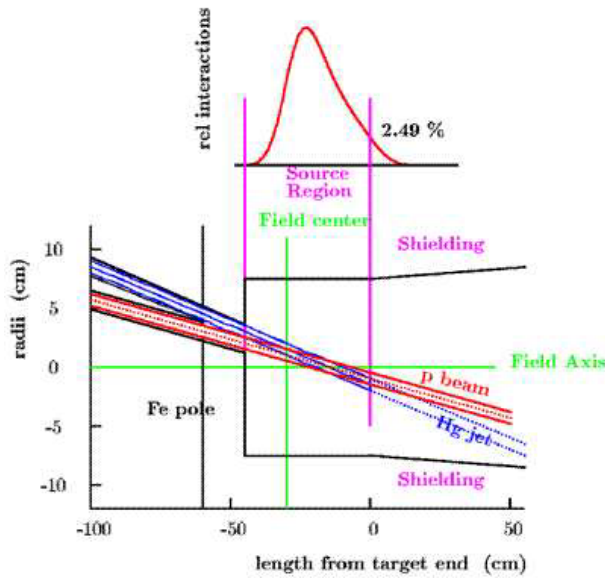


Figure 4.1: Layout of the US target scenario.

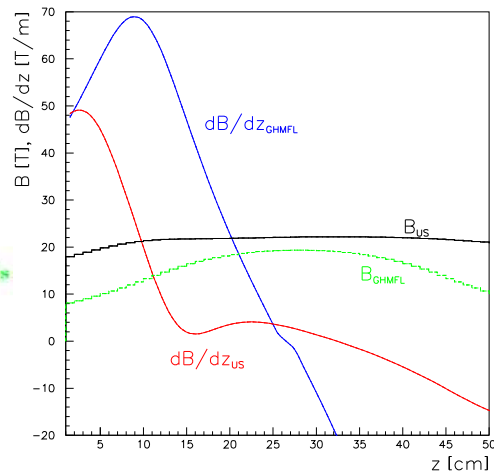


Figure 4.2: B-field of the M9 at Grenoble High Magnetic Field Laboratory (GHMFL) compared with the target section of the US-solenoid.

## 4.1 Experimental Layout

### 4.1.1 The 20 Tesla Solenoid M9

At the **Grenoble High Magnetic Field Laboratory (GHMFL)**, M9 is a solenoid with a vertical bore of  $d = 13\text{ cm}$  for the configuration, where the DC magnetic field can be ramped up to  $\approx 20\text{ Tesla}$ . Figure 4.2 shows the B-field of the solenoid M9 for magnetohydrodynamic studies at GHMFL and compares it with the one of the US decay channel. The maximum field is comparable, but its gradient is much higher in the case of M9. The bore can be accessed from the top. The bottom is closed at 44 cm below the maximum of the magnetic field, where the bore is reduced to  $d = 5.5\text{ cm}$  over the last 17 cm (Figure 4.3).

### 4.1.2 The Jet Setup

The mercury jet is driven via a compressed air driven double piston pump feeding a nozzle placed in the magnetic field. A picture of the setup installed at GHMFL is shown in Figure B.1, where on the left hand side the pump rack is located. The blue confinement hose points towards the top of the experimental chamber, which is inserted in the vertical solenoid.

A flow chart of the setup is indicated in Figure B.2. A two stroke piston pump, which is air driven with a translation of 1/16, accelerates the mercury. A detailed description of the pump NORDSON 25B, which is a commercial product for paint spray systems, can be found in [49]. It is neither designed for high flow rates nor to be used with mercury. The maximum air pressure of 6 bar, limited by a safety valve, results in a static pressure of 90 bar on the mercury. The

tungsten seats of the ceramic ball valves broke regularly after typically 150 strokes [54], what forced dismantling of the mercury circuit to access and repair the pump. A detailed description of the gas rack, the mercury recuperation system and the handling procedures are given in [55]. A piezo-electric pressure gauge (Dytran 2300V5 pressure gauge) is mounted at the beginning of the high-pressure piping to monitor the dynamic pressure losses of the moving mercury.

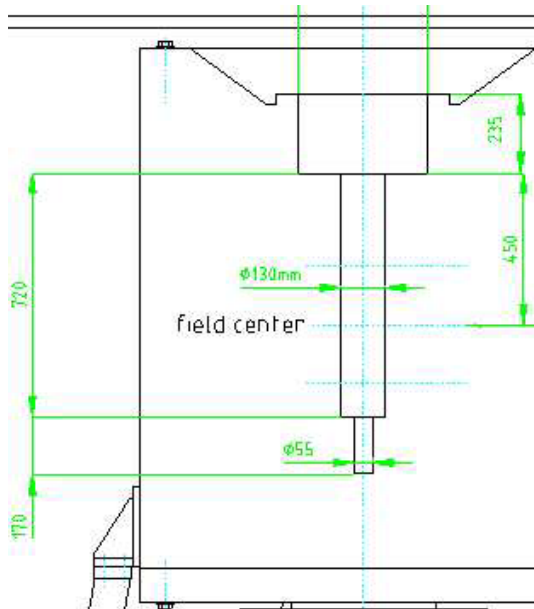


**Figure 4.3:** Technical drawing of the solenoid M9 at GHMFL

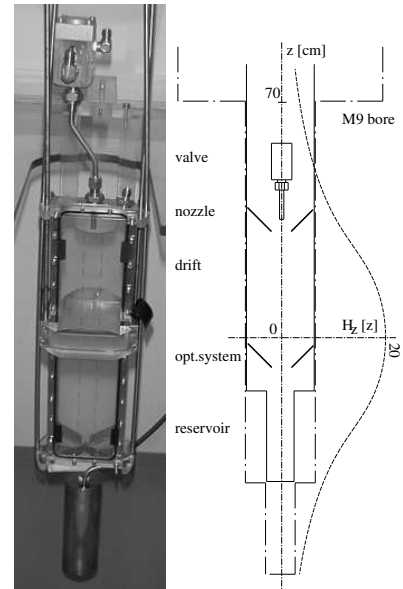


**Figure 4.4:** left: jet chamber; right: schematic in the bore of M9

Via the blue hose, containing gas and mercury supply, the pump rack is connected to the experimental chamber, which consists of an outer confinement containing the jet chamber (Figure 4.4). The shape of this outer steel tube is following the bore of the solenoid (see Section 4.1.1) and its cross-section is indicated in the following figures.

### The Jet Chamber

Due to the working principle of the pump and due to the restricted space inside the experimental chamber and its reservoir, the mercury jet is pulsed. Spilled mercury can not be withdrawn from the chamber permanently and would block the observation view. An air-actuated ball valve, located next to the nozzle, allows to run the jet for an adjustable delay, typically of 100 ms (Figure 4.4). On triggering the valve, a mercury jet is ejected from the nozzle ( $d_{inner} = 4$  mm) into the jet chamber, where it travels along a free path of  $\approx 27$  cm. The jet chamber consists of a steel frame with a Makrolon cover on each side. At the bottom of the jet chamber splash guards in v-form collect the mercury and guide it into the cylindrical reservoir located below. With argon pumping of a few atmospheres the mercury can be recuperated to the main reservoir in the pump rack. The jet chamber with its double confinement is fixed to an elevator in order to vary its height. The position of the nozzles are chosen such, that the drift of the jet is either placed in the

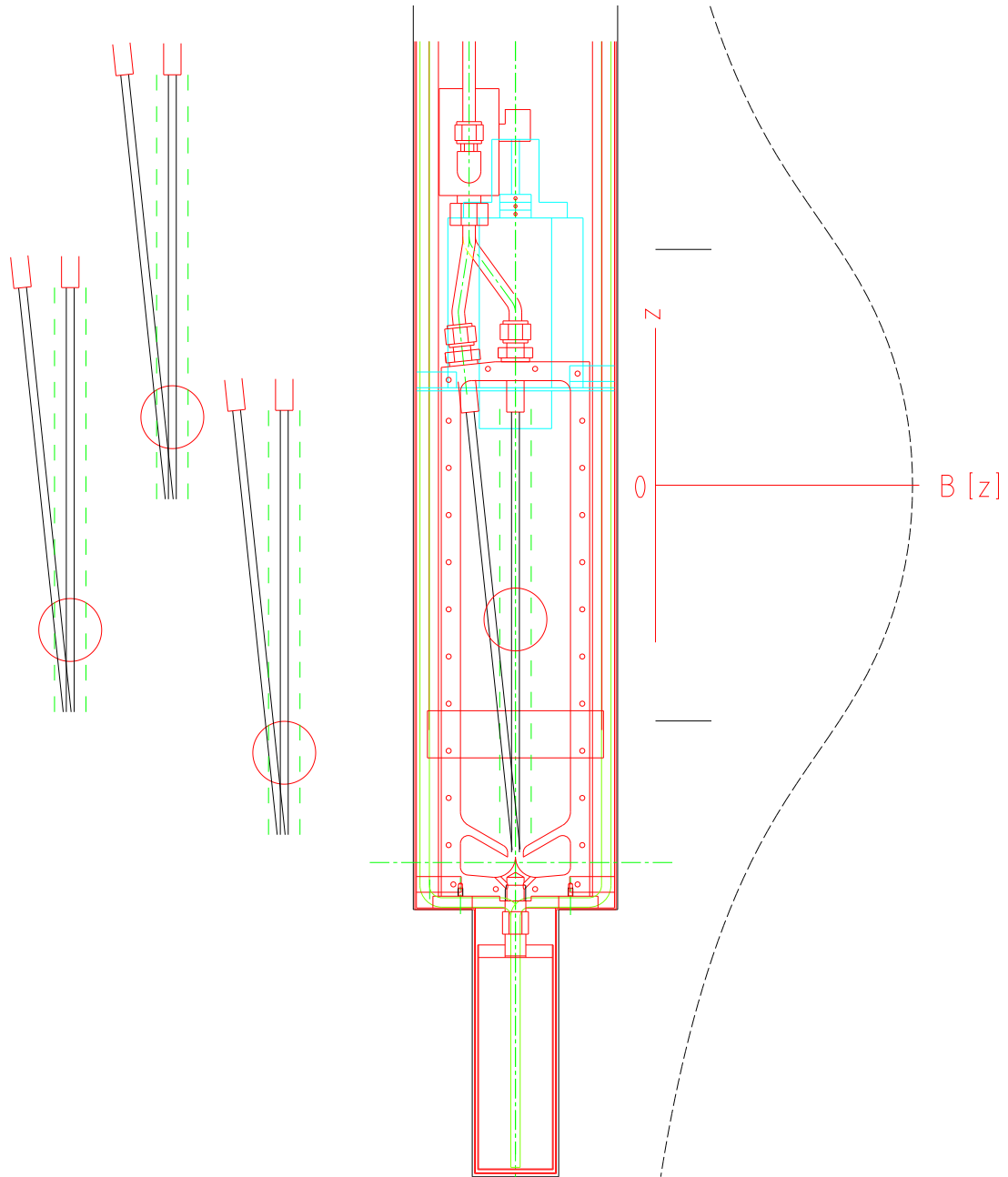


**Figure 4.5:** Short nozzles: collinear and tilted. Technical drawing of the jet chamber placed in the M9 bore with the nozzle at two different angles and at different positions indicated. The position 'lowest' is limited by the magnet bore, which is closed at the bottom.

positive or negative gradient, or in the maximum field (Figure 4.5). The chamber is filled with one atmosphere of argon normally, but an under-pressure can be applied. If not stated differently, the jet chamber was filled with one atmosphere argon.

## The Nozzles

The connection of the nozzle is modular in such a way that various nozzles with different lengths and angles can be mounted. The nozzles differ in the length, which is measured from the valve until the outlet, and in the inclination, at which they are installed. Nozzles installed at two different angles ( $0^\circ$  and  $6^\circ$ ) are indicated in Figure 4.5. The figures on the left side show the possibility to move the drift path in respect to the magnetic field, which is shown on the right side. The left figures show besides the nozzle and the jet also the calibration grid (green dashed line) and a typical view area (red circle). Such nozzles with a short length ( $\approx 13$  cm) are called “short”. The length of the nozzle is measured from the air-actuated valve to the tip of the nozzle. The left figures show only the tip of the nozzle, the full nozzle is indicated in the centred figure. Nozzles, where the tube length is extended to  $\approx 23$  cm, are called long nozzles, where the longer pipe implies a accordingly shorter drift path as the position of the valve is fixed in respect to the experimental chamber as indicated in Figure 4.6. The different length of the nozzles produces a mercury jet with different properties (Section 4.2.3- 4.2.4).

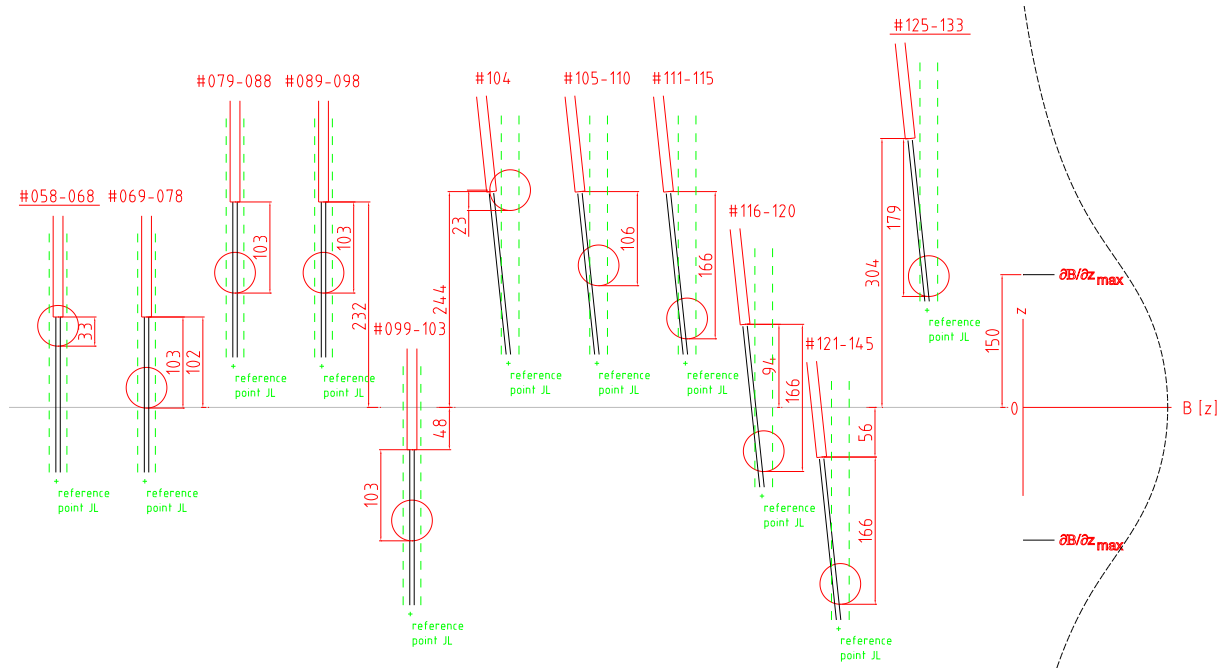


**Figure 4.6:** Positions of the long nozzles (straight/tilted) and the viewing area (circles) relatively to the solenoid for each set of data. The event indices are indicated.

### 4.1.3 Diagnostics and Digital Image Processing

As for the experiments on proton induced shocks, the MHD jet setup is based on the recording of the shadow of the mercury, intercepting a laser light source, with a high speed camera. Sets of mirrors allow the installation of the sensitive pieces of electronics outside of the magnetic field.

The light source is a laser diode, 35 mW, 670 nm, coupled to a few meter long fibre. The fibre guides the light into the confinement of the jet chamber. An optical lens focuses the light to a parallel beam with a diameter of  $\approx 45$  mm. The stainless steel chamber equipped with transparent windows sits between two mirrors placed at 90 degree. The light is guided parallel to the jet, reflected via a plane mirror (Figure 4.4) by  $90^\circ$  through the Makrolon window, intercepts with the drift path of the jet and is again reflected by  $90^\circ$  through the top of the confinement towards the high speed camera (Section 3.3.4). The optics allowed the observation of a  $\approx 4$  cm diameter surface movable along the field axis over a distance of 20 cm. The camera settings were 2000 frames/second for the recording rate and  $25 \mu\text{s}$  for the shutter time. A typical view in absence of the mercury jet is shown in Figure 4.7. In Figure B.3 and B.4 a full image of the mercury jet can be seen, where the outer confinement was removed to directly view the drift path.

The digital image processing is similar to the case of the proton induced shocks (Section 3.3.4). The calibration and the random tilt of the central axis are corrected using the calibration grid (two parallel lines with a distance of 2 cm, each dashed 1 cm equidistant). The tilt correction and the extraction of the resolution (typically 0.33 mm/pixel) is illustrated in Figure 4.7. The mercury jet was extracted by differential comparison with the initial frame. The raw jet, which is corrected for background, is indicated in Figure 4.8. The digital image processing allows to extract information like jet width, velocity and inclination, which is correlated with the offset. As the representative velocity for an event, the initial 50 ms of the fully established jet are averaged, except if clearly indicated velocity of the jet tip. The width and the inclination are averaged over  $\approx 50$  ms as well. The resolution of the camera and the typical length (3 cm) results a in a measurement error of approx.  $\pm 5\%$  of the velocity.

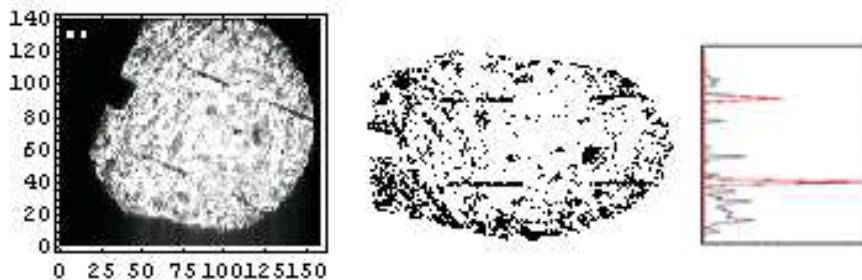


**Figure 4.7:** Extracting the calibration grid. From the original frame the black border is removed. A rotation and projection reveals the position of the calibration grid (two black, 1 cm-dashed lines at a distance of 2 cm). The resolution was typically 0.33 mm/pixel for the MHD experiment. In the left figure the tip of the nozzle is seen.

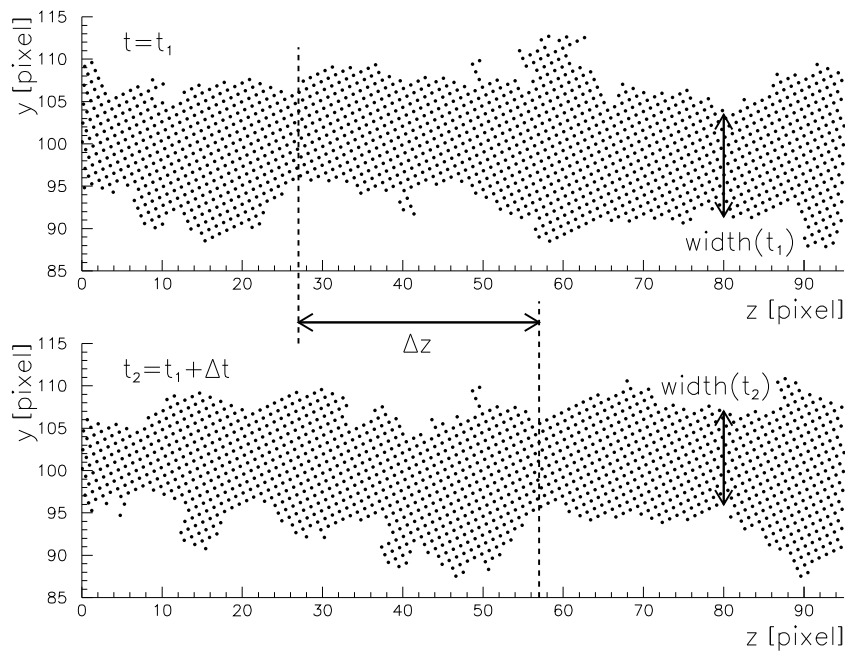


**Figure 4.8:** Width and velocity of a jet. From each frame the jet is extracted. The shape can be measured and reveals the width of the jet. The comparison of the jet shape from frame to frame reveals the shift per frame and the velocity  $v = \frac{\Delta z}{\Delta t}$  can be calculated.

## 4.2 Observations

From the nozzle the jet is ejected with a velocity in absence of a magnetic field depending on the driving pressure as discussed in Section 4.2.1. The stabilising effect of the magnetic field on a turbulent (Section 4.2.3) and a quasi-stable (Section 4.2.4) jet are observed by using different nozzle types. The impact of the presence of a magnetic field on deflection, width and velocity are discussed in Section 4.2.6-4.2.8. Finally we compare with analytical calculations and numerical simulations, and conclude on the impact of the design for a full scale mercury jet in a magnetic field as foreseen for a neutrino factory.

### 4.2.1 Jet Velocity at $B=0$ T

The optical observation of the shape and the resulting determination of the velocity are presented in Figure 4.8 and 4.9. From each frame the position of both jet edges is measured. The difference of these two provides the width of the jet. Independent superposition of these three arrays (upper edge, lower edge, width) of two subsequent frames and the evaluation of the minimum difference by shifting along the jet axis gives the velocity  $v = \text{shift} * \text{rate}_{\text{frame}}$ .

Possible standing pressure waves could fudge the velocity measurement. That is excluded by independent analysis of the three arrays. Additionally the measurement of obvious mass movements, like tip and tail of the jet, have been determined manually and agree with the results of the digital analysis. In Figure 4.9 the jet velocity for a representative event is plotted as a function of time.

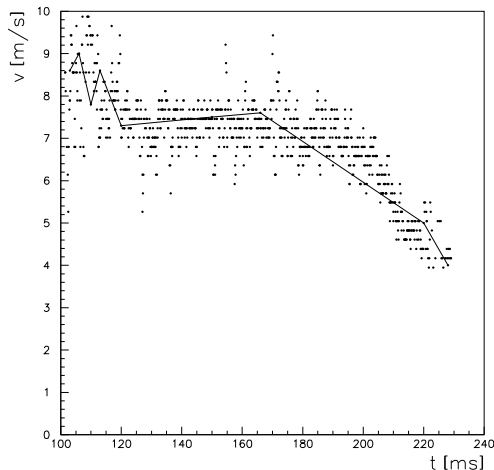


**Figure 4.9:** Velocity of the jet as a function of time. The digital retrieved data (points) corresponds to the measurement of obvious jet movement analysed manually (line).

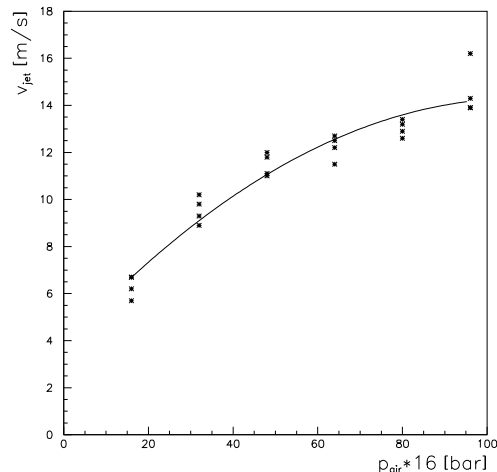


**Figure 4.10:** Jet velocity as a function of the driving pressure.

The jet velocity as a function of the air pressure in the pump is indicated in Figure 4.10, obtained from calibration measurements without magnetic field. With a trigger gate of 100 ms of the air actuated valve the corresponding jet length is in the order of 1 m. For low velocities the gate was prolonged to keep the length several times above the drift length.

### Jet in the Evacuated Chamber

Normally the jet was injected in one atmosphere Argon. Applying a pressure of a few Torr in the jet chamber showed negligible change in the width. After a drift path of 10.3 cm at low pressure the average width at 2 bar driving pressure measured as  $w = 4.1$  mm,  $w = 4.2$  mm in atmosphere. At 4 bar driving pressure the width changed to 5.1 mm and 5.2 mm respectively. The jet velocity at low pressure in the chamber corresponds to the one if the chamber is filled with argon (Figure 4.10).

### 4.2.2 Dynamic Pressure

The piezo-sensor records the dynamic pressure losses in the high pressure hose (Figure 4.11). With a typical delay of 60 – 90 ms after the trigger the pressure drops. This is caused by the filling of the air supply to the air-actuated valve and the opening of the pneumatic valve itself. The delay of valve opening is related to the strength of the magnetic field. The jet passes with an additional delay to reach the view area. From this time (100 – 140 ms) onwards the velocity data are indicated (Figure 4.11). The trigger gate ends after 100 ms. The pressure drop gets smaller with the magnetic field. This indicates a resistive force on the ball valve and/or the mercury in the pipe.

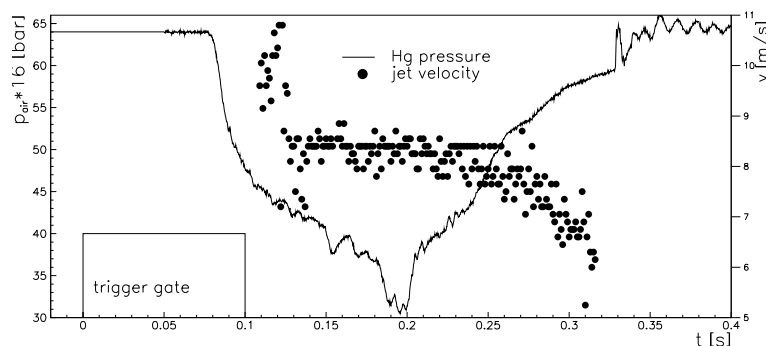


**Figure 4.11:** Pressure in the mercury supply and the jet velocity as a function of time. The pressure loss is recorded with the piezo-gauge. The velocity is digitally retrieved from the movies.



### 4.2.3 The Sprayed Jet

The two types of nozzle produced two different kind of jets. From the 'short' nozzle the jet could not evolve properly and the jet looks more like a 'cloud' of mercury ('sprayed' jet).

Figure 4.12 shows the sprayed jet in the absence and presence of a magnetic field. The Jet could not be stabilised by the magnetic field, independently of the inclination and the position of the nozzle referred to the magnetic field. The frames are such chaotic that a digitally analysis is impossible (with reasonable effort). The number of small single droplets is reduced in the case of magnetic field presence. Clearly visible is the effect of the repulsive force by the magnetic field, where the droplets tend to smooth and are stretched in backward direction. Also, the velocity of the jet is reduced similar to the observation in the case of the 'stable' jet (Section 4.2.4).

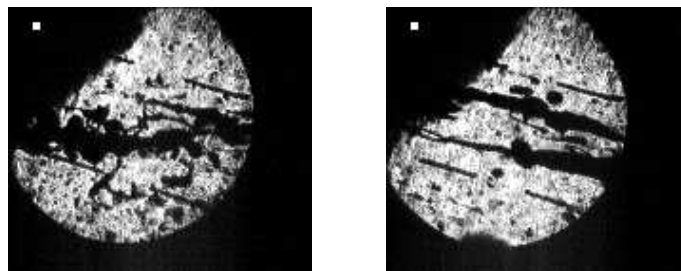


**Figure 4.12:** The sprayed jet without (left) and in a magnetic field (right). The jet arrives from the left hand side.

### 4.2.4 The Stable Jet

With the 'long' nozzle a different type of jet, a 'stable' jet was obtained. Single frames from the film of the 'stable' jet injected under 6 degree are presented in Figure 4.13. The tip of the jet and the jet itself recorded 10 ms after the passage of the tip are given for injection velocities between 8 and 12 m/s and a field strength up to 19.3 Tesla. With increasing field, the smoothness of the jet envelope is clearly improved thus demonstrating the expected damping. The results presented in Section 4.2.5-4.2.8 are obtained with running a 'stable' jet.

### 4.2.5 The Jet Tip

A 4 mm diameter jet injected in a 20 Tesla field stabilised at the desired injection angle within 10 ms (Figure 4.14). Minor misalignments or oscillation around the axis of the jet cannot be excluded. The first figure shows the jet width for a jet without magnetic field. At 19 T the tip is more pointed. The width of the jet is fully established at  $t < 10$  ms. The time is reset to zero at the first indication of the jet, thus correcting for the time delay caused by the air actuated valve in a magnetic field. Clearly seen in Figure 4.14 is the damping of the surface oscillations: Larger fluctuations of the width are suppressed by the magnetic field.

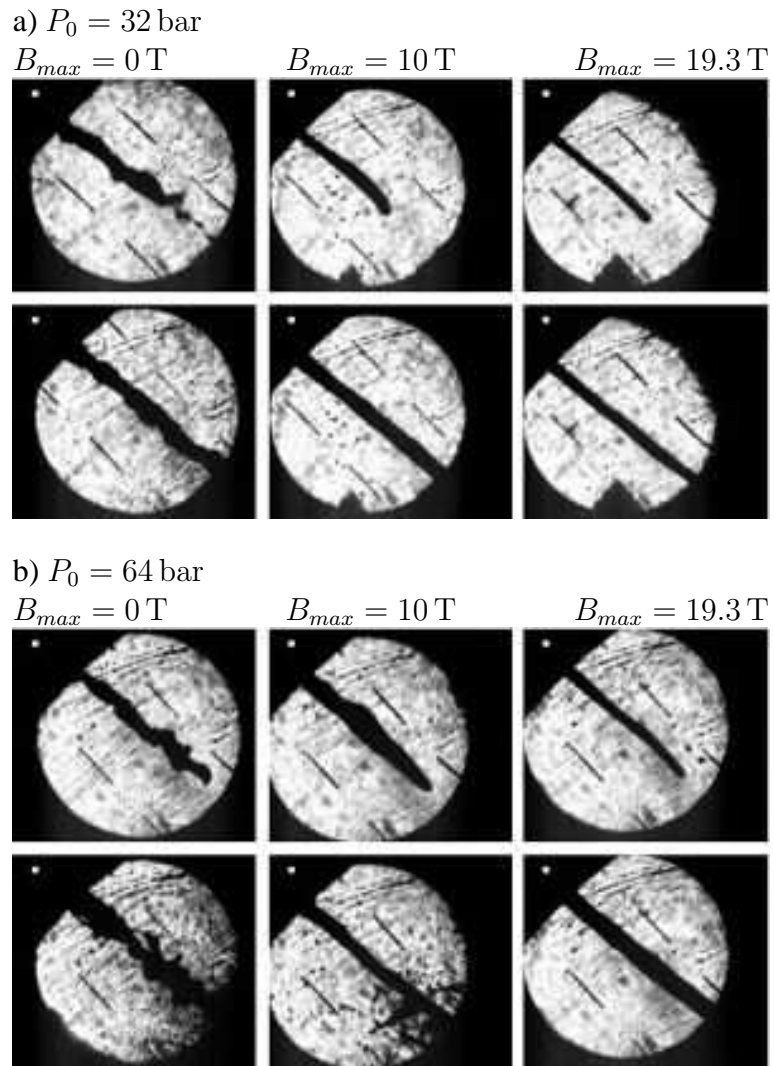


**Figure 4.13:** Mercury jet injected at 6 degree into the bore of the M9 magnet at GHMFL Grenoble. The tip of the jet is presented in the top row and the second row is a snap shot of the jet taken 10 ms after the passage of the tip. The static pressures driving the mercury were 32 (a) and 64 bars (b)

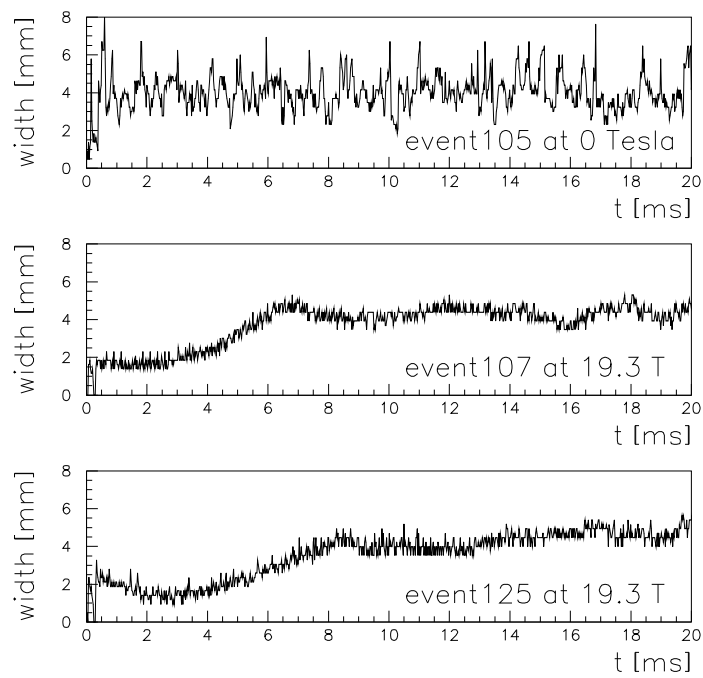


**Figure 4.14:** The width of the jet as a function of time at 0 T and 19.3 T. A clear smoothing of the jet shape at 19.3 T is visible.

### 4.2.6 Deflection

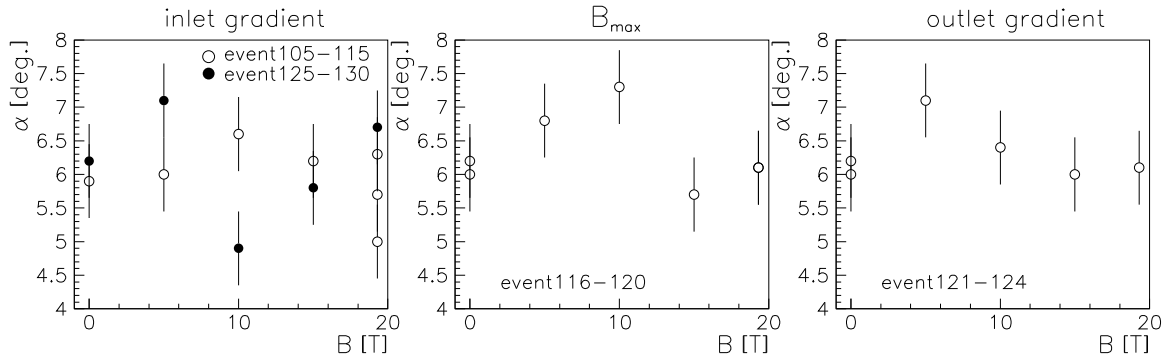


**Figure 4.15:** Deflection as a function of the magnetic field for several positions of the drift path as given in Figure 4.6.

The injection of the inclined jet showed no deflection of the jet. In Figure 4.15 the inclination of the jet is plotted for a drift path through the positive gradient (event 105-115 and 125-130), through the maximum field (event 116-120) and out of the magnetic field (event 121-124). The error indicated originates from the uncertainty given by the resolution of the camera. The angle is defined as the inclination between jet and solenoid axis.

### 4.2.7 Jet Diameter

The jet diameter was studied as a function of the position of the jet in the magnetic field. The diameter has a general tendency to decrease with increasing magnetic field (Figure 4.16-4.18). The typical width decrease is about 10% for the injection of a collinear jet. In Figures 4.16 and 4.17 the width for the jet on entering the magnetic field is shown for two different distances of observation from the tip of the nozzle.

A large effect is seen (Figure 4.18, open circles), where the drift path is in the negative gradient after the maximum field. A width decrease of about 30% is measured. This indicates the occurrence of MHD effects in the pipe itself. The width of the jet on traversing the positive gradient, implying the position of the valve and nozzle in a comparable low magnetic field and gradient, is constant as indicated in Figure 4.18. The MHD effects of the confined flow of the mercury in the valve and the nozzle are subject to further investigations.

For the tilted injection at  $6^\circ$  the change in width can result in a deformation of the cross section of the jet. The tilted injection makes the problem asymmetric in respect to the magnetic axis and could cause a broadening in the view axis. However, this effect could not be analysed with our diagnostics.

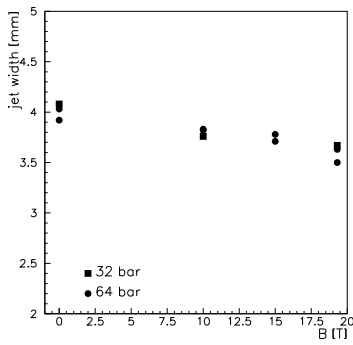


**Figure 4.16:** Pinching for the straight jet on traversing the field maximum measured at a distance  $d = 3.3$  cm.

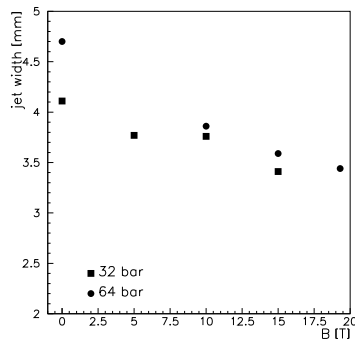


**Figure 4.17:** Pinching for the straight jet on traversing the field maximum measured at  $d = 10.3$  cm.

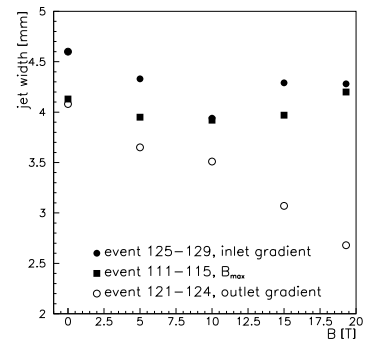


**Figure 4.18:** Pinching of the inclined jet.

### 4.2.8 Velocity

The velocity measurement relies on the shift of the jet shadow. This implies that the velocity measured is the one of the surface only. Figure 4.13 shows samples of the fully established jet. At high magnetic field the surface oscillations are damped and the amplitude is comparable to the resolution. This effect results in difficulties to determine precisely the velocities at high magnetic field. Approaches by different diagnostics are mentioned in the conclusions. Overall the velocity decreases with the magnetic field (Figure 4.19). The tip of the jet has a lower velocity than the fully established jet.

Jet velocities are presented in Figure 4.19 as a function of the magnetic field strength for different initial pump pressure and injection angles. The expected tendency for the velocity of the jet to be reduced with increasing field is observed. Independent of the injection angle the velocity is about 25% less at highest magnetic field.

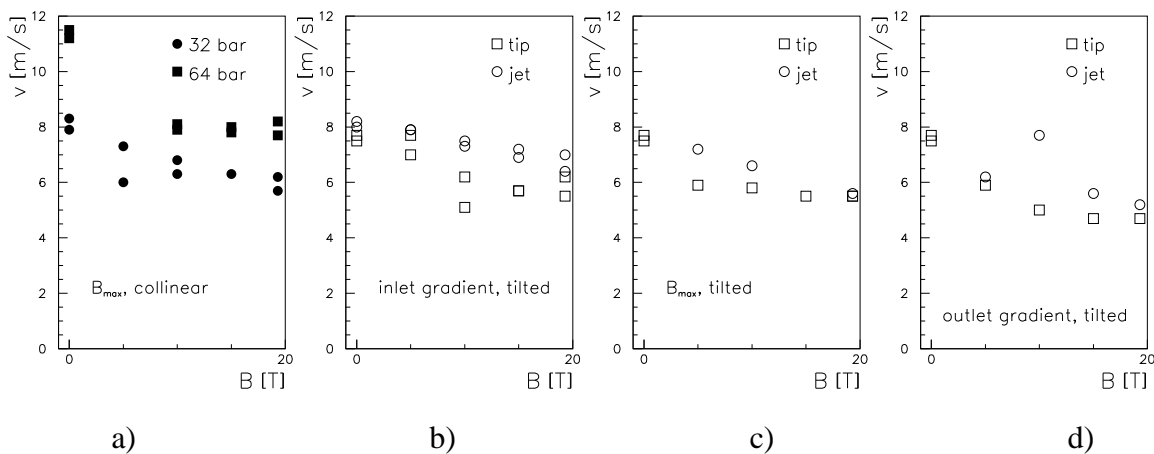


**Figure 4.19:** Jet velocity versus magnetic field

### 4.3 Magnetohydrodynamics

In this section we discuss the possible behaviour of the metal jet target within the inhomogeneous 20 T magnetic field of a neutrino factory. Three cases will have to be considered:

- the flow of the liquid through the supply pipe to the nozzle with the supply pipe being placed in the gradient of the magnetic field;
- the injection of the free jet into the magnetic field;
- the behaviour of a disrupted jet in the magnetic field after the interaction with the proton beam, and its removal from the intersection region.

The first two cases can be directly bench-marked with the experiment performed at GHMFL, where both effects can not be clearly separated. The flow in a pipe is governed by the magnetohydrodynamics of a contained flow of a conducting liquid in the presence of an inhomogeneous field (e.g. [56]). Second, the free jet as for a neutrino factory has been studied analytically and numerically by several groups [57]-[58] for simplified systems. The most basic geometry of the target jet, a perfect mercury cylinder penetrating into a 20 T coaxial solenoid, was addressed numerically and shows major deformations [59] (Figure 4.20 and 4.21). The collected data are to benchmark this simulation code.

The few-nanosecond long 24 GeV proton pulse will interact with the target in the middle of the high field region and disrupt the jet as discussed in the previous chapter. Such a situation, the effect of perpendicular velocities due to thermal expansion, has been introduced in the setup presented here via a very turbulent stream produced with a short nozzle (Section 4.2.3). Perpendicular velocities were small ( $< 0.1$  m/s), while proton induced shocks, as presented in Section 3, are expected to cause velocities of several tens of meter per second.

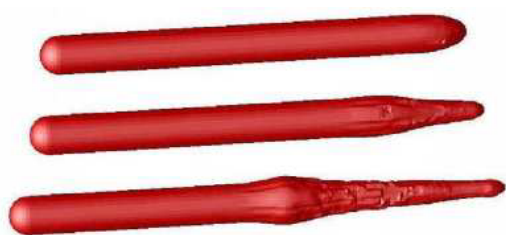


**Figure 4.20:** Numerical simulation of a mercury jet entering and ...



**Figure 4.21:** .. leaving a magnetic field [59]

On entering the magnetic field (Figure 4.20), a repulsive force is acting on the jet, which shapes it like a torpedo. In Figure 4.21 the leaving jet is displayed, where the pressure wave on entering is still visible. In a negative gradient negative pressure is disrupting the jet as indicated on the very far right. The effects are exaggerated in the figures.

The analytical evaluation given in [60] is compared with the experimental results. In a metal jet penetrating axially into a solenoid field, the change in magnetic flux induces an electric field, where the resulting current density is approximated by

$$j_\varphi \approx \frac{rv\sigma}{2} \frac{dB_z}{dz}, \quad (4.1)$$

where  $v$  and  $r$  are velocity and radius of the jet,  $\sigma$  the conductivity of mercury. As the maximum gradient is in the same order of magnitude as the one of the 'US solenoid', the current density of  $100 \text{ A/cm}^2$  caused in the M9 at GHMFL is comparable. The largest contribution of all force components is the axial force [60] causing a velocity decrease of the order of  $\text{cm/s}$ . This is two orders of magnitude below the ones observed. The repulsive force on the free jet can not be the only explanation for the velocity decrease. The MHD of confined flow has to be taken into account. The deflection was never assumed to be relevant [61] and the experimental results confirm this. The elliptical deformation of the jet is an effect caused by the asymmetry of the tilted injection of the mercury jet in respect to the solenoid axis. Such a deformation would result in a diameter decrease in the plane perpendicular to the viewing axis of the M9 setup. In [61] the distortion  $\epsilon = -\frac{\Delta y}{r}$  including surface tension is estimated to be at the ten percent level. This would explain the experimentally obtained results. But it does not explain, why the smaller diameter occurs already close to the nozzle exit and is kept rather constant along the drift path. This indicates once more the importance of the magnetohydrodynamics in the nozzle.

## 4.4 Conclusions

The injection of a fast mercury jet ( $10 \text{ m/s}$ ) under an angle of 6 degree field was successfully observed. The experimental method to investigate the magneto-fluid-dynamic effects of a high velocity liquid metal in a high magnetic field magnet has been demonstrated by recording the behaviour of a mercury burst entering in the gradient of a 20 Tesla solenoid at GHMFL Grenoble.

The observed reduction of velocities by about 25% (Section 4.2.8) in a magnetic field and the narrowing of the jet by 10% (Section 4.2.7) upon injection is significantly larger compared to the predictions for a free mercury jet and indicates the importance of MHD effects in the piping. The magnetic field causes damping of surface oscillations (Section 4.2.5), where the amplitude is in the order of the spatial resolution ( $\Delta x \approx 0.33 \text{ mm}$ ). A deflection of the jet has not been observed (Section 4.2.6).

The damping of disrupting jets, simulated by highly turbulent ejection, could not be observed (Section 4.2.3). Predictions [59] of stabilising instabilities could not be validated, where the initial conditions do slightly differ.

We have observed, that the full width  $d = 4 \text{ mm}$  of the jet establishes within 10 ms (Section 4.2.5). On injecting a mercury jet into a magnetic field, a repulsive force acted on the tip of the mercury jet. This resulted in a shaping of the mercury tip towards a shape similar the tip of a rocket. It is not excluded that the nominal jet will stabilise into a cylindrical target within the 20 ms available between proton pulses induced disruptions.

MHD effects occurring in the valve are specific of the experimental setup. MHD of confined flow are an issue for the final scheme of the target area as well and require a full MHD simulation of the injection circuit. The results presented serve as benchmark for numerical codes already in development.

Confined flows of conducting liquids are a major subject of magnetohydrodynamics. The impact on the design for a mercury jet target are bigger than assumed. We observed that the MHD effects in the confined circuit are not negligible. In the present baseline, the mercury jet is ejected from a nozzle placed at the beginning of the coil for the 20 T-field. The possibility of placing the nozzle in a region with low magnetic field and low gradient should be kept as an option in order to keep MHD effects in the mercury circuit small.

Further studies with the setup are limited in radius and velocity of the jet, although the basic principle could be validated. The optical diagnostics were limited in measuring the velocity of a smooth jet due to the method of observing the shadow. The additional use of the a radar or a laser vibrometer would overcome this difficulty by measuring the Doppler shift. Nevertheless, diagnostics similar to the system used up to now are necessary in order to observe properties like the width of the jet.

In view of a full scale experiment of the target section of the US scenario, the next step should be the mechanical construction of a mercury jet of nominal radius and velocity. The energy stored in such a jet is in the order of a few tens kilowatt and indicates the challenge of this project. At GHMFL the construction of a hybrid solenoid, with a bore of  $d = 40$  cm in the 17 Tesla configuration, should be finished by spring 2003. The large bore and the almost nominal field would be highly suitable for further investigations of the magnetohydrodynamics of the mercury circuit and the jet itself.



# Chapter 5

## Conclusion

Within the Neutrino Factory Working Group in the PS division of CERN, experiments on the behaviour of high power proton targets have been performed. That covers proton induced shocks in a metal target and the behaviour of a fast metal jet in a high magnetic field.

The exposure of different configurations of mercury samples to proton beams at ISOLDE/CERN and AGS/BNL (E951 collaboration) revealed the behaviour of its free surface as a function of the beam parameters like intensity and spotsize. The response of the nominal target for a neutrino factory was obtained by an one order of magnitude extrapolation of these results.

A mercury jet has been successfully injected into a 20 Tesla solenoid field with velocities of about 10 m/s. The experiment revealed the importance of magnetohydrodynamic effects occurring in the mercury circuit next to the free jet. The experimental results serve as benchmark for numerical codes, which are a necessity to understand such systems in detail.

The diagnostics used in both cases is optical observation by a high speed camera followed by digital image processing. The obtained data aims at benchmarking the assumptions of the physical model of the numerical MHD codes.

The concept of a metal jet as a secondary particle target for high power proton beams is still valid and we propose further experiments on MHD of the molten metal circuit.

In total 6 years of full time equivalents directly involved have been invested in establishing the experiments on proton induced shocks and magnetohydrodynamics. This does not include the participation of members from the US collaboration.

# Appendix A

## Material Properties

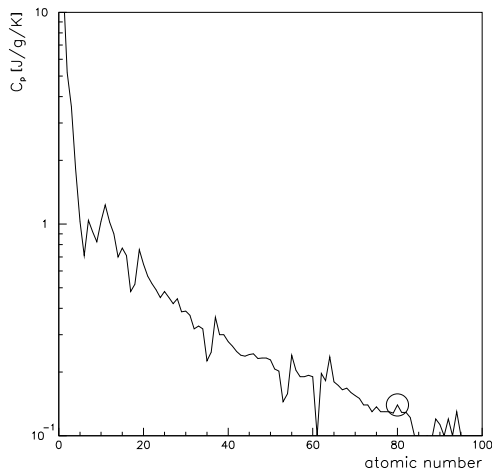


**Figure A.1:** Heat capacity as a function of atomic number [63] at ambient temperature. Mercury is indicated with a circle.

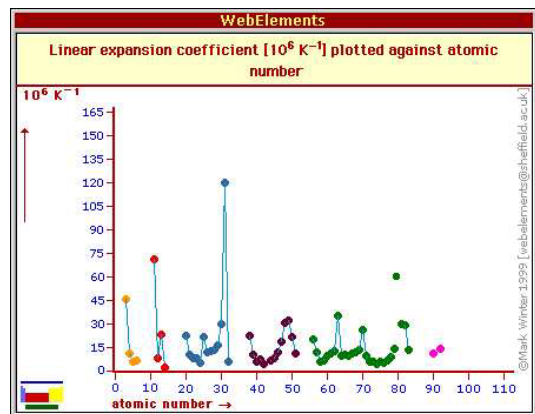


**Figure A.2:** Thermal expansion coefficient at  $20^\circ\text{C}$ . Mercury (atomic number 80) has a thermal expansion coefficient a few times higher than elements with comparable atomic number and density.

property	char	value	unit
atomic number	Z	80	-
atomic mass	A	200.59(2)	-
density	$\rho$	13.6	kg dm <sup>3</sup>
linear expans. coeff.	$\alpha$	$60 \cdot 10^{-6}$	K <sup>-1</sup>
$v_{sound}$ (at 20 °C)	c	1407	m/s
specific electrical resistance	$\rho_{\Omega}$	$96 \cdot 10^{-8}$	$\Omega$ m
bulk modulus	$\frac{1}{\kappa}$	25	GPa
dynamic viscosity	$\mu$	1.552	$\frac{\text{kg}}{\text{m}\cdot\text{s}}$
kinematic viscosity	$\nu$	$1.145 \cdot 10^{-4}$	m <sup>2</sup> s <sup>-1</sup>
mineral hardness		1.5	
dielectric constant	$\epsilon$	1.00074	-
surface tension (20 °C)	$\sigma$	$4.6 \cdot 10^{-1}$	$\frac{\text{J}}{\text{m}^2}$
surface tension (20 °C, air-Hg)	$F_{\sigma}$	$0.5 \cdot 10^2$	$\frac{\text{N}}{\text{m}^2}$
magnetic permeability	$\mu$	$< 4\pi \cdot 10^{-7}$	H/m

**Table A.1:** properties of mercury

linear expans. coeff.	$\alpha_{SS316LN}$	$16 \cdot 10^{-6}$	K <sup>-1</sup>
-----------------------	--------------------	--------------------	-----------------

**Table A.2:** properties of stainless steel SS316LN

linear expansion coefficient	$\alpha_{Al}$	$23.1 \cdot 10^{-6}$	K <sup>-1</sup>
$v_{sound}$ (at 20 °C)	c	5100	m/s

**Table A.3:** properties of Aluminium

## **Appendix B**

### **The mercury jet setup for the MHD experiment**



**Figure B.1:** The experimental setup at GHMFL M9. The vertical bore of the solenoid is lowered in the floor, where the blue hose is pointing to. To the other end the pump device is connected. On the left hand side the gas rack can be seen.

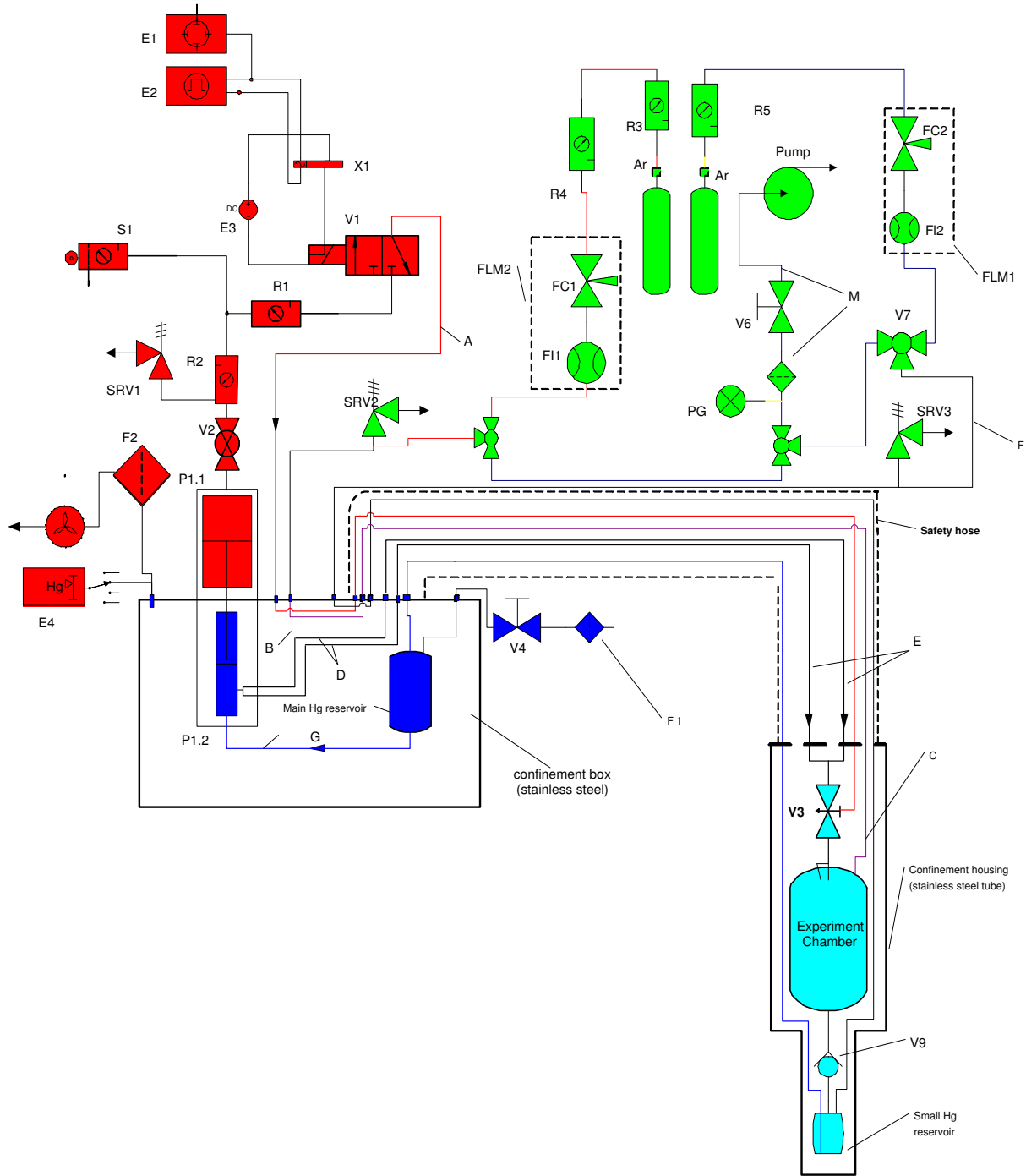


**Figure B.2:** Flowchart of the mercury pump system for the MHD jet setup (legend see Table B.1)

index	description
E1	Oscilloscope Tektronix TDS3032 300Mhz, 2.5Gs/s
E2	Pulse Generator Philips/Fluke PM5786B 1Hz-125MHz
E3	Power Supply 24V DC
E4	Mercury Vapor Detector Mercury Instruments VM-3000
F1, F2	Charcoal Filter
FLM1,FLM2	Flow meter Vögtlin Q80EE S1 M12G A2.0E
FC1	Flow Control for Noble Gas
FC2	Flow Control for Noble Gas/Air
FI1,FI2	Flow Indicator (Flow meter) 0-10 l/min
PG	Pressure gauge for under-pressure
P1.1	NORDSON 25B Piston Pump, Air Motor
P1.2	NORDSON 25B Piston Pump, Hydraulic Section
P3	Rotary pump
R1	Air Pressure Regulator
R2	Air Pressure Regulator
R3	Pressure Regulator for Argon LHC15 200bar→15bar
R4	Pressure Regulator for Argon BS300/01 15bar→10-100 mbar
R5	Pressure Regulator for Argon and Air
S1	Air Service Station (Filter, Pressure Regulator)
V1	3/2 Pneumatic Valve
V2	Shut Off Valve for Air Motor of Piston Pump
V3	NORDSON A7A Ball Tip Valve (air actuated)
V4	Screw down valve
V5	Pneumatic valve / non return
V6	Screw down valve
V7	Mixing valve
V8	Three way valve
V9	One way valve
SRV1	Safety Relief Valve 4.1 bar
SRV2,SRV3	Safety Relief Valve “Nupro”, 0,2-3bar (calibrated to 0,2bar)
X1	Reed Relays 5V
	<b>Tube and hose types, contained medium</b>
A	4x6mm Rilsan (Polyamide) flexible hose; medium: compressed air
B	5x6mm stainless steel tube; medium: compressed air
C	4x6mm Rilsan (Polyamide) flexible hose; medium: compressed air
D	6x8mm stainless steel tube; medium: mercury (high pressure)
E	2x NORDSON high-pressure hoses, Teflon 1/4”, stainless steel nipples and swivel nuts; medium: mercury (high pressure)
F	6x8mm stainless steel tube; medium: compressed air
G	1/2” plumbing (316 stainless steel); medium: mercury
I	6x8mm stainless steel tube; medium: air
L	1/2” plumbing (316 stainless steel); medium: mercury
M	4x6mm Rilsan (Polyamide) flexible hose; medium: compressed air
	Feedthrough fittings: Gyrolok, stainless steel

**Table B.1:** Components of the mercury pump system for the MHD jet setup



**Figure B.3:** A full view of the MHD jet (64 bar, long nozzle at 6 degree) at 11 ms and ...



**Figure B.4:** ... 76 ms after ejected from the nozzle. The splashing of the mercury in backward direction along the steel frame can be seen.



# Appendix C

## Cavitation Bubbles

The proton induced splashing observed in the free jet could be generated by the propagating compression shock wave immediately following the energy deposition. Could the observed splashing be the result of the shock wave generated by a collapsing vapor bubble (signature of cavitation) close to the free liquid surface? To address this point, the monitoring of the collapsing vapor bubble is simpler in transparent media. Cavitation is a well-studied phenomenon in the framework of its deleterious corrosion on piping or propeller. Such a material test setup where the vaporisation of water is induced by means of a spark discharge was modified to study cavitation in the vicinity of a free surface. Qualitative information was gained by recording with a digital camera the light of a flash transmitted through the liquid few millisecond after the spark. While the initial shock did not disrupt the surface of the liquid, a vapor bubble collapsing close to the surface did. On the picture presented in Figure C.1 (M.Farhat, E.Robert, EPFL, Lausanne) a thin jet is visible that has similarities with some of the proton induced splashes in mercury jets shown in reference 3. In both cases, the energy deposited is of a few Joule, however, the influence of the type of fluid, position and geometry of the spark gap or bubble has not been investigated. While the cavitation corrosion pattern was observed in contained lead targets, any conclusion on its appearance in free jets is premature. However, this investigation shall be continued. Vapor bubble will be generated close to the free surface by Neodim YAG laser to avoid the actual reflection of pressure waves on the electrodes and to reduce the heat deposition time from few millisecond down to a fraction of the relaxation time (few ns).



**Figure C.1:** Water vapor bubble collapsing close to the free surface. The velocity of the micro jet was not measured. A liquid dome is formed around the micro jet.

# Bibliography

- [1] <http://www.sns.gov/>
- [2] Evidence for oscillation of atmospheric neutrinos. The Super-Kamiokande Collaboration, Phys. Rev. Lett. 81, p.1562-1567, 1998
- [3] SNO collaboration, Direct Evidence for Neutrino Flavor Transformation from the Neutral-Current Interactions in the Sudbury Neutrino Observatory, <http://www.sno.phy.queensu.ca/>, 2002
- [4] S. Geer, Neutrino beams from muon storage rings: characteristics and physics potential, Phys.Rev.D, Vol 57, p.6989-6997, 1998
- [5] LEP Electroweak working group, A Combination of Preliminary Electroweak Measurements and Constraints on the Standard Model, CERN-EP/2001-098, hep-ex/0112021
- [6] M.Apollonio et al., hep-ex/9907037
- [7] A. Cervera et al., Golden measurements at a neutrino factory, hep-ph/0002108
- [8] J. Burguet Castell et al., On the measurement of leptonic CP violation, CERN-TH/2001-081
- [9] L. Wolfenstein, Phys. Rev. D 17, 2369, 1978
- [10] S.P. Mikheev and A. Yu. Smirnov, Sov. J. Nucl. Phys. 42, 913, 1985
- [11] The ICFA/ECFA Workshop, Neutrino Factories based on Muon Storage Rings, Lyon, NIM-A 451 No.1, 2000
- [12] R. Palmer, C.D. Johnson, E. Keil, A Cost-Effective Design for a Neutrino Factory, CERN-SL-99-070, 1999
- [13] Feasibility Study-II of a Muon-Based Neutrino Source, ed., S. Ozaki, R. Palmer, M. Zisman, and J. Gallardo, BNL-52623, 2001 (<http://www.cap.bnl.gov/mumu/studyii/FS2-report.html>)
- [14] R.Raja (editor) et al., Status of Neutrino Factory and Development and Future Plans, PRSTAB, 2002
- [15] Y. Mori, Neutrino Factory in Japan: Based on FFAG accelerators, proceedings EPAC02, Paris, 2002
- [16] R. Garoby, M. Vretenar, Status of the Proposal for a Superconducting Proton Linac at CERN, CERN/PS/ 99-064 (RF), 1999
- [17] F. Dydak, Spokesperson, Proposal to Study Hadron Production for the Neutrino Factory and for the Atmospheric Neutrino Flux, HARP PS-214, CERN-SPSC/99-35, SPSC/P315, 1999
- [18] <http://megapie.web.psi.ch/about/about.shtml>
- [19] L.Cinotti, The Pb-Bi cooled XADS status of development, Journal of Nuclear Materials 301(2002) 8-14

- [20] B.Jonson, Present and future RNB facilities in Europe, Nucl.Phys. A 701 (2002) 35c
- [21] <http://isolde.web.cern.ch/ISOLDE/>
- [22] <http://www.ganil.fr/eurisol/>
- [23] R.Catherall, neutron converter targets, presentation, ISOLDE physics workshop, CERN, 2001
- [24] D.Kaplan, Muon collider/neutrino factory: status and prospects, NIM A 453 (2000) 37
- [25] S.Geer, Muon colliders move nearer, CERN courier article, 1997, [http://www.fnal.gov/projects/muon\\_collider/cern\\_courier/article.html](http://www.fnal.gov/projects/muon_collider/cern_courier/article.html)
- [26] H.Schoenauer et al., Proton Drivers for Neutrino Factories: The CERN Approach, CERN-NUFACT Note 046, 2000
- [27] P.Thieberger and H.G.Kirk, Autoradiographic determination of the AGS proton beam-spot size for experiment E951, <http://www.hep.princeton.edu/~mcdonald/mumu/target/muc0236.pdf>
- [28] H. L. Ravn, The CERN Target and Horn Concept for a Neutrino Factory Based on Muon Beams. proc. NuFACT01, NIM A, Japan, 2001
- [29] S.Van Der Meer, A directive device for charged particles and its use in an enhanced neutrino beam, CERN 61-7
- [30] A.Ball, A.Blondel, S.Gilardoni and N.Vassilopoulos, Preliminary Magnetic Horn Studies in the Collection Scheme for a Neutrino Factory (Proc. NuFact'99, Lyon, NuFact Note 4, 1999)
- [31] S.Gilardoni (CERN PS-PP), private communication
- [32] B.Autin et al., Conducting Target for Pion Production, CERN NuFact note 91, 2001
- [33] H.Kirk et al., Target Studies with BNL E951 at the AGS, proceedings PAC'01, Chicago, 2001
- [34] P.Sievers, A Stationary Target for the CERN-Neutrino-Factory, CERN-NuFact-Note 065, 2000
- [35] P.Sievers, J.Letry, private communication
- [36] B.King et al., A Cupronickel Rotating Band Pion Production Target for Muon Colliders, Proc. PAC99, NY, 1999
- [37] presentations by J.Haines and B.Riemer, Fifth International Workshop on Spallation Materials Technology, Charleston, SC, proceedings will be published in Journal of Nuclear Materials (Elsevier)
- [38] N.Mokhov, " $\pi/\mu$  Yield and power dissipation for carbon and mercury targets in 20-Tesla solenoid with matching section", MUCOLL Note 61, BNL 1999
- [39] Grenoble High Magnetic Field Laboratory, <http://ghmfl.polycnrs-gre.fr/>
- [40] H.G. Kirk, *TARGETRY FOR A  $\mu^+\mu^-$  COLLIDER*, Proceedings of the 1999 Particle Accelerator Conference, New York, March 1999, p.3029.
- [41] James Alessi, et al., *An R&D Program for Targetry and Capture at a Muon-Collider Source*, Proposal submitted to Brookhaven National Laboratory, (Sept. 28, 1998).
- [42] P.Sievers, P. Pugnât, Response of Solid and Liquid Targets To High Power Proton Beams for Neutrino Factories, CERN-LHC/2000-4 (CERN-NuFACT Note 035), 2000

- [43] J.Letry et al., Effects of Thermal Shocks on the Release of Radio-isotopes and on Molten Metal Target Vessels, proc. EMIS-14, Canada, 2002
- [44] A. Fabich, J.Letry, Experimental Observation of Proton-Induced Shocks and Magneto-Fluid-Dynamics in Liquid Metal, proceedings NuFact'01, NIM A, 2001
- [45] A.Fabich, M.Benedikt, J.Letry, Experimental Observation of Proton-Induced Shocks in Free Surface Liquid Metal Targets, proceedings IWSMT5, J.of Nuclear Materials, 2002
- [46] K.McDonald et al., THE R&D PROGRAM FOR TARGETRY AT A NEUTRINO FACTORY, PAC'01, Chicago, 2001
- [47] M.Benedikt, CERN PS-OP, private communication
- [48] K. Brown, *First Beam Tests of the Muon Collider Target Test Beam Line at the AGS*, Proceedings of the 2001 Particle Accelerator Conference, Chicago, 2001
- [49] D.Schaffarzick, Experimental Investigation of Proton Induced Thermal Shocks and Magneto-hydrodynamic Effects in Molten Metal Pion Production Targets for a Neutrino Factory, Wels (Austria), 2001
- [50] N.V. Mokhov, "The Mars Code System User's Guide", Fermilab-FN-628 (1995).  
N.V. Mokhov, "MARS Code Developments, Benchmarking and Applications", Fermilab-Conf-00-066 (2000)  
N.V. Mokhov, S.I. Striganov, A. Van Ginneken, S.G. Mashnik, A.J. Sierk and J. Ranft "MARS Code Developments", Fermilab-Conf-98/379 (1998)  
LANL Report LA-UR-98-5716 (1998); nucl-th/9812038 v2 16 Dec 1998  
O.E. Krivosheev and N.V. Mokhov, "A New MARS and its Applications", Fermilab-Conf-98/43 (1998)
- [51] A.Hassanein, Argonne National Laboratory, private communication
- [52] J. Letry, A. Fabich, S. Gilardoni, M. Benedikt, GMHFL Grenoble, EPFL, Thermal shocks and magnetohydrodynamics of high power mercury targets, proc. NuFact02, London, J. Phys. G, 2002
- [53] A.Hassanein, Liquid metal targets for high-power applications: pulsed heating and shock hydrodynamics, *Laser & Particle Beams*, Vol.18, 2000  
A.Hassanein and I.Konkashbaev, Numerical simulation of liquid metal jet penetrating a strong magnetic field, Argonne National Laboratory Report, ANL-ET/01, 2001
- [54] G.Jesse, EMDS report 351111 v.1, CERN, 2002
- [55] A. Astone, Experimental investigation of MHD in molten metals and study of homogeneity of radioactive amalgams, diploma thesis, Universit degli Studi di Genova - Facolt di Ingegneria, 2002
- [56] J.R.Moreau, *Magnetohydrodynamics*, ISBN 0-7923-0937-5, Kluwer Academic Publishers, Dordrecht, 1990
- [57] P.Thieberger, "Estimated perturbations of the axial motion of a liquid-metal jet entering a strong magnetic field", MUCOLL Note 182, BNL 2000
- [58] R.Samulyak, Numerical simulation of hydro- and magnetohydrodynamic processes in the Muon Collider target, *Lecture Notes in Comp. Sci.*, Springer-Verlag, Berlin - Heidelberg, 2331 (1992), 391-400.
- [59] R.Samulyak (BNL), The FronTier Code, private communication, <http://www.ams.sunysb.edu/~shock/FTdoc/FTmain.html> and [58]

- [60] J.Gallardo et al., Calculations for a mercury jet target in a solenoid magnet capture system, proc. PAC01, Chicago, 2001
- [61] J.Gallardo et al., First order perturbative calculations for a conducting liquid jet in a solenoid, MUC-note-target-242 (muon tech. note MU-047), BNL, 2002
- [62] A.Hassanein and I.Konkashbaev, Dynamics of liquid metal jets penetrating a strong magnetic field in high-power colliders, proc. PAC01, Chicago, 2001
- [63] <http://web.mit.edu/3.091/www/pt/>

# Curriculum Vitae

## Adrian Fabich

### personal data

Name: Adrian Fabich  
date of birth: 17. August 1974  
born in: Sao Paulo, Brazil  
Nationality: Austria  
Marital status: single

### address

Bürgerspitalgasse 9  
1060 Vienna  
Austria

e-mail: [adrian.fabich@cern.ch](mailto:adrian.fabich@cern.ch)

homepage: <http://cern.ch/Adrian.Fabich>

### education

Jan.2003- until Nov. 2002 fellow (post-doctoral position) at CERN (CH)  
PhD work on 'High Power Proton Beam Shocks and Magnetohydrodynamics in a Mercury Jet Target for a  $\nu$ -Factory'

March-Oct. 2000 PhD work on 'Acceleration of Macromolecules'

Jan. 2000 degree of Diploma-Engineer at Technical University of Vienna

1999-2000 diploma work at CERN (CH), thesis on 'Quality Control of MDT chambers in the ATLAS Muon Spectrometer'

1993-1999 study of 'Technical Physics' at Vienna University of Technology

Jan – Aug 1993 Military service in the Austrian army (ABC defense)

1984 – 1992 High school, Akademisches Gymnasium Wien

### part-time jobs

since Feb. 1997 software development and technical administration  
at Wiener Kunstauktionen (Vienna Art Auctions)

June 1998 –  
January 1999 network (Windows NT) administration at Call Us Assistance, Vienna

September 1997 technical assistant, GSI, Darmstadt

July – Aug. 1995 truck driver, Koenig&Ebhardt, Vienna

July – Aug. 1994 truck driver, Gebrueder Weiss, Vienna

July – August 1991 and  
July – Sept. 1992 administrative work, German Courses for Foreigners at the University of Vienna

### languages

German (mother tongue), English, French

### computer skills

MS Windows (OS and applications), Unix, C/C++, Fortran, Latex, Mathematica (Wolfram Research), Geant 4, MS office, AutoCAD, BridgeView

## List of Publications

- A. Fabich, J.Letry, Experimental Observation of Proton-Induced Shocks and Magneto-Fluid-Dynamics in Liquid Metal, proceedings NuFact'01, NIM A, 2001
- A.Fabich, M.Benedikt, J.Letry, Experimental Observation of Proton-Induced Shocks in Free Surface Liquid Metal Targets, proceedings IWSMT5, J.of Nuclear Materials, 2002
- J.Letry et al., Effects of Thermal Shocks on the Release of Radio-isotopes and on Molten Metal Target Vessels, proc. EMIS-14, Canada, 2002
- H.Kirk et al., Target Studies with BNL E951 at the AGS, proceedings PAC'01, Chicago, 2001
- K.McDonald et al., THE R&D PROGRAM FOR TARGETRY AT A NEUTRINO FAC-TORY, PAC'01, Chicago, 2001
- P.Gruber (ed.) et al., The Study of a European Neutrino Factory Complex, CERN/PS/2002-008 (NuFact note)
- R.Raja (editor) et al., Status of Neutrino Factory and Development and Future Plans, PRSTAB, 2002
- J. Letry, A. Fabich, S. Gilardoni, M. Benedikt, GMHFL Grenoble, EPFL, Thermal shocks and magnetohydrodynamics of high power mercury targets, proc. NuFact02, London, J. Phys. G, 2002